

**STUDY OF  
INTERMEDIATE MASS FRAGMENT EMISSION  
IN HEAVY-ION REACTION**

*By*

**SAMIR KUNDU**

**Enrolment No PHYS04200804002**

**Variable Energy Cyclotron Centre, Kolkata**

*A thesis submitted to the  
Board of Studies in Physical Sciences*

*In partial fulfillment of requirements  
For the Degree of*

**DOCTOR OF PHILOSOPHY**

*of*

**HOMI BHABHA NATIONAL INSTITUTE**



**January, 2013**

# Homi Bhabha National Institute

## Recommendations of the Viva Voce Board

As members of the Viva Voce Board, we certify that we have read the dissertation prepared by **Samir Kundu** entitled “**STUDY OF INTERMEDIATE MASS FRAGMENT EMISSION IN HEAVY-ION REACTION**” and recommend that it may be accepted as fulfilling the dissertation requirement for the Degree of Doctor of Philosophy.

.....**Date:**  
Chairman - Prof. Sudhee Ranjan Banerjee

.....**Date:**  
Guide / Convener - Prof. Sailajananda Bhattacharya

.....**Date:**  
Member 1 - Prof. Satyajit Saha

.....**Date:**  
Member 2 - Prof. Alok Chakrabarti

Final approval and acceptance of this dissertation is contingent upon the candidate's submission of the final copies of the dissertation to HBNI.

I hereby certify that I have read this dissertation prepared under my direction and recommend that it may be accepted as fulfilling the dissertation requirement.

**Date:**

**Place:**

## **STATEMENT BY AUTHOR**

This dissertation has been submitted in partial fulfillment of requirements for an advanced degree at Homi Bhabha National Institute (HBNI) and is deposited in the Library to be made available to borrowers under rules of the HBNI.

Brief quotation from this dissertation are allowable without special permission, provided that accurate acknowledgement of source is made. Requests for permission for extended quotation from or reproduction of this manuscript in whole or in part may be granted by the Competent Authority of HBNI when in his or her judgement the proposed use of the material is in the interests of scholarship. In all other instances, however, permission must be obtained from the author.

Samir Kundu

## **DECLARATION**

I, hereby declare that the investigation presented in the thesis has been carried out by me. The work is original and has not been submitted earlier as a whole or in part for a degree/diploma at this or any other Institution / University.

Samir Kundu

*To the memory of my father  
Sudhansu Sekhar Kundu*

# Acknowledgements

The work for this thesis is one of the best experiences in my life. It is a result of a challenging journey, upon which many people have helped and supported me, directly or indirectly. I gratefully acknowledge my sincere respects and thanks to my thesis supervisor, Prof. Sailajananda Bhattacharya. I am really proud to get opportunity to work with you. You have given me opportunity to work freely, you have encouraged me to think and work independently which is very important in my research carrier. Without your continuous support, help and encouragement, this thesis would not be completed. Besides my advisor, I would like to thank the rest of my thesis committee: Prof. S. R. Banerjee, Prof. Mlok Chakarbarty and Prof. Satyajit Saha, for their encouragement, insightful comments, and hard questions.

I would like to thank Prof. Chandana Bhattacharya for her friendly and open hearted support to complete this work. I have learnt a lot from you and am very glad about the fruitful time to have spent with you. Thank you so much!

I would like to acknowledge my thanks to my collaborators who directly helped me to do different experiments and developmental works included in this thesis. Those are Kaushik Banerjee, Capan K. Rana, Jaikiran Meena, Supriya Mukhopadhyay, Prof. S. R. Banerjee, A. Dey, C. K. Ghosh, G. mukherjee. I would also like to thank to my other collaborators D. Gupta, R. Saha, P. Mali, D. Pandit, H. Pai, Pratap Roy, Prof. S. Kumar, Prof. A. Shrivastava, Prof. A. Chatterjee, Prof. P. Banerjee, K. Ramachandran, K. Mahata, S. K. Pandit, S. Santra, C. Bhattacharjee, P. Mukhopadhyay, D. L. Bandyopadhyay, M. Ahammed and P. Bhattacharya. I would like to thank Amitava Roy and my friend Partha Dhara for providing the data analysis

software, on line as well as off line, and giving continuous support which helped me to collect and analyze the experimental data. I also express my thank to my other colleagues, Ruchi, Amiya and Jayanta for their indirect support in my work.

The experiments included in the present thesis have been performed at H130 Cyclotron, VEC at Kolkata and Pelletron at Mumbai. I would like to express special gratitude to the operating staff of these accelerators to provide us smooth and uninterrupted beams.

I am indebted to Prof. Dinesh Kumar Srivastava, Director, VEC for his constant inspiration to continue the research. I thank him for nurturing a favorable environment at VEC for research work, which indirectly helped me to carry out my work.

I am grateful to all of my friends and seniors who have supported and inspired me during many difficulties in my life. Immediately I remember Brindaban, Nitai, Santanu, Partha, Samal, Aditya, Jajati, Dipak Pati, Surajitda and Gautamda for their support and help.

Finally, I owe my loving thanks to my little son, Sayantan, who has been my constant source of energy and delight. I would like to thank my wife, Monika, whose love and encouragement allowed me to finish this journey. I owe a lot to my dear parents, who encouraged and helped me at every stage of my personal and academic life. I deeply miss my father, who is not with me to share this joy. I would like to dedicate this work to the memory of my father. I warmly thank my sisters, Anuja, Gopi and their families for their loving support. I would like to thank my maternal uncles, Chhoto-mama, Na-mama, Sejo-mama and Baro-mama for their loving support. I also thank in-laws and all my relatives for their sympathy during this work.

# Contents

<b>SYNOPSIS</b>	<b>xi</b>
<b>List of Figures</b>	<b>xxi</b>
<b>List of Tables</b>	<b>xxii</b>
<b>1 Introduction</b>	<b>1</b>
1.1 Fusion and decay of CN . . . . .	6
1.1.1 Decay of CN by evaporation . . . . .	8
1.1.2 Decay of CN by fission . . . . .	9
1.2 Deep inelastic collision . . . . .	12
1.2.1 Experimental results and its theoretical interpretations . . . . .	14
1.2.1.1 Deflection function . . . . .	14
1.2.1.2 Kinetic energy loss . . . . .	15
1.2.1.3 Time of interaction . . . . .	17
1.2.1.4 Angular momentum dissipation: theoretical limit . . . . .	18
1.3 Dinuclear orbiting . . . . .	20
1.3.1 Equilibrium orbiting model . . . . .	22
1.3.2 Number of open channel . . . . .	24
1.4 Motivation . . . . .	27

<b>2</b>	<b>Experimental setup and data analysis technique</b>	<b>31</b>
2.1	Accelerators . . . . .	32
2.1.1	Variable energy cyclotron . . . . .	32
2.1.2	BARC-TIFR Pelletron . . . . .	34
2.2	Experimental setups . . . . .	35
2.2.1	Scattering chambers . . . . .	35
2.2.2	Charged particle telescopes: particle identification . . . . .	37
2.2.3	Electronics and data collection . . . . .	41
2.2.4	Measurements . . . . .	41
2.3	Data analysis technique . . . . .	44
2.3.1	Target thickness measurement . . . . .	44
2.3.2	Gain matching factor . . . . .	45
2.3.3	Energy loss correction of the projectile and fragments . . . . .	46
2.3.4	Energy calibration of the telescopes . . . . .	48
2.3.5	Calculation of cross section . . . . .	49
<b>3</b>	<b>Result: Fragment and light particle emission in <math>^{16}\text{O} + ^{12}\text{C}</math> reactions</b>	<b>51</b>
3.1	Fragment emission study . . . . .	52
3.1.1	Energy spectra . . . . .	52
3.1.2	Angular distribution . . . . .	54
3.1.3	Angular distribution of average $Q$ -value . . . . .	55
3.1.4	Excitation energy dependence of $\langle Q \rangle$ averaged over angle . . . . .	56
3.1.5	Total cross section of the fragment . . . . .	57
3.2	Study of light charged particle emission . . . . .	59
3.2.1	Energy spectra . . . . .	59
3.2.2	Angular distribution . . . . .	61
3.2.3	Average velocity . . . . .	62
3.2.4	Statistical model calculations . . . . .	64

3.2.4.1	Input parameters . . . . .	65
3.2.4.2	Experimental spectra and CASCADE predictions . . . . .	67
3.2.5	Quadrupole deformation calculation . . . . .	67
<b>4</b>	<b>Result: Fragment emission in <math>^{12}\text{C} + ^{28}\text{Si}</math>, <math>^{12}\text{C} + ^{27}\text{Al}</math>, <math>^{11}\text{B} + ^{28}\text{Si}</math> reactions</b>	<b>72</b>
4.1	Study of fusion-fission fragments . . . . .	75
4.1.1	Angular distribution . . . . .	75
4.1.2	Angular distribution of $Q$ -value . . . . .	77
4.1.3	Total fragment yield . . . . .	77
4.2	Study of DI fragments . . . . .	78
4.2.1	Angular distribution . . . . .	78
4.2.2	Average $Q$ -value . . . . .	81
4.2.3	Total fragment yield . . . . .	81
<b>5</b>	<b>Discussions</b>	<b>83</b>
5.1	$\alpha$ -cluster systems and dinuclear orbiting . . . . .	83
5.1.1	Number of open Channels (NOC) . . . . .	85
5.1.2	Secondary decay of heavier fragments emitted in $^{16}\text{O} + ^{12}\text{C}$ . . . . .	87
5.1.3	Deformation in $^{28}\text{Si}^*$ . . . . .	89
5.2	Angular momentum dissipation in DI collision . . . . .	91
<b>6</b>	<b>Development a of high vacuum reaction chamber</b>	<b>95</b>
6.1	Basic design parameters . . . . .	97
6.2	Details of SHARC . . . . .	99
6.2.1	Mechanical details . . . . .	99
6.2.2	Target ladder assembly . . . . .	101
6.2.3	Input / Output ports . . . . .	102
6.2.4	Vacuum pumping system . . . . .	103

6.3	Operation of the chamber . . . . .	108
6.3.1	Operation of the pumping system . . . . .	109
6.3.2	Operation of target ladder . . . . .	112
6.4	Status . . . . .	114
<b>7</b>	<b>Summary and conclusion</b>	<b>116</b>
	<b>List of Publications</b>	<b>127</b>

# SYNOPSIS

The light particle evaporation, and fission are known to be the most dominant decay modes of a composite produced at low energy ( $E_{lab} \lesssim 10$  MeV/A) nuclear reaction. However, many other complex fragments with masses in between light particle and fission fragment are also found to be emitted with much lower yield than the above two processes. These fragments are called as intermediate mass fragments (IMF). Nowadays, the presence of IMF emission has been well-established in all kind of reactions at all excitation energies. To search the origin of IMF, intense studies have been done both theoretically and experimentally for the last few decades in heavy-ion as well as light-ion systems. But the origin is still not well understood, particularly in light-ion systems (typically,  $A_{projectile} + A_{target} \lesssim 60$ ) at moderate bombarding energy ( $E_{lab} \lesssim 10$  MeV/A). This might be due to the strong overlap between elemental yields of different processes. Situation becomes more complicated in the reactions involving  $\alpha$ -cluster systems, where nuclear structure is also known to play an important role in the equilibrium emission of complex fragments. In these cases, in addition to the standard fusion-fission route of fragment emission, the projectile and the target have a finite probability to form a long-lived dinuclear composite, which directly undergoes scission (without the formation of the fully equilibrated compound nucleus) to emit complex fragments. This process, termed as nuclear orbiting, has been shown to contribute significantly to the fragment yield in many reactions involving light  $\alpha$ -cluster nuclei (e.g.,  $^{20}\text{Ne} + ^{12}\text{C}$ ,  $^{24}\text{Mg} + ^{12}\text{C}$ ,  $^{28}\text{Si} + ^{12}\text{C}$  etc.). The orbiting is described in terms of the formation of a long-lived, dinuclear molecular complex, with a strong memory of the entrance channel. This phenomenon in general suggests weak absorption in the angular momentum window between the critical angular momentum of fusion,  $\ell_{cr}$ , and the grazing angular momentum,  $\ell_{gr}$ . In addition, substantial mass and charge transfer would also occur during the evolution of the orbiting dinuclear complex. So, the study of rearrangement channels will give opportunity to probe the dynamics of the orbiting process involving light nuclear systems.

The aim of the present thesis was to study the the reaction mechanism of IMF emission in light  $\alpha$ - and non  $\alpha$ -cluster systems ( $A_{CN} \leq 40$ ) in general, and to investigate into the role played by orbiting in light  $\alpha$ -cluster systems at moderate bombarding energy ( $E_{lab} \lesssim 10$  MeV/A), in particular. Two experiments have been performed under the present Ph.D programme. In the first experiment, the reaction mechanism of IMF emission and its evolution with bombarding energy have been studied in the  $\alpha$ -cluster system  $^{16}\text{O} + ^{12}\text{C}$ . Quadrupole deformation parameter of the composite system ( $^{28}\text{Si}^*$ ) has also been estimated from the comparison of slopes of the light charged particle spectra with the same obtained from statistical model predictions. In the second experiment, the emission processes of IMF have been studied in  $\alpha$ -cluster system  $^{12}\text{C} + ^{28}\text{Si}$  and the neighbouring non  $\alpha$ -cluster systems  $^{11}\text{B} + ^{28}\text{Si}$  and  $^{12}\text{C} + ^{27}\text{Al}$ , all having same excitation energy of  $\sim 67$  MeV, in order to look into the roles played by various IMF emission process in these reactions. In addition, a large reaction chamber has been developed for reaction mechanism studies, which is also part of this thesis.

Recently, a detailed study of the competition between direct and dissipative processes in binary channels in the systems  $^{16}\text{O} + ^{12}\text{C}$ ,  $^{18}\text{O} + ^{12}\text{C}$  have been made by S. Szilner *et al.* [ Nucl. Phys. A 779, 21 (2006)] in the energy range 5 - 7.7 MeV/ nucleon. For both the systems, resonant structure has been observed at lower energies and refractive effects at higher energies, which may be considered as the signature of the orbiting process. In the present work, a study of fragment emission has been done from  $^{16}\text{O} + ^{12}\text{C}$  reaction in the bombarding energy range  $\sim 7 - 10$  MeV/ nucleon with the aim to explore the role of different mechanisms (fusion-fission, deep inelastic orbiting, etc.) in the yields of various exit channels. Significant mass and charge transfer occur during the course of evolution of the rotating dinuclear complex, which leads to typical deep-inelastic reaction yields. Therefore, the study of the rearrangement channels offers a special interest in probing the dynamics of long-lived dinuclear complexes. For a better understanding of the orbiting process, it is important to study how the orbiting process evolves with energy. With this motivation, a detailed study of fragment energy

spectra have been made for the reaction  $^{16}\text{O} + ^{12}\text{C}$  at different bombarding energies viz.  $E_{\text{lab}} = 117, 125, 145$  and  $160$  MeV, respectively.

The inclusive energy spectra for fragments ( $3 \leq Z \leq 5$ ) emitted in the reaction  $^{16}\text{O} + ^{12}\text{C}$  at the energies 117, 125, 145 and 160 MeV have been measured at different angles. All the experimental signatures shows that the fragments are emitted from a long-lived equilibrated composite at all bombarding energies. Total elemental cross-section for the fragments Li to B have been measured from angular distributions. At all bombarding energies, it has been observed that there is an enhancement in the angle integrated yield of B in comparison with respective statistical model calculation. The origin of this enhancement is may be due to dinuclear orbiting. The above observation is consistent with the fact that the NOC (Number of Open Channel) values for this system are much smaller than those for other two near by systems. The energy and angular distributions of  $\alpha$ -particles have also been measured in the same experiment to extract the deformation of the produced composite  $^{28}\text{Si}^*$  using charged particle spectroscopy. Observed large deformation may be due to dinuclear orbiting.

In recent years, a few studies have been made on the  $\alpha$ -cluster system  $^{40}\text{Ca}^*$  and the neighbouring non- $\alpha$ -cluster systems to look into the relationship between equilibrium emission of fragment (and *vis-à-vis* orbiting) and  $\alpha$ -clustering. From the study of fragment emission ( $6 \leq Z \leq 8$ ) in the inverse kinematical reaction  $^{28}\text{Si} + ^{12}\text{C}$  at energies  $29.5 \text{ MeV} < E_{c.m.} < 50 \text{ MeV}$  [D. Shapira et al., Phys. Rev. Lett. 53, 1634(1984)], it has been conjectured that orbiting played a crucial role in fully energy-damped fragment emission. Even for the non  $\alpha$ -cluster system with  $A_{CN} \simeq 42$  ( $^{28}\text{Si} + ^{14}\text{N}$ ), where the NOC was large compared to that of  $^{28}\text{Si} + ^{12}\text{C}$ , the yields of fully energy damped fragments ( $6 \leq Z \leq 8$ ) were found to have contributions, though smaller in magnitude, from the orbiting process. It will, therefore, be worthwhile to study the emission of lighter fragments ( $Z < 6$ ) in particular, for systems around  $A_{CN} \simeq 40$ , to extract the contributions of different emission mechanisms, which will be partly complementary to the earlier measurements. Here, we have studied the light fragment ( $3 \leq Z \leq 5$ ) emission from  $\alpha$ -cluster system  $^{40}\text{Ca}^*$  produced in  $^{12}\text{C}$  (77 MeV) +  $^{28}\text{Si}$  reaction,

as well as those from the neighbouring composite system  $^{39}\text{K}^*$  produced at the same excitation energy of ( $\sim 67$  MeV) via two different reaction channels  $^{11}\text{B}$  (64 MeV)+ $^{28}\text{Si}$  and  $^{12}\text{C}$  (73 MeV)+ $^{27}\text{Al}$ ; the last two reactions have been chosen to crosscheck the equilibrium decay nature (absence of entrance channel dependence) of the energy damped binary fragment yield in the decay of  $^{39}\text{K}^*$ .

The inclusive energy distributions of the emitted fragments ( $3 \leq Z \leq 5$ ) have been measured in the angular range of  $\sim 12^\circ$  to  $55^\circ$ . The fusion-fission and deep inelastic components of yield of the fragments have been extracted for all three reactions. The c.m. angular distributions of the fusion-fission fragments have been found to follow  $1/\sin\theta_{c.m.}$  dependence, which signifies the emission of these fragments from a long-lived equilibrated composite. It has been found that the yields of the fully energy-damped fragments for all the above three reactions are in conformity with the respective statistical model predictions. The absence of any entrance channel dependence in FF components of the yields of the fragments ( $3 \leq Z \leq 5$ ) emitted from the reactions  $^{11}\text{B}$  (64 MeV) +  $^{28}\text{Si}$  and  $^{12}\text{C}$  (73 MeV)+  $^{27}\text{Al}$  is consistent with the compound nuclear origin. It has been shown that the DI fragment angular distribution falls much faster than  $1/\sin\theta_{c.m.}$  distribution. The time scale of the DI process has been estimated from the DI angular distribution. It has been observed that for all these reactions, the time scale, which is related to net nucleon transfer, decreases as the fragment charge increases (closer to the projectile charge). It has also been observed that the average  $Q$  values for the DI fragments decrease with the increase of emission angle and saturate at higher angles, signifying a saturation in energy damping process beyond these angles. Assuming a compact exit channel configuration (estimated from the extracted FF part of the spectra), the angular momentum dissipation factor,  $f$ , for the DI process has been extracted. For all the three reactions, the experimental values of  $f$  have been found to be in fair agreement with the corresponding sticking limit predictions.

Several large experimental facilities are being built as a part of the K500 Superconducting Cyclotron (SCC) utilization program at VECC which will enable to continue IMF studies in the Fermi Energy domain. I have, as a part of my thesis work,

contributed to the design, development, installation, testing, of the large multipurpose reaction chamber. It is a large (1m diameter, 2.2m long), Segmented, Horizontal Axis, Reaction Chamber (SHARC) which can be pumped down to a nominal pressure of  $\sim 5 \times 10^{-7}$  mbar in  $\sim 8$  hours by means of two turbo-molecular (1000 l/s) and two cryo pumps (2500 l/s) backed by two mechanical pumps (37m<sup>3</sup>/hr). The dimensions of SHARC have been optimized to have maximum flexibility for versatile experimental setups; optimum shape has been decided to be cylindrical with its axis coinciding with the beam axis to avail maximum possible flight path for time of flight measurements. The vacuum system and movement of target ladder both can be controlled by PLC (Programmable Logic Controller) in auto and manual modes with dynamic display of complete status. There is a provision for remote monitoring of vacuum status with emergency shutdown option. Option has also been kept for remote operation of target ladder system. Special technique has been developed to fabricate flange with multiple flat ribbon connectors as a feedthrough for detectors placed within SHARC. The installation of the chamber has been completed and presently it is aligned with the beam line of SSC.

# List of Figures

1.1	Trajectories of heavy ion collision in classical picture. . . . .	3
1.2	Typical nucleus-nucleus potential. $r$ is the distance between the centers of the nuclei. . . . .	4
1.3	The spin distribution of a heavy-ion reaction. The regions for quasi-elastic collision ( $\sigma_{QE}$ ), deep-inelastic collision ( $\sigma_{DI}$ ) and for fusion ( $\sigma_F$ ) are indicated. For $\ell > \ell_{gr}$ , only Coulomb excitation and elastic scattering are possible. . . . .	5
1.4	Energy balance is shown schematically for fusion-fission reaction. . .	11
1.5	(A) Saddle point energies ( $V_{saddle}$ ) for light system $A = 56$ as a function of spin and mass asymmetry, (B) $V_{saddle}$ for heavy system $A = 230$ as a function of mass asymmetry. . . . .	12
1.6	Different types of classical deflection function $\Theta(\ell)$ as a function of ratio of angular momentum and Sommerfeld parameter. . . . .	15
1.7	(a) Average kinetic energies of various fragments emitted in the reaction $^{40}\text{Ar} + ^{197}\text{Au}$ . The solid lines represent the theoretical values expected from Coulomb repulsion of two touching spheres and of two touching spheroids.(b) Correlation between total kinetic energy loss (TKEL) and charge dispersion for the projectile-like fragments in various Kr- and Xe-induced reactions. . . . .	16
1.8	Reaction variables for the collision of spherical projectile (P) and target (T) nuclei. . . . .	18
1.9	Difference between fusion-fission (left column) and orbiting (right column) mechanism is shown. . . . .	22
1.10	Variation of NOC with $\ell_{gr}$ for different systems. . . . .	26
2.1	K130 variable energy cyclotron. . . . .	32

2.2	Beam line layout of K30 variable energy cyclotron. . . . .	34
2.3	Accelerator and beam line layout of TIFR-BARC pelletron. . . . .	36
2.4	(a) Schematic diagram of experimental setup used in both experiments done at VECC and pelletron.(b) General purpose scattering chamber, Ch # 2, VECC. (c) Partial view of experimental setup at scattering chamber, Pelletron. . . . .	38
2.5	$\Delta E$ - $E$ heavy ion spectrum obtained in 117 MeV $^{16}\text{O} + ^{12}\text{C}$ reaction at $\theta_{lab} = 12^\circ$ . . . . .	39
2.6	Schematic diagram of electronics circuit used in the experiment at VECC. PA: Preamplifier, AMP: Amplifier, TFA: Timing filter amplifier, CFD: Constant fraction discriminator, GG: Gate and delay generator, OR: Fan-in-Fan-out. . . . .	42
2.7	Typical gain matching spectra of telescope IV, used in the experiment performed at VECC. . . . .	45
2.8	Energy loss of projectile and ejectile in the target. . . . .	46
2.9	The effect of energy loss correction on fragments in the target. Black line is the detected spectrum and pink line is the corresponding spectrum after energy loss correction. . . . .	47
2.10	Calibration of telescope IV used in the experiment at VECC. . . . .	49
3.1	Typical energy spectra of emitted fragments (B, Be and Li) detected at an angle $\theta_{lab} = 15^\circ$ at respective $E_{lab}$ . Arrows indicate the centroid of the Gaussian distributions. . . . .	53
3.2	The c.m. angular distributions of the B, Be and Li fragments obtained at $E_{lab} = 117, 125, 145, \text{ and } 160$ MeV [from (a) to (d), respectively]. Solid circles correspond to experimental data and solid lines show fit to the data obtained using the function $f(\theta_{c.m.}) \propto 1/\sin\theta_{c.m.}$ . . . . .	54
3.3	Average $Q$ -values, $\langle Q \rangle$ , of the fragments B, Be and Li obtained at $E_{lab} = 117, 125, 145$ and $160$ MeV (denoted by triangle up, triangle down, square and circle, respectively) plotted as a function of c.m. emission angle, $\theta_{c.m.}$ . . . . .	56
3.4	Variation of $\langle \bar{Q} \rangle$ with $E_{c.m.}$ . The solid lines show the linear dependence of $\langle \bar{Q} \rangle$ with bombarding energy for the fragments B, Be and, Li respectively. . . . .	57

3.5	Excitation functions for the angle-integrated (over the range $0^0 \leq \theta_{c.m.} \leq 180^0$ ) cross section of the B, Be and Li fragments. Solid lines are the predictions of the statistical model CASCADE with angular momentum $\ell = \ell_{cr}$ . Short dashed lines are the prediction of EHF. . . . .	58
3.6	Energy spectra (c.m.) of $\alpha$ -particles obtained at different angles for different beam energies. The symbols represent experimental data and the solid lines represent the fitted Maxwellian function. All the experimental and calculated spectra for lower to higher angles have been multiplied by $10^{-2}, 10^{-1}, 10^0, 10^1, 10^2, 10^3$ , respectively. . . . .	60
3.7	Comparisons of the energy spectra (c.m.) of $\alpha$ -particles obtained at most forward (red triangles) and backward angles (blue open inverted triangles) at different beam energies. Beam energies and c.m angles are written on the figure. . . . .	61
3.8	Angular distribution of $\alpha$ -particles as a function of c.m. angles, $\theta_{c.m.}$ . Symbols represents the experimental data and solid lines show fit to the data obtained using $(d\sigma/d\theta)_{c.m.} = \text{constant}$ . . . . .	62
3.9	Average velocity curve of the $\alpha$ -particle in laboratory frame. Solid pink circles corresponds to experimental data measured at different angle mentioned in the figure and solid lines show fit to the data obtained using Eq. 3.7. The blue, green, and pink arrows indicate the velocity of the composite nucleus in lab ( $v_{CN}$ ), average velocity of $\alpha$ -particle in c.m. ( $v_{av}^{c.m.}$ ), and average velocity of $\alpha$ -particle in lab frame ( $v_{av}$ ), respectively. . . . .	63
3.10	Average velocity curve. Symbols corresponds to experimental data and solid lines show fit to the data obtained using equation $v_{\perp}^2 = v_{c.m.}^2 - (v_{\parallel} - v_{CN})^2$ . The arrows indicate the position of $v_{CN}$ . . . . .	64
3.11	Energy spectra (c.m.) of $\alpha$ particles obtained at different angles for different beam energies. The symbols represent experimental data. The dash-dot-dash and solid lines represent CASCADE calculations with default and optimized values of spin dependent ‘deformability’ parameters, respectively (see Table 3.2). All experimental and calculated spectra, starting from the lowest angle, were multiplied by $10^{-2}, 10^{-1}, 10^0, 10^1, 10^2, 10^3$ , respectively. . . . .	69
4.1	Typical energy spectra of the fragments measured for the reactions $^{12}\text{C} + ^{28}\text{Si}$ (a - c), $^{12}\text{C} + ^{27}\text{Al}$ (d - f) and $^{11}\text{B} + ^{28}\text{Si}$ (g - i) at $\theta_{lab} = 17.5^{\circ}$ (a - h) and $30^{\circ}$ (i). The blue dash-dotted, the black dotted, and the red solid curves represent the contributions of the FF, the DI, and the sum (FF + DI), respectively. The left and the right arrows correspond to the centroids of FF and DI components of energy distributions, respectively. . . . .	73

4.2	The typical extraction procedure of FF and DI components from the total energy spectrum of Be fragment measured in the reaction $^{12}\text{C} + ^{27}\text{Al}$ at $\theta_{lab} = 17.5^\circ$ . Detail of the extraction procedure is given in the text. The arrow at low and higher energy indicates the FF and DI peaks, respectively. . . . .	74
4.3	The c.m. angular distributions of the fragments Li (a), Be (b) and B (c). Solid circles (red), triangles (blue) and inverted triangles (black) correspond to the experimental data for the reactions $^{11}\text{B} + ^{28}\text{Si}$ , $^{12}\text{C} + ^{27}\text{Al}$ and $^{12}\text{C} + ^{28}\text{Si}$ , respectively. Solid curves are fit to the data with the function $f(\theta_{c.m.}) \propto 1/\sin\theta_{c.m.}$ . . . . .	75
4.4	Average $Q$ -values of the FF fragments Li, Be and B represented by inverted green triangle, pink triangle and blue circle, respectively for reactions (a) B + Si, (b) C + Al and (c) C + Si. . . . .	76
4.5	The total FF fragment cross sections (c.m.) for the three reactions. The solid circles (red), triangles (blue), and inverted triangles (black) correspond to the experimental data for $^{11}\text{B} + ^{28}\text{Si}$ , $^{12}\text{C} + ^{27}\text{Al}$ , and $^{12}\text{C} + ^{28}\text{Si}$ reactions, respectively. The solid (red), dashed (blue) and dotted (black) lines are the corresponding theoretical predictions. . . . .	77
4.6	The c.m. angular distributions of the DI fragments [Li (a), Be (b), and B (c)]. The solid circles (red), triangles (blue), and inverted triangles (black) correspond to the experimental data for $^{11}\text{B} + ^{28}\text{Si}$ , $^{12}\text{C} + ^{27}\text{Al}$ , and $^{12}\text{C} + ^{28}\text{Si}$ reactions, respectively; the solid lines are the fits to the data (see text). . . . .	79
4.7	The emission time scales of different DI fragments. . . . .	81
4.8	The average $Q$ -values, $\langle Q_{DI} \rangle$ , plotted as function of $\theta_{c.m.}$ for Li (green inverted triangle), Be (pink triangle), and B (blue solid circle) emitted in (a) $^{11}\text{B} + ^{28}\text{Si}$ , (b) $^{12}\text{C} + ^{27}\text{Al}$ , and (c) $^{12}\text{C} + ^{28}\text{Si}$ reactions. Solid lines are plotted to guide the eye. . . . .	82
4.9	Total DI cross sections of the fragments obtained in three different reactions. . . . .	82
5.1	Number of open channels for decay of composite nucleus (a) $^{28}\text{Si}^*(^{16}\text{O} + ^{12}\text{C})$ , $^{31}\text{P}^*(^{19}\text{F} + ^{12}\text{C})$ and $^{28}\text{Al}^*(^{10}\text{B} + ^{18}\text{O})$ and (b) $^{12}\text{C} + ^{28}\text{Si}$ , $^{14}\text{N} + ^{28}\text{Si}$ , $^{11}\text{B} + ^{28}\text{Si}$ , $^{12}\text{C} + ^{27}\text{Al}$ , normalized to the incident flux, $N/F$ , plotted as a function of grazing angular momentum, $\ell_{gr}$ . . . . .	86

5.2	Secondary decay contribution to B fragment estimated from LILITA at energies 117 and 160 MeV, respectively. The energy distribution of B at these energies at $\theta_{lab}=15^0$ are shown along with fitted Gaussians. In the same graph, the difference spectra (Gaussian subtracted from total spectra) is shown by pink curve and blue dashed curve represents the total secondary decay contribution estimated using LILITA. . . . .	88
5.3	Comparison of the experimental energy spectra (c.m.) of $\alpha$ -particles (red triangles) with the same obtained by theoretical calculations for beam energy 160 MeV. Green solid line represent the CASCADE calculations done using ‘frozen’ deformation ( $I_{eff}/I_0$ ) obtained using RLDM deformability parameters for $\ell = 23\hbar$ . . . . .	90
5.4	The variation of angular momentum dissipation factor $f$ with atomic number of the fragments. The solid circles (red), solid triangles (blue), and inverted triangles (black) are the extracted values of $f$ for (a) $^{11}\text{B} + ^{28}\text{Si}$ , (b) $^{12}\text{C} + ^{27}\text{Al}$ , and (c) $^{12}\text{C} + ^{28}\text{Si}$ reactions, respectively. The solid (black) and dotted (pink) curves correspond to the sticking limit and the rolling limit predictions for the same, respectively. . . . .	93
6.1	Different types of reaction chambers used at different laboratory all over the world. . . . .	96
6.2	Schematic diagram of K500 cyclotron beam lines with three beam hall. SHARC has been installed in beam line-I. . . . .	97
6.3	Schematic diagram of SHARC without vacuum pumping system. . . . .	99
6.4	SHARC installed in SCC Cave-I. . . . .	100
6.5	SHARC target assembly. . . . .	101
6.6	(a) Design of different component of FRC vacuum feed through. Holes in the PCB are kept to place FRC. (b) The flange after final casting. . . . .	104
6.7	Variation of pumping speed of the scroll pump with inlet pressure. . . . .	105
6.8	Local control panel of SHARC. It control both the vacuum system, target ladder and also shows the status all other operations of SHARC. . . . .	107
6.9	Remote control panel of target ladder. It also shows the status all operation of target ladder and pumping system. . . . .	108
6.10	Schematic diagram of SHARC with vacuum pumping system. . . . .	110
6.11	A typical pumping sequence. Unit of the pressure is in mbar. . . . .	111
6.12	Human machine interface in auto mode. . . . .	112

6.13	Human machine interface in manual mode. Details of the buttons are given in the text. . . . .	113
6.14	Vacuum performance of SHARC during a typical pumping cycle. . . .	114

# List of Tables

2.1	Technical specifications of K130 cyclotron. . . . .	33
2.2	Technical details of the telescopes. . . . .	40
2.3	Experimental details. . . . .	43
3.1	Input parameters used for CASCADE calculations for the reactions $^{16}\text{O} + ^{12}\text{C}$ at beam energies 117, 125, 145 and 160 MeV. . . . .	68
3.2	The values the of ‘deformability’ parameters: A - obtained from RLDM, and, B - obtained by fitting the experimental data (see text) have been given below. $E_{lab}$ , $E$ , $\ell_{cr}$ and $\ell_{av}$ are the beam energy, excitation energy, critical angular momentum and average angular momentum, respectively. . . . .	70
3.3	The values the of quadrupole parameters: A - obtained from ‘deformability’ using RLDM, and, B - extracted using ‘deformability’ parameters obtained by fitting the experimental data. The ‘deformability’ parameters are given in Table 3.2. . . . .	71
4.1	Emission time scale of different DI fragments for all three reactions. . . . .	80
6.1	Throughput of the materials used in different parts of SHARC over a period of $\sim 6$ -7h. Throughput is defined as the product of outgassing rate and surface area of the material. . . . .	106

# Chapter 1

## Introduction

The nuclear force, which holds neutrons and protons together inside an individual nucleus, starts affecting other nuclei when a nucleus comes sufficiently close to another nucleus. As a result, the initial system (of interacting nuclei) is modified and a different final system is produced. These phenomena, in general, are called nuclear reactions. If the interacting ions are heavier than helium, then the nuclear reaction is called 'heavy ion reaction'. In any nuclear reaction, the intermediate composite produced in course of evolution of the system is usually having lot of excitation energy which is sufficient to cause its decay through various modes. The light particle ( $Z \leq 2$ ) evaporation and fission are known to be most dominant decay modes of a composite produced in the reactions at moderate bombarding energy ( $E_{lab} \lesssim 10-15$  MeV/A). In addition, many other complex fragments with masses in between light particles and fission fragments are also found to be emitted in this energy range with much lower yield than the above two processes. These fragments (typically,  $2 < Z \lesssim 20$ ) are called intermediate mass fragments (IMF). According to the number of fragments emitted in a single event, a reaction can be classified in two broad categories, binary or multifragmentation reaction. At lower energy ( $E_{lab} \lesssim 10-15$  MeV/A), the composite is generally divided into two fragments and the process is called binary fragmentation. On the other hand, at higher energy, in addition to the binary process, composite may also be fragmented

into more than two pieces and this process is called multifragmentation. The type of reaction product depends on the masses of the projectile and target also. For example, in heavy system ( $A \gtrsim 100$ ), one of the possibilities of decay of the compound nucleus is symmetric fission, where the fragment mass distribution peaks around half of the total mass of target and projectile. On the other hand, in light heavy-ion reaction ( $A \lesssim 100$ ), the decay of CN is replaced by asymmetric fission (emission of IMF). In this thesis, we have restricted ourselves to low-energy light heavy-ion collisions, with energy  $\lesssim 10\text{MeV}/A$  for the experimental work. Here, we shall discuss only IMF emission process in the low energy range ( $E_{lab} \lesssim 10\text{MeV}/A$ ).

The energies of the bombarding heavy ions under the present study are such that the de Broglie wave length,  $\lambda$ , is small relative to the characteristic length of the interaction potential. Therefore, the collision can be treated within the classical limit. The only force that opposes the colliding nuclei to come close to each other is the Coulomb repulsion force. Let  $r_1$  and  $r_2$  be the radii of the projectile and target nuclei, respectively. The coulomb barrier at interaction distance of the colliding nuclei, is

$$V(R) \approx \frac{Z_1 Z_2 e^2}{r_1 + r_2} \quad (1.1)$$

where  $R = r_1 + r_2 + \Delta$ ,  $\Delta$  is a correction term due to surface diffuseness. So, at least this much of energy in the centre of mass (c.m.) is required for a nuclear reaction. At this interaction barrier, the wave length of relative motion is [1]

$$\lambda = \frac{\hbar}{[2\mu\{E_{c.m.} - V(R)\}]^{1/2}} \approx \left( \frac{A_1 + A_2}{A_1 A_2} \frac{20\text{MeV}}{E_{c.m.} - V(R)} \right)^{1/2} \text{ fm} \quad (1.2)$$

where  $A_1$ ,  $A_2$ ,  $E_{c.m.}$  ( $= \frac{A_2}{A_1 + A_2} E_{Lab}$ ) denote the mass numbers of the projectile, target, and the energy in the c.m. frame, respectively. As an example, in the collision of  $^{16}\text{O}$  at  $E_{lab} = 117 \text{ MeV}$  on  $^{12}\text{C}$ ,  $\lambda \approx 0.3 \text{ fm}$  which is small as compared to the characteristic lengths (e.g., surface thickness  $\approx 2 \text{ fm}$ ) of the interaction potential of the colliding nuclei. Hence the classical treatment is justified.

So, to a first approximation, low energy heavy ion (HI) reactions can be described in terms of classical trajectories. Each impact parameter determines a unique trajectory; therefore, each type of binary reaction processes can be classified by a typical

zone of impact parameters  $b$  (see Fig. 1.1), which are related to the relative angular momenta,  $\ell$ , of the entrance channel by the semi-classical relation,

$$\ell = bp_\infty/\hbar = b/\lambda \quad (1.3)$$

where  $p_\infty$  is the relative momentum of the colliding nuclei in entrance channel. Overall

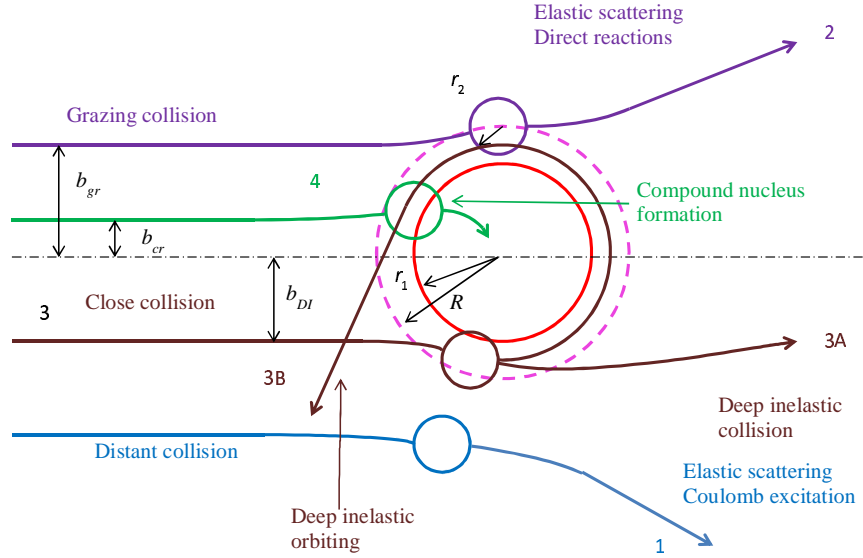


**Figure 1.1:** Trajectories of heavy ion collision in classical picture.

features of most of the binary reactions can be fairly well described by the classical collision trajectories shown in Fig. 1.1 and by the effective interaction potential,  $V_{eff}$ , of the colliding nuclei in the radial wave equation for different angular momentum, as shown in Fig. 1.2. The radial part of this potential has three parts: (a)  $V_N$ , the strongly attractive nuclear potential which practically acts inside the volume occupied by ions (interaction zone) and falls off exponentially outside the zone, (b) the repulsive Coulomb potential,  $V_C$ , which is  $\sim Z_1Z_2e^2/r$  and  $r > R_c$ , and  $\sim (Z_1Z_2e^2/2R_c)(3 - r^2/R_c^2)$  for  $r < R_c$  and  $R_c$  is the charge radius [2], and (c) repulsive centrifugal potential,  $\ell(\ell + 1)\hbar^2/2\mu r^2$ . Classically, effective potential

$$V_{eff}(r) = V_N + V_C + \ell(\ell + 1)\hbar^2/2\mu r^2 \quad (1.4)$$

should determine the trajectory of the interacting ions. But as soon as one nucleus comes in touch with other, nucleon exchange may start which is represented by an

absorbing potential. Quantum mechanically, the absorption process is represented by an imaginary potential as done in optical model potential. Absorption causes a loss of the incident flux; however the classical trajectories are largely decided by the real part,  $V(r)$ , of the potential  $V_{eff}$ , shown schematically, in Fig. 1.2. When the energy of the

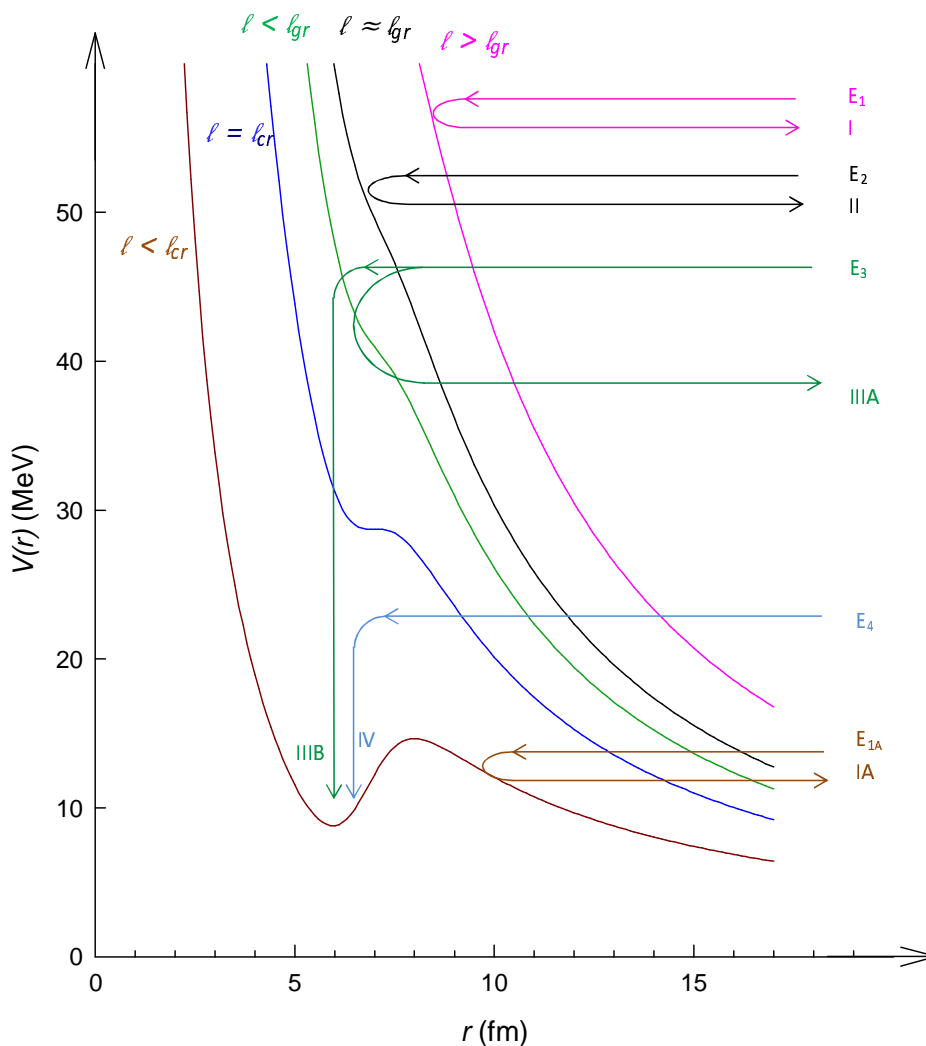


**Figure 1.2:** Typical nucleus-nucleus potential.  $r$  is the distance between the centers of the nuclei.

projectile  $E_1$  (Fig. 1.2) is much higher than the Coulomb barrier, for distant collision ( $l \gg l_{gr}$  or  $b \gg b_{gr}$ ), only elastic scattering will result and a possibility of Coulomb excitation is also there (trajectory 1, Fig. 1.1). The same result will be seen for any impact parameter when the energy ( $E_{1A}$ , Fig. 1.2) is less than the Coulomb barrier. At

energies above the barrier (e.g.,  $E_1, E_2, E_3, E_4$ ), the reaction process gradually evolves with impact parameter from elastic/inelastic collision to fusion. For grazing collision ( $\ell \cong \ell_{gr}$  or  $b \cong b_{gr}$ ), the incident ion may be elastically or inelastically scattered or direct reaction occurs with the exchange of few nucleons in between interacting ions; the scattered particle follow the path II as in Fig. 1.2 and trajectory 2 in Fig. 1.1. If the impact parameter is reduced further, below a certain value,  $b_{DI}$  (Fig. 1.1), interaction between the nuclei increases sharply due to significant overlap of nuclear densities of the colliding nuclei. This results in the exchange of nucleons between colliding particles leading to the dissipation of kinetic energy and orbital angular momenta from the entrance channel. Classically, this is described as friction and the process is called deep

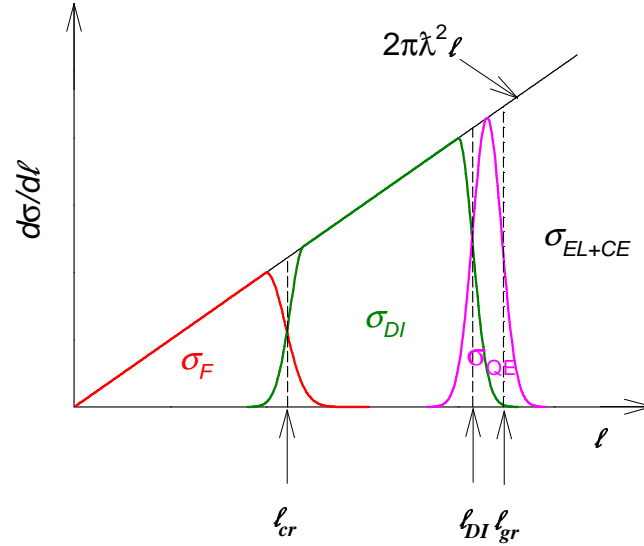


**Figure 1.3:** The spin distribution of a heavy-ion reaction. The regions for quasi-elastic collision ( $\sigma_{QE}$ ), deep-inelastic collision ( $\sigma_{DI}$ ) and for fusion ( $\sigma_F$ ) are indicated. For  $\ell > \ell_{gr}$ , only Coulomb excitation and elastic scattering are possible.

inelastic (DI) process (trajectory IIIA, Fig. 1.2). During this process of dissipation, the shape of the composite resembles close to a rotating dumb-bell, which evolves differently depending on the impact parameter. If the rotation is more than  $360^\circ$  (trajectory IIIB, Fig. 1.2), then the dinuclear complex, which is fully energy equilibrated, may either completely fuse to form a CN or breaks up into a binary exit channel having partial memory of the entrance channel. The second way of evolution is called deep

inelastic orbiting (DIO)[3] (path 3B as in Fig. 1.1). For more central collision, ( $\ell \lesssim \ell_{cr}$  or  $b \lesssim b_{cr}$ ), nuclei get trapped in the nucleus-nucleus potential pocket and remain together for a long time enough to desolve their individual identities and get fused into a single compound nucleus which follow the path IV (Fig. 1.2). Using sharp cutoff model, the total cross-section for all these processes may be estimated as

$$\begin{aligned}\sigma &= \pi b^2 = \pi \lambda^2 \ell^2 \\ \Rightarrow d\sigma/d\ell &= 2\pi \lambda^2 \ell\end{aligned}\quad (1.5)$$

The cross-sections for quasi elastic (QE) process, deep inelastic collision and fusion may be written as,

$$\sigma_{QE} = \pi \lambda^2 (\ell_{gr}^2 - \ell_{DI}^2) \quad (1.6)$$

$$\sigma_{DI} = \pi \lambda^2 (\ell_{DI}^2 - \ell_{cr}^2) \quad (1.7)$$

$$\sigma_F = \pi \lambda^2 \ell_{cr}^2 \quad (1.8)$$

Decomposition of all these cross-sections is pictorially shown in Fig. 1.3 [4]. All of the above discussions are based on semiclassical phenomenology and are highly qualitative (dashed lines). The sharp distinction between different processes are removed in full quantum mechanical explanation (solid lines, Fig. 1.3) [5].

## 1.1 Fusion and decay of CN

The above discussion shows that for central collision ( $b \lesssim b_{cr}$ ), at energy above the Coulomb barrier, the projectile and the target completely amalgamate to form a single, fully equilibrated compound nucleus; this process is called complete fusion. Apart from a few quantities, which are subject to the conservation laws (energy, angular momentum, parity), the compound nucleus completely loses memory on the way it was formed and the decay of CN is independent of the entrance channel. This hypothesis of CN was originally given by N. Bohr [6] to explain the resonance in the neutron capture cross section at the thermal energy range. However it has been established that

the CN hypothesis is valid for heavy ion reactions at higher excitation energies also. The formation cross section of CN is already given in Eq. 1.8, which is based on sharp cutoff model. Though the sharp cutoff model is quite successful to estimate the cross section, the quantum mechanical calculation shows that for a particular  $\ell$  there is finite probability of fusion as well as other reaction (e.g, DI, DIO, etc.). So, the partial cross section for formation of CN of spin  $J$  from projectile and target nuclei of intrinsic spins  $I_P$  and  $I_T$ , respectively, at c.m. energy  $E_{c.m.}$  is given by

$$\sigma_{CN}(J) = \pi\lambda^2 \frac{2J+1}{(I_P+1)(I_T+1)} \sum_{S=|I_P-I_T|}^{I_P+I_T} \sum_{\substack{\ell=|J-S| \\ [\pi]}}^{J+S} T_\ell(E_{c.m.}) \quad (1.9)$$

where  $T_\ell(E_{c.m.})$ , the transmission coefficient, represents the probability of a partial wave ( $\ell$ -wave) to be absorbed to form the compound nucleus and  $S = I_P + I_T$  is the channel spin. The summation over  $\ell$  is restricted by the parity selection rule,  $\pi = \pi_P \pi_T (-1)^\ell$  where  $\pi, \pi_P$ , and  $\pi_T$  are the parities of CN, projectile and target, respectively [7]. The total fusion cross section can be written as

$$\sigma_{CN} = \sum_{J=0}^{\infty} \sigma_{CN}(J) \quad (1.10)$$

The CN is usually produced at sufficiently high excitation energy. This excited CN releases its energy by evaporation [the emission of  $\gamma$ -rays, nucleons ( $p, n$ ), cluster of nucleons ( $d, t, \alpha$ )] , or by fission. Relative yields of different ejectiles depend upon the mass, charge, excitation energy, angular momentum of the CN. The coulomb barrier, which inhibits the emission of light charged particles (LCP), is less in light system; that made it possible to compete for the LCP emission  $\ell$  with neutron emission. For higher angular momentum, repulsive centrifugal force is also high which favours the emission of  $\alpha$  particles.  $\gamma$ -ray emission dominates when the available excitation energy is not sufficient for particle emission. Fission is generally inhibited in the light systems because the surface energy is more than Coulomb energy; however, a system of heavier mass ( $A \sim 200$ ) with higher angular momentum, will have significant fission width, which may compete with, and even dominates over evaporation process.

### 1.1.1 Decay of CN by evaporation

Nucleus is a many body complex system. When the energy is transferred from the projectile to the CN, it is distributed over numerous degrees of freedom of the CN like thermal distribution of energy in a liquid drop. Even a small increase in excitation energy, causes a large increase of the number of available quantum-mechanical states. So, there are many states available in CN and there are many ways to decay. In such a complex situation, statistical methods are essential for proper comprehension and prediction of the subsequent decay of the CN. The evaporation yields (particles and residue) of CN is well predicted by the codes based on quantum statistical methods, such as CASCADE [7], LILITA [8], PACE[9], GEMINI [10]. These codes basically use a method proposed by Hauser-Feshbach (HF) [11] around six decades ago. In HF method, the partial cross section of emission of a particle  $x$  from a CN of spin  $J$  is given by

$$\sigma_x(J) = \frac{\Gamma_x(J)}{\sum_x \Gamma_x(J)} \times \sigma_{CN}(J) \quad (1.11)$$

where  $\sigma_{CN}(J)$  is the cross section of the populated compound states (Eq. 1.9),  $\Gamma_x(J)$  is the partial width of emission of  $x$  and  $\sum_x \Gamma_x(J)$  is the sum of all the partial widths of all particles. The partial width that the parent nucleus (excitation energy  $E_1$ , spin  $I_1$ , parity  $\pi_1$ ) emits a particle  $x$  with an orbital angular momentum  $\ell$ , kinetic energy  $\epsilon_x$  ( $\epsilon_x = E_1 - E_2$ ) and spin  $s$  is given by

$$\Gamma_x(J) = \frac{\rho_2(E_2, I_2, \pi_2)}{2\pi\rho_1(E_1, I_1, \pi_1)} \times \sum_{S=|I_2-s|}^{I_2+s} \sum_{\substack{\ell=|I_1-S| \\ [\pi]}}^{I_1+S} T_\ell(\epsilon_x) d\epsilon_x \quad (1.12)$$

where  $E_2$ ,  $I_2$  and  $\pi_2$  are the excitation energy, spin and parity of the daughter nucleus,  $\rho_1$  and  $\rho_2$  are the level-densities of the excited parent nucleus and daughter nucleus, respectively, and,  $S = I_2 + s$  is the channel spin. The transmission coefficients  $T_\ell(\epsilon_x)$  for the scattering of particle  $x$  on daughter nucleus (inverse process) are obtained by using standard Optical Model (OM). The level density for a given angular momentum  $J$  and excitation energy  $E$ , is given by well-known Fermi gas expression with equidistant

single-particle levels and a constant level density parameter  $a$ :

$$\rho(E, J) = \frac{(2J + 1)}{12} a^{1/2} \left( \frac{\hbar^2}{2\mathcal{I}_{eff}} \right)^{3/2} \frac{1}{u^2} \exp[2\{au\}^{1/2}] \quad (1.13)$$

$$u = E - \Delta - E_J \quad (1.14)$$

where  $\Delta$  is the pairing correction,  $E_J$  is the rotational energy[12].

All the above codes based on HF formalism well predict the energy distribution of the particles emitted from fully equilibrated CN with thermodynamic temperature  $T$ , which can be expressed as,

$$\frac{d^2\sigma}{dEd\Omega} = Cf(E) \exp(-E/T) \quad (1.15)$$

which is similar to the energy distribution of the molecules evaporating from the surface of a liquid. Hence CN decay is often refereed as particle evaporation process.

### 1.1.2 Decay of CN by fission

Another decay mode of CN is fission. After the formation by collision of two ions, shape of the excited CN is distorted like a liquid drop. If the excited CN is considered as charged liquid, liquid drop model in its simple form can be applied to describe the changes in potential energy associated with the shape change [13]. The surface and Coulomb energies are affected by the distortion. The attractive surface energy term tries to minimize the surface area of the CN, to keep it spherical, whereas the repulsive Coulomb energy term tries to elongate the shape of CN. Sum of these two energies creates a pocket because of their functional difference as shown in Fig. 1.4 (Figure has been taken from [12]). When the change in Coulomb energy due to distortion is more than the change in surface energy, CN decays through fission. The shape for which the potential energy is maximum along the fission path, is called ‘saddle’ point (Fig. 1.4). This is the point of no return, i.e., if CN crosses this shape, it must go to fission; the corresponding shape is called ‘saddle’ shape. Actually, if one draws the potential energy in two dimensions with respect to elongation and mass asymmetry of fission

fragments, potential surface looks like the shape of a saddle. Hence the corresponding shape of CN is called saddle shape. The system, in course of its evolution, gradually passes through the saddle point to reach scission point, where the fission (binary splitting) actually takes place; the corresponding shape is called ‘scission’ shape.

First quantitative description of fission process was given by N. Bohr and J. A. Wheeler to explain neutron induced fission (transition state model) [14]. In this model, fission competes with  $\gamma$ -ray and LCP emission in the de-excitation of CN. The probability of fission depends on the number of available ‘transition states’, which is usually taken as the total available phase space of the CN above the saddle-point (Fig. 1.4). However, the large anisotropy observed in the angular distribution of fission products coming from heavier systems with vanishing fission barrier, has been explained by considering the more deformed scission point as the transition point [15, 16]. In lighter systems, saddle-point and scission-point configuration are nearly same. So, the calculation based on saddle-point [17] and scission-point [18] transition-state configurations are found to be give equivalent results in lighter systems. The calculation of fission cross section is based on Hauser-Feshbach formalism as in case of fusion-evaporation (Eq. 1.11), which can be written as

$$\sigma_{fis}(J) = \frac{\Gamma_{fis}(J)}{\Gamma_{tot}(J)} \times \sigma_{CN}(J) \quad (1.16)$$

where  $\Gamma_{fis}(J)$  is the fission decay width and  $\Gamma_{tot}(J) = \sum_x \Gamma_x(J) + \Gamma_{fis}(J)$ , is the total decay width for CN with spin  $J$ .  $\sigma_{CN}(J)$  is the partial cross section of fusion as given in Eq. 1.9. If we consider the saddle-point (SP) as transition state,  $\Gamma_{fis}$  will depend on the level density above the SP. Before we go to the details of level density, let us see the energy balance in fusion-fission (FF) process as a whole which has been shown schematically in Fig. 1.4 [12]. The excitation energy,  $E_{CN}^*$ , of CN is basically the sum of the incident energy,  $E_{c.m.}$  in c.m. and the entrance channel  $Q$ -value. The effective excitation energy of CN to be used to calculate its level density will be less by an amount  $\Delta_{eff}$ . The  $\Delta_{eff}$  is calculated from the assumption that the virtual ground state of the level density at high excitation energy should coincide with the ground-state energy of a spherical liquid drop [7]. The kinetic energy,  $\epsilon$ , associated with radial

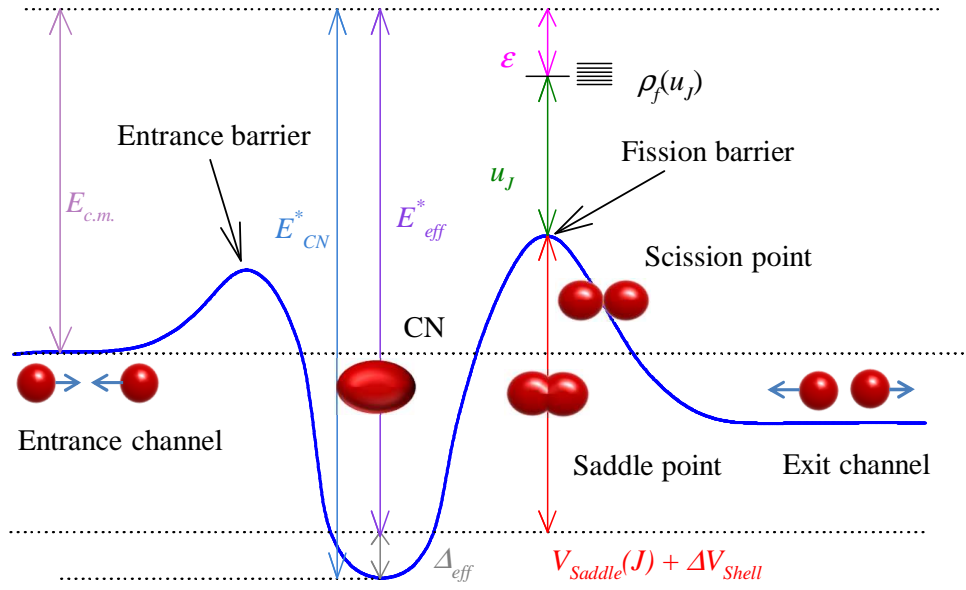


**Figure 1.4:** Energy balance is shown schematically for fusion-fission reaction.

motion at SP, further reduces level density at SP where the density of states is already minimum. The SP shell correction  $\Delta V_{shell}$  is also taken into account as it influences the fission decay probability. The excitation energy available at the SP,  $u_J$ , which determines the corresponding level density,  $\rho_{fis}$ , is then given by

$$u_J = E_{CN}^* - V_{saddle}(J, \eta) - \Delta V_{shell} - \Delta_{eff} - \epsilon \quad (1.17)$$

The probability that a CN with spin  $J$  will break up to a fission channel of mass asymmetry,  $\eta$  [ $= A_1/(A_1 + A_2)$ ], is proportional to the level density  $\rho_{fis}$  above the corresponding spin  $J$  saddle point [12]. The expression of level density is same as given in Eq. 1.13 with  $u$  as in Eq. 1.17. So, it is clear that with increase in  $V_{saddle}(J, \eta)$ , fission probability decreases for that particular mass asymmetry in the exit channel. The dependence of  $V_{saddle}(J, \eta)$  with mass asymmetry is shown in Fig. 1.5, for a light system ( $A_{CN} = 56$ , [12]) and heavy system ( $A_{CN} = 230$ ). For the lighter system, as the fission barrier is maximum at  $\eta = 0.5$ , it favours asymmetric fission over symmetric fission. On the other hand, for heavier system, the fission barrier favours symmetric fission. It is also seen that as the spin increases (for lighter system), variation of  $V_{saddle}(J, \eta)$  with  $\eta$  becomes more and more flat and the probability of symmetric increases. So, the total

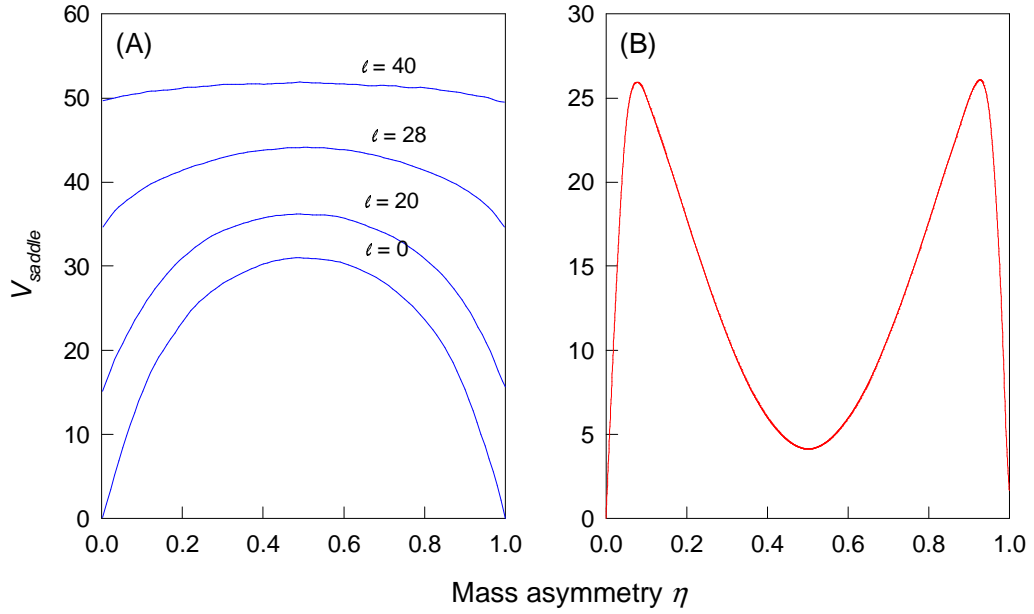


**Figure 1.5:** (A) Saddle point energies ( $V_{saddle}$ ) for light system  $A = 56$  as a function of spin and mass asymmetry, (B)  $V_{saddle}$  for heavy system  $A = 230$  as a function of mass asymmetry.

decay width of the fission is the sum of the decay widths of all individual channels,

$$\Gamma_{fiss} = \sum_{A_1} \sum_{Z_1} \Gamma_{fiss}(Z_1, A_1) \quad (1.18)$$

where  $A_1$  and  $Z_1$  are the mass and charge of the lighter fragment.

## 1.2 Deep inelastic collision

Deep inelastic reactions is a class of reaction which is intermediate between ‘complete fusion’ and ‘quasi-elastic’ processes in terms of impact parameter and energy loss as discussed earlier. In this type of reaction, a large amount of kinetic energy of relative motion is transformed into internal excitation energy. Here, after the reaction, the two fragments are re-emitted without CN formation and the emitted fragments retain the memory of entrance channel. For DI collision, two characteristic time scales may be defined: a rotational period, which corresponds to the time required for a (hypothetical) complete revolution of the two touching fragments, and ‘interaction time’

or ‘contact’ time during which the the fragments interact strongly by nuclear forces. For a particular interacting system, both these times depend on the bombarding energy, relative angular momentum,  $Q$ -value, and also on the final fragmentation [2]. In case, where interaction time is shorter than the rotational period, the angular distribution of the emitted fragments is asymmetric and it peaks around grazing angle for heavy systems. In other case, where interaction time is more than the rotational period, the angular distribution becomes symmetric around  $90^\circ$ . This situation implies the existence of an orbiting of a quasimolecular system which is indistinguishable from CN decay. Intermediate cases, when the interaction time and rotational period are comparable, the reaction product deflected to negative angle as shown in Fig. 1.1, trajectory 3A. Deep inelastic collisions are observed in both light and heavy systems, but according to characteristic features, interacting systems can be distinguished in two classes [2] as described below.

★ **Class I:** Comparatively light systems and (or) the systems with bombarding energies well above the interaction barrier belongs to this class. These systems are characterized by angular distribution which is forward peaked [in excess of  $1/\sin\theta_{c.m.}$ , falling exponentially with the increase of angle  $\theta_{c.m.}$ ]. The decay products of this class are generally spread over wide range of mass and charge. Besides DI process, a large portion of total cross section is contributed by the products of CN formation and decay.

★ **Class II:** Heavier systems and (or) the systems with bombarding energies near the interaction barrier belongs to Class II. These systems exhibit ‘side-peaked’ angular distributions (peaking around grazing angle) which steeply fall off towards larger and smaller angles. The masses and charges of the decay products are concentrated near the entrance channel. The major portion of the total reaction cross section is contributed by the DI process only.

We also have mentioned that the above classification depends on masses of the colliding ions and/or on the bombarding energy. So, a heavier system with bombarding energy well above the interaction barrier may show the characteristics of class I. Therefore, the classification of scattering systems may also be made on the basis of the ratio

of bombarding energy  $E$  and interaction energy  $B_{int}$ . If  $E/B_{int} > 1.6$ , it is assigned to class I, otherwise class II [2].

## 1.2.1 Experimental results and its theoretical interpretations

For quantitative discussion on DI process, we have to relate experimental results to its theoretical interpretation. For example, angular momentum is not a direct experimental observable, but plays an important role in the theoretical interpretation of the experimental data. Angular momentum is related to the scattering angle which is an experimental observable.

### 1.2.1.1 Deflection function

The relationship between angular momentum and scattering angle is classically expressed by ‘classical deflection function’,  $\Theta(\ell)$ , which is given by [2]

$$\Theta(\ell) = \pi - \int_{\infty}^{D_{\ell}} \left( \frac{\ell(r)}{K_{\ell}(r)} \right)_{\downarrow} \frac{dr}{r^2} - \int_{D_{\ell}}^{\infty} \left( \frac{\ell(r)}{K_{\ell}(r)} \right)_{\uparrow} \frac{dr}{r^2} \quad (1.19)$$

$$K_{\ell}(r) = \left\{ \frac{2\mu}{\hbar^2} [E_{c.m.} - V(r)] - \frac{\ell(\ell + 1)}{r^2} \right\}^{\frac{1}{2}} \quad (1.20)$$

where  $D_{\ell}$  is identical with classical turning point for angular momentum  $\ell$ ,  $K_{\ell}(r)$  and  $\ell(r)$  are local, instantaneous wave number and angular momenta at distance  $r$ . The subscript  $\downarrow$  and  $\uparrow$  denote the ingoing and outgoing part of the trajectory, respectively. Typical deflection functions for different classes of systems are illustrated in Fig. 1.6. For typical Class I systems, the deflection function looks like curve (i) where it is seen that below certain value of  $\ell$  the system starts orbiting due to the influence of the strong nuclear force. The curve (ii) represents the intermediate situation, where nuclear attraction is strong enough to cause deflection into negative angles, but it does not lead to fusion because of the strong repulsion. Deflection functions of typical Class II systems are represented by curve (iii). In this case, there is no deflection to negative angles,

and the balancing of attractive and repulsive forces causes strong focusing of trajectories having a wide range of  $\ell$  values into a very narrow angular range of deflection angles. Finally, curve (iv) represents the pure Coulomb scattering. To correlate the ex-

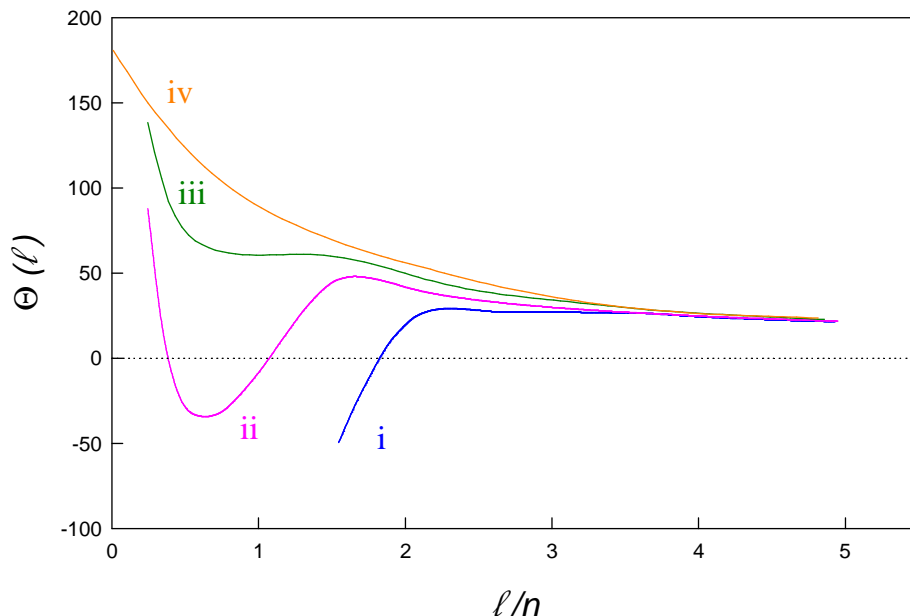


**Figure 1.6:** Different types of classical deflection function  $\Theta(\ell)$  as a function of ratio of angular momentum and Sommerfeld parameter.

perimental result with the deflection function, one should be aware that practically it is not possible to describe a system in terms of a single, well defined deflection function [2]. Actually, emergent fragments will be characterized by a distribution of deflection angles which are correlated with the distributions in energy, angular momentum, and mass partition in the exit channel. So, one should expect a ‘deflection distribution’ rather than a deflection function.

### 1.2.1.2 Kinetic energy loss

A large amount of energy of radial and orbital motion can be dissipated in DI collision. The energy loss is of the order of the difference between energy in the entrance channel and the interaction barrier in the exit channel. In other words, c.m. kinetic energy of the fragments is given by the mutual potential energy at the contact which

depends on the deformation in the exit channel. So, highest deformation leads to a maximum energy losses. This is illustrated in Fig. 1.7(a) as an example [19], where it is seen that the Coulomb energy calculated assuming spherical exit channel overpredicts the experimental data, indicating that the exit channel may not be of spherical shape. But there are many examples where the Coulomb energy calculated assum-

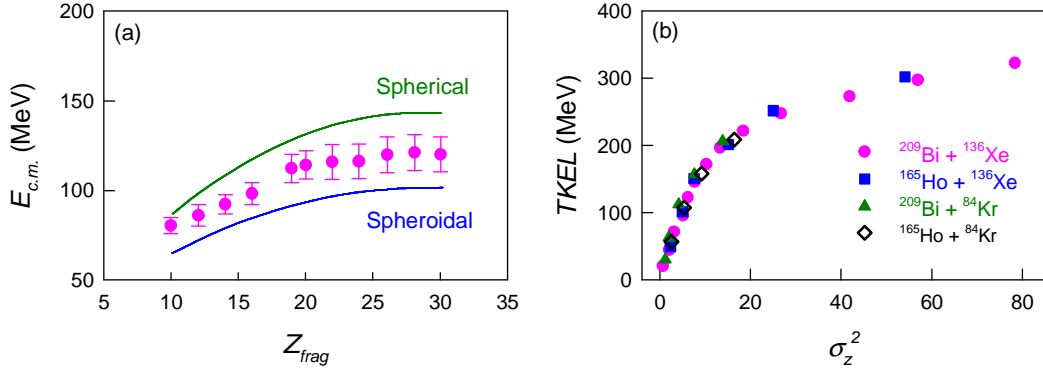


**Figure 1.7:** (a) Average kinetic energies of various fragments emitted in the reaction  $^{40}\text{Ar} + ^{197}\text{Au}$ . The solid lines represent the theoretical values expected from Coulomb repulsion of two touching spheres and of two touching spheroids. (b) Correlation between total kinetic energy loss (TKEL) and charge dispersion for the projectile-like fragments in various Kr- and Xe-induced reactions.

ing spherical exit channel predicts the experimental data (e.g., [20]). However, the interpretation of kinetic energy of the fragments emitted in DI collision is not always possible by only Coulomb potential. Examples are there that certain fraction of angular momentum may also contribute in the final kinetic energy of the emitted fragments. The magnitude of this contribution depends on the coupling between relative and intrinsic angular momenta [21]. This coupling is explained macroscopically in terms of tangential friction [2] which will be discussed later. So, it may be said that well matching of the experimental kinetic energy with the calculated one for some simple configuration of touching sphere does not always imply that the exit channel has really spherical configuration. This is because of the fact that the effect of deformation in the kinetic energy may be cancelled out by the angular momentum effect. The energy loss in damped collisions has been found to be strongly correlated to the charge dispersion

of the projectile-like fragments as shown in Fig. 1.7(b) [22]. The charge dispersion (variance,  $\sigma_z^2$ ) increases with increase in energy loss. From this correlation, it may be inferred that, nucleon exchange between the colliding ions is likely to be an important basic mechanism in the energy loss process.

### 1.2.1.3 Time of interaction

The interaction between the colliding nuclei depends on the distance and the deformation of the composite. It varies with time along the trajectory. Observable effects, like energy loss, mass and angular momentum transfer, will presumably depend on time integral over the effective interaction time, which is defined in relation to the some observable like deflection angle. A simple definition of interaction time has been introduced by Nörenberg [23]:

$$\tau(\Theta) = \frac{\Theta_{gr} - \Theta}{\bar{\omega}} = \frac{\mathcal{I}(\Theta_{gr} - \Theta)}{\hbar \bar{\ell}} \quad (1.21)$$

where  $\mathcal{I}$  is the moment of inertia of the two fragments system,  $\Theta_{gr}$  is the grazing angle,  $\bar{\omega}$  is the average angular velocity of the touching fragments; the average angular momentum,  $\bar{\ell}$ , is defined by the relation  $\bar{\ell} = 2(\ell_{gr}^3 - \ell_{cr}^3)/3(\ell_{gr}^2 - \ell_{cr}^2)$ , and,  $\ell_{cr}$  is limiting angular momentum for the fusion.

In another definition, interaction time is defined using angular distribution. The angular distribution of the fragments is explained classically by rotating dinuclear system [24, 25, 26]. Here, it is assumed that the dinuclear system rotates around an axis perpendicular to reaction plane with frequency  $\omega = \hbar\ell/\mu R^2$ , where  $\mu$  is the reduced mass of the system,  $\ell$  is the angular momentum,  $R$  represents the distance between the two centres of the di-nucleus. The angular distribution of  $d\sigma/d\Omega_{c.m.}$  can be expressed as [26, 25]

$$(d\sigma/d\Omega)_{c.m.} = (C/\sin\theta_{c.m.})e^{-\theta_{c.m.}/\omega\tau} \quad (1.22)$$

where  $C$  is a constant and  $\tau$  is the time of interaction during which the two nuclei remain in solid contact in the form of the rotating di-nucleus. The term ' $\omega\tau$ ' is called 'life angle'.

#### 1.2.1.4 Angular momentum dissipation: theoretical limit

Several models have been developed to explain the phenomena of damped nuclear reactions. These may be classified as classical scattering model and diffusion model. Here we shall discuss classical scattering model to explain the angular momentum dissipation. Classical trajectories have been widely used to represent the heavy ion collision dynamics. It has been already discussed that due to relatively short de Broglie wave length, the use of classical dynamics in heavy ion collision is justified. In clas-

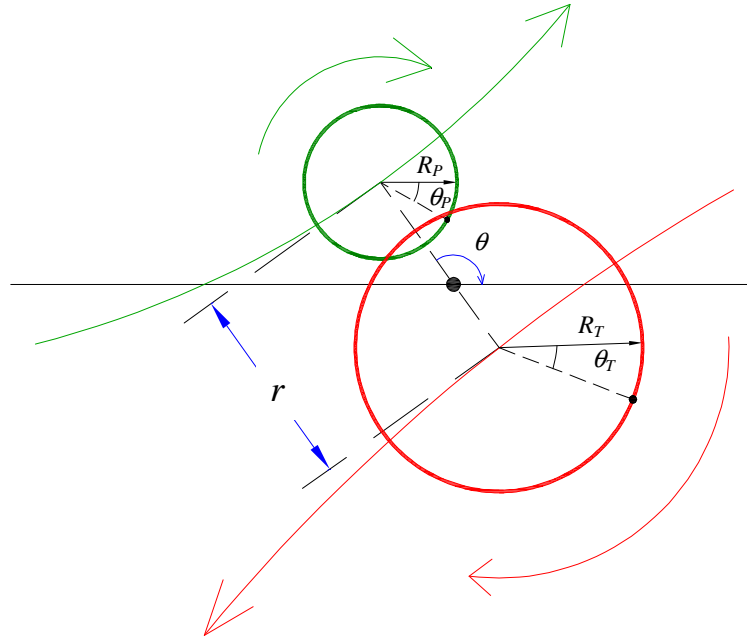


**Figure 1.8:** Reaction variables for the collision of spherical projectile (P) and target (T) nuclei.

sical scattering models, time evolution of the collective variables (a set  $\{q_i\}$  of  $n$  collective variables) are computed by solving Lagrange-Rayleigh equations numerically.

The equations are given below

$$\frac{d}{dt} \left( \frac{\partial \mathcal{L}}{\partial \dot{q}_i} \right) - \frac{\partial \mathcal{L}}{\partial q_i} = - \frac{\partial \mathcal{F}}{\partial \dot{q}_i}, \quad i = 1, 2, 3, \dots, n \quad (1.23)$$

where  $\mathcal{L}(q_i, \dot{q}_i) = T(q_i, \dot{q}_i) - V(q_i)$  is the Lagrangian, and  $\mathcal{F} = (1/2) \sum C_{ij} \dot{q}_i \dot{q}_j$  is the Rayleigh dissipation function. If it is assumed that the nuclei are rigid spheres [27] as shown in Fig. 1.8, the Lagrangian can be expressed as [28],

$$\mathcal{L} = \frac{\mu}{2} (\dot{r}^2 + r^2 \dot{\theta}^2) + \frac{\mathcal{I}_P}{2} \dot{\theta}_P^2 + \frac{\mathcal{I}_T}{2} \dot{\theta}_T^2 - V_{Coul} - V_N \quad (1.24)$$

where  $V_{Coul}$ ,  $V_N$  are the Coulomb and nuclear interaction potentials, respectively. Here, four coordinates are used to describe the collisions;  $r$  is the distance between the mass centers of the colliding nuclei, their relative orientation angles,  $\theta_P$  and  $\theta_T$ , and  $\theta$  is the orientation of the total system. The reduced mass is  $\mu = \frac{M_P M_T}{M_P + M_T}$ , and,

$$\mathcal{I}_i = \frac{2}{5} M_i R_i^2, \quad i = P, T \quad (1.25)$$

denote the rigid body moment of inertia of projectile and target with masses  $M_P$  and  $M_T$ , respectively. The dissipation function may be approximated in terms of a friction coefficient  $C_r(r)$  associated with radial motion, and the coefficient  $C_t(r)$  describing the slowing-down of the relative sliding motion of the two nuclear surfaces. Then Rayleigh function becomes

$$\mathcal{F} = \frac{1}{2} \left\{ C_r \dot{r}^2 + C_t \left( \frac{r}{R_P + R_T} \right)^2 [R_P(\dot{\theta}_P - \dot{\theta}) + R_T(\dot{\theta}_T - \dot{\theta})]^2 \right\} \quad (1.26)$$

From Eq. 1.23, one can obtain the equation of motions

$$\mu \ddot{r} - \mu r \dot{\theta}^2 + C_r \dot{r} + \frac{\partial}{\partial r} (V_{Coul} + V_N) = 0 \quad (1.27)$$

$$\mu r^2 \ddot{\theta} + \dot{I}_P + \dot{I}_T = 0 \quad (1.28)$$

$$\frac{d}{dt} (\mathcal{I}_i \dot{\theta}_i) + C_t \left( \frac{r}{R_P + R_T} \right)^2 R_i (\dot{\theta}_i - \dot{\theta}) = 0, \quad i = P, T \quad (1.29)$$

where  $I_P$  and  $I_T$  are the intrinsic spins of projectile and target, respectively, and  $\ell = \mu r^2 \dot{\theta}$  is the orbital angular momentum. From Eq. 1.29, following limits of angular momentum dissipation can be obtained. When two nuclei are rolling on each other,

without any rolling friction,  $R_P(\dot{\theta}_P - \dot{\theta}) = R_T(\dot{\theta} - \dot{\theta}_T)$ . In such condition, final angular momentum (rolling limit) becomes,

$$\ell_{roll} = \frac{5}{7}\ell \quad (1.30)$$

In addition, if rolling friction is also there, then angular momentum dissipation continues till sticking condition occurs i.e.,  $\dot{\theta}_P = \dot{\theta}_T = \dot{\theta}$ , is reached, which is similar to the rigid rotation of the dinuclear system. The final angular momentum under this condition (sticking condition) becomes,

$$\ell_{stick} = \frac{\mathcal{I}}{\mathcal{I} + \mathcal{I}_P + \mathcal{I}_T}\ell \quad (1.31)$$

where  $\mathcal{I} = \mu r^2$  is the moment of inertia for the orbital motion of two nuclei with reduced mass  $\mu$ .

### 1.3 Dinuclear orbiting

Two colliding nuclei with suitable energy and angular momentum may be trapped in the interaction potential that exhibits a pocket as a function of the distance between their centers and a dinucleus is formed. This dinucleus may evolve with complete amalgamation into a fully equilibrated CN which may decay by fission as discussed above. Another possible evolution of this dinucleus is that it may escape into a binary exit channel by way of orbiting trajectory. Binary decay of second process is called dinuclear orbiting or simply orbiting. The conceptual difference between FF and orbiting for the light systems is shown schematically in Fig. 1.9 [12]. The fragments coming from fission decay of CN depends on the phase space available at the ‘transition’ configuration. For light systems, fission decay leads to significant population of large number of energetically allowed mass channels. On the other hand, in orbiting, the system trapped in a more deformed configuration than the CN and inhibited to spread into CN states. Before it is fully equilibrated with respect to all degrees of freedom, it decays back to the binary channels. Orbiting is also considered as a kind

of deep inelastic process, but in the light systems, due to rapid mass exchange, the exit channel has significantly different mass asymmetry than the entrance channel. Still, it is expected that the orbiting mechanism will retain a greater memory of the entrance channel than the FF. So, orbiting acts as a ‘door way’ state to the fusion with strong memory of entrance channel [12, 29]. In deep inelastic collisions between relatively heavy ions, partial orbiting of interacting nuclei is well documented [30]. D. Shapira *et al.*, first time observed a strong enhancement in the cross section for the inelastic scattering in light  $\alpha$ -cluster system  $^{12}\text{C} + ^{20}\text{Ne}$  [31, 32] and resonance-like structure in the excitation function of the total yield of carbon. They used the phenomenon of orbiting to explain their experimental data for this light system also. They further claimed this mechanism as the origin of backward angle enhancement of elastic scattering [33, 34, 35] in  $\alpha$ -cluster nuclei, which was earlier explained by number of ways, such as Regge poles, resonances, parity dependent potentials, diffraction and particle exchange [31]. The peak of energy spectra of the inelastic channels of  $^{12}\text{C} + ^{20}\text{Ne}$  was found to be the same as  $^{12}\text{C}$  and  $^{20}\text{Ne}$  fragments are emitted from a equilibrated CN. The average  $Q$ -value,  $\langle Q \rangle$ , have a constant value over the all measured angles for a particular beam energy and it varies linearly with the beam energy; further, the angular distribution is also proportional to  $1/\sin\theta_{c.m.}$  [31] which suggest that long-lived intermediate complex is formed. As the enhanced yield in the backward angles cannot be explained by statistical model, it was suggested that an orbiting dinuclear configuration is formed which preferentially decays back to the entrance channel [12]. Similar enhancement in the binary yield was observed in  $\alpha$ -cluster system  $^{28}\text{Si} + ^{12}\text{C}$  [36]. Here, in addition to carbon yield, enhancement was also observed in non- $\alpha$ -conjugate channels B, N and O yields also. Enhancement in the yields were also observed at large angle in heavier systems,  $^{28}\text{Si} + ^{28}\text{Si}$  [37, 38] and  $^{24}\text{Mg} + ^{24}\text{Mg}$  [39]. In this two  $\alpha$ -cluster systems, strong resonance-like structures were observed in the angle-integrated excitation functions of elastic and inelastic channels.

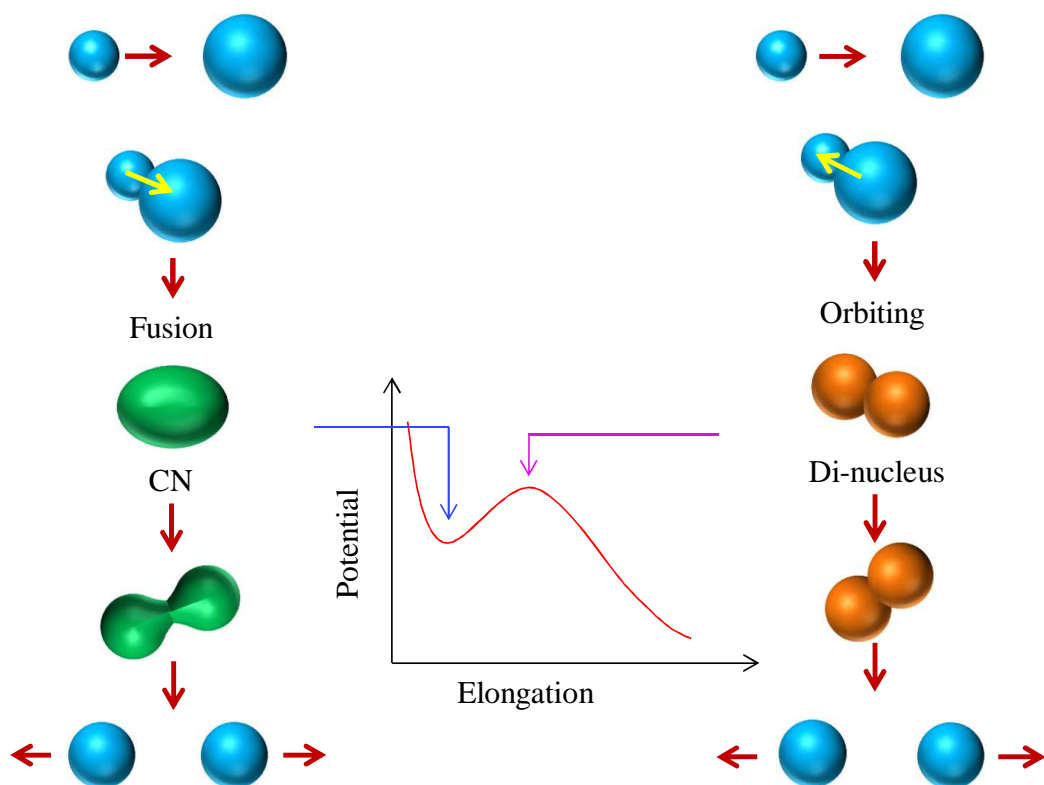


**Figure 1.9:** Difference between fusion-fission (left column) and orbiting (right column) mechanism is shown.

### 1.3.1 Equilibrium orbiting model

As we discussed above, binary reaction yields for a number of systems, like  $^{12}\text{C} + ^{20}\text{Ne}$  [31, 32],  $^{24}\text{Mg} + ^{24}\text{Mg}$  [39],  $^{28}\text{Si} + ^{12}\text{C}$  [36],  $^{28}\text{Si} + ^{28}\text{Si}$  [37, 38],  $^{28}\text{Si} + ^{14}\text{N}$  [29, 40],  $^{24}\text{Mg} + ^{12}\text{C}$  [41] have been explained in terms of the formation and decay of long-lived orbiting dinuclear complex. B. Shivakumar *et al.*[29] proposed a model to explain the experimental data coming from dinuclear orbiting and fusion in terms of evolution of dinuclear molecular complex (DMC) within the framework of extended diffusion model. Such a DMC often acts as a doorway state in the formation of completely equilibrated CN [29]. It is formed after damping of energy and angular momentum and evolves rapidly through the exchange of nucleons to different configuration and subsequently decays partially by fragmentation (orbiting) and partially by CN formation [3]. The model is an approximation of full transport theory that

assumes  $P_\ell(N, Z)$ , the probability of fragmentation of DMC into a channel  $(N, Z)$  and angular momentum  $\ell$ , can be expressed as product of transition probability and phase space factors [29]. The phase space factors are the level densities of DMC in equilibrium and scission. The transition probability is taken as constant as it varies relatively very slowly with energy with respect to the phase space factors. The probability of fragmentation of DMC is given by,

$$P_\ell(N, Z) = \frac{\rho_\ell(N, Z; R_B)}{\sum_{N', Z'} \rho_\ell(N', Z'; R_M) + \rho_\ell(N', Z'; R_B)} \Big|_{(Z, Z' > 2)} \quad (1.32)$$

where  $\rho_\ell(N, Z; R_B)$  and  $\rho_\ell(N', Z'; R_M)$  are the level densities of DMC at excitation energies evaluated at the top of the potential barrier  $R = R_B$  and the minimum potential at  $R = R_M$ , respectively. The potential energy surface of DMC which is used to calculate the density of states using Fermi level density is given below [29]

$$U_J(N, Z; R) = V_N(N, Z; R) + V_C(N, Z; R) + \frac{\hbar^2}{2 \mathcal{J}_{tot}(N, Z; R)} J(J + 1) + Q(N, Z) \quad (1.33)$$

Here  $\mathcal{J}_{tot}$  is the total moment of inertia of in the sticking limit,  $J$  total angular momentum,  $Q(N, Z)$  is the ground state  $Q$ -value of the entrance channel with respect to the fragmentation  $(N, Z)$ .  $V_N(N, Z; R)$  and  $V_C(N, Z; R)$  are the nuclear and Coulomb potentials. The total fragmentation probability into a exit channel  $(N, Z)$  (orbiting cross section) can be written as

$$P(N, Z) = \pi \lambda^2 \sum_{\ell=0}^{\ell_{max}} (2\ell + 1) P_\ell(N, Z) \quad (1.34)$$

where  $\ell_{max}$  is the maximum angular momentum for which system can be trapped in the pocket of interaction potential. The average kinetic energy of the fragment  $(N, Z)$  can be given as

$$KE(N, Z) = \pi \lambda^2 \sum_{\ell=0}^{\ell_{max}} (2\ell + 1) \left[ U_0(N, Z; R_B) + \frac{\hbar^2}{2 \mathcal{J}_{rel}(N, Z; R_B)} f^2 - Q(N, Z) \right] \frac{P_\ell(N, Z)}{P(N, Z)} \quad (1.35)$$

where  $f = \mathcal{J}_{rel}(N, Z; R_B) / \mathcal{J}_{tot}(N, Z; R_B)$  and  $\mathcal{J}_{rel}$  and  $\mathcal{J}_{tot}$  are the relative and total moment of inertia at  $R = R_B$  (saddle point).  $U_0(N, Z; R_B)$  is the nuclear and Coulomb contribution to the potential energy for  $\ell = 0$  [29]. The equilibrium orbiting model has

been found to successfully reproduce the total average kinetic energy as well as cross section of fully damped fragments for several light systems [12]. The only adjustable parameters in the calculations are those to determine the nuclear potential and the level density [29].

### 1.3.2 Number of open channel

The orbiting and resonance contributions of the reaction yields occur because of the weak absorption of the partial waves near grazing angular momentum. This ‘surface transparency’ may be related to the number of open reaction channels (NOC) in lighter systems [42]. In light heavy-ion systems a strong correlation has been observed between the existence of very low NOC and the occurrence of resonant behavior and back angle enhancement in the elastic, inelastic, or a transfer channels [43]. For example, significant evidence of orbiting process has been observed in the system  $^{24}\text{Mg} + ^{16}\text{O}$  for which NOC is small. On the other hand, binary fragment yields for the systems  $^{35}\text{Cl} + ^{12}\text{C}$  [44] and  $^{23}\text{Na} + ^{24}\text{Mg}$  [45] which, have large NOC, have been found to be consistent with the predictions of fusion-fission like process.

The NOC for a given system is obtained by the triple summation over all possible two-body mass partition in the exit channels, over all possible angular momentum couplings and on all possible energy sharing between the the fragments which is written as [43]

$$N^J(E_{c.m.}) = \sum_{\substack{A_1+A_2=A_{CN} \\ A_1 \leq A_2}} \sum_{J=I_1+I_2+\ell} T_\ell(E_r) \quad (1.36)$$

where  $E_{c.m.}$  is the incident c.m. energy and  $E_{ex}$  is the excitation energy of the compound system.  $I_1$ ,  $I_2$  and  $\ell$  are the intrinsic spins of the fragments and the angular momentum of their relative motion.  $E_1$ ,  $E_2$  and  $E_r$  are the intrinsic energies of the fragments and the energy available for their relative motion.  $Q_{12}$  is the reaction ground state  $Q$ -value of the decay into two fragments.  $T_\ell(E_r)$  is the transmission coefficient of the outgoing channel as a function of  $\ell$  and  $E_r$ . The transmission coefficients have been calculated

using semiclassical model of the inverted parabolic penetration approximation,

$$T_\ell(E_r) = \frac{1}{1 + \exp\left[\frac{2\pi\{V_\ell(R_B) - E_r\}}{\hbar\omega_\ell}\right]} \quad (1.37)$$

where

$$\hbar\omega_\ell = \hbar \left[ \frac{1}{\mu} \left\{ \frac{d^2 V_\ell(R)}{dR^2} \right\}_{R=R_B} \right]^{1/2} \quad (1.38)$$

is related to the curvature of the potential barrier. In this expression  $\mu$  is the reduced mass and  $V_\ell(R)$  is the the total real potential including the Coulomb potential, nuclear potential and centrifugal term.  $R_B$  is the distance between the centers of the dinuclear molecule at the top of the barrier where  $[dV_\ell(R)/dR]_{R=R_B} = 0$  [43]. The sum over energy sharing between the fragments employs discrete energy levels at low energy and at higher energies, level density expression is used [43]. The expression  $N^J(E_{c.m.})$  is similar to the expression of the HF formalism of CN, but here direct reaction channels are included along with fusion evaporation channels and phase space calculation is extended to the incident angular momentum beyond the critical angular momentum of fusion  $\ell_{cr}$ . To compare the NOC for the different systems, it is useful to normalize NOC by the total incident flux. The normalized NOC is expressed as  $N/F = N^J(E_{c.m.})/F^J(E_{c.m.})$ , number of open channels per mb, where  $F^J(E_{c.m.})$  is the incident flux for the total angular momentum  $J$  which given by the expression

$$F^J(E_{c.m.}) = \pi\lambda^2 \frac{2J+1}{(I_P+1)(I_T+1)} \sum_{J=\ell+I_P+I_T} T_\ell(E_{c.m.}) \quad (1.39)$$

where  $I_P$  and  $I_T$  are the intrinsic spins of the incident particles. In the case of spin zero particles,  $N/F$  is calculated for  $J = \ell_{gr}$ , grazing angular momentum, and parity  $(-1)^{\ell_{gr}}$ , whereas for the particles with non-zero spin,  $J$  is taken as largest possible  $J$  values and parity is given by the product of intrinsic parities and  $(-1)^{\ell_{gr}}$ .

A few examples of NOC calculations as a function of grazing angular momentum are given in Fig. 1.10 (a)[46] and (b)[43]. In all systems,  $N/F$  initially decreases with increase of  $\ell_{gr}$  and then increases again. The initial drop is due to the increasing difficulty the compound system has in accommodating the largest angular momenta

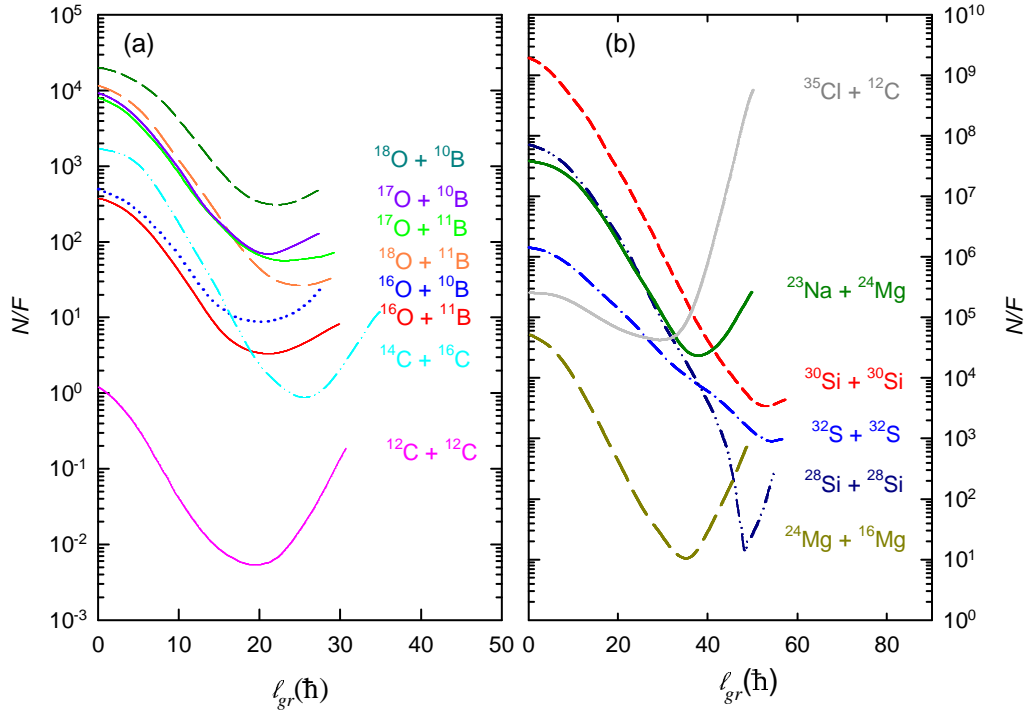


**Figure 1.10:** Variation of NOC with  $\ell_{gr}$  for different systems.

by the evaporation of the light particle alone. Subsequent rise, is due to increase in number of direct channel, such as single and mutual inelastic excitation, nucleon and  $\alpha$ -transfer and, finally, deep-inelastic orbiting and fusion-fission processes, becomes effectively open [43].

A strong correlation is there between small value of  $N/F$  and the quasimolecular resonance in light and medium heavy-ion reactions [43]. For example, prominent resonance is observed in  $\alpha$ -like system  $^{12}\text{C} + ^{12}\text{C}$  and at the same time it has a minimum value of  $N/F$  which is  $\approx 0.1$  only as shown in Fig. 1.10(a); for this system orbiting yield is expected [46]. On the other hand, for non  $\alpha$ -like O + B systems, minimum value of  $N/F$  more than  $10^4$ . In this case, large value of NOC is associated with the occurrence of fusion-fission processes [46]. For more heavier  $\alpha$ -cluster system  $^{28}\text{Si} + ^{28}\text{Si}$ , prominent narrow structure was seen in the excitation function [37, 38, 47] and NOC has a minimum value of  $\sim 10$  [43]. It may be noted here that, for heavier system minima of NOC has shifted to the higher spin. For  $^{12}\text{C} + ^{12}\text{C}$  system it happens at

$\ell_{gr} \approx 19\hbar$  whereas for  $^{28}\text{Si} + ^{28}\text{Si}$  system, the same is at  $\ell_{gr} \approx 47\hbar$ . For more heavier system,  $^{32}\text{S} + ^{32}\text{S}$ , minima has a tendency to disappear where CN cannot sustain angular momenta larger than  $49\hbar$  according to the modified liquid drop model [48] and the system does not show any resonance like feature [49]. The non  $\alpha$ -like systems are known to be much less surface transparent. For an example, the systems  $^{28}\text{Si} + ^{30}\text{Si}$  and  $^{30}\text{Si} + ^{30}\text{Si}$  do not show structures in the excitation function and NOC is found to be significantly larger than  $^{28}\text{Si} + ^{28}\text{Si}$  [43]. Although the resonance behavior appears to be a common feature in light- and medium-light heavy-ion systems, its observation is restricted to the reactions involving  $\alpha$ -cluster nuclei and other closed shell nuclei with a small NOC value. Though  $^{14}\text{C}$  is not an  $\alpha$ -like nucleus, the  $^{14}\text{C}$  induced reactions with other  $\alpha$ -like nuclei, for example,  $^{14}\text{C} + ^{16}\text{O}$  have small NOC. The weak absorption due to small NOC value permitted the quasimolecular resonance structures to show up in the experimental inelastic and quasielastic channels of the  $^{12}\text{C} + ^{12}\text{C}$ ,  $^{14}\text{C} + ^{14}\text{C}$  and  $^{14}\text{C} + ^{16}\text{O}$  [42].

## 1.4 Motivation

Nowadays it is well known that the origin IMF is broadly fusion-fission and non-fusion (deep inelastic, quasi elastic, breakup, etc.) processes. To search the origin of IMF, intense studies have been done both theoretically [17, 50, 51, 52, 53, 54, 55, 56] and experimentally [12, 26, 29, 31, 32, 57, 58, 59, 60, 61, 62, 63, 64, 65, 66, 67, 68, 69, 70, 71, 72, 73, 74, 75, 76, 77, 78, 79, 80, 81, 82, 83, 84, 85] for the last few decades in heavy-ion as well as light-ion systems. But the origin is still not well understood, particularly in light-ion systems (typically,  $A_{\text{projectile}} + A_{\text{target}} \lesssim 60$ ) at moderate bombarding energy ( $E_{\text{lab}} \lesssim 10 \text{ MeV/A}$ ). This might be due to the strong overlap between elemental yields of different processes. Situation becomes more complicated in the reactions involving  $\alpha$ -cluster systems, where nuclear structure is also known to play an important role in the equilibrium emission of complex fragments. In these cases, in addition to the standard fusion-fission route of fragment emission, the projectile and

the target have a finite probability to form a long-lived dinuclear composite, which directly undergoes scission (without the formation of the fully equilibrated compound nucleus) to emit complex fragments. This process, termed as nuclear orbiting [29], has been shown to contribute significantly to the fragment yield in many reactions involving light  $\alpha$ -cluster nuclei (e.g.,  $^{20}\text{Ne} + ^{12}\text{C}$  [70, 73, 31, 32],  $^{24}\text{Mg} + ^{12}\text{C}$  [85],  $^{28}\text{Si} + ^{12}\text{C}$  [83, 84] etc.) as discussed above.

The aim of the present thesis was to study the reaction mechanism of IMF emission in light  $\alpha$ - and non  $\alpha$ -cluster systems ( $A_{CN} \leq 40$ ) in general, and to investigate into the role played by orbiting in light  $\alpha$ -cluster systems at moderate bombarding energy ( $E_{lab} \lesssim 10$  MeV/A), in particular. Two experiments have been performed under the present Ph.D programme. In the first experiment, the reaction mechanism of IMF emission and its evolution with bombarding energy have been studied in  $\alpha$ -cluster system  $^{16}\text{O} + ^{12}\text{C}$ . Quadrupole deformation parameter of the composite system ( $^{28}\text{Si}^*$ ) has been estimated from the comparison of slopes of the light charged particle spectra with the same obtained from statistical model predictions. In the second experiment, the emission processes of IMF have been studied in  $\alpha$ -cluster system  $^{12}\text{C} + ^{28}\text{Si}$  and the neighbouring non  $\alpha$ -cluster systems  $^{11}\text{B} + ^{28}\text{Si}$  and  $^{12}\text{C} + ^{27}\text{Al}$ , all having same excitation energy  $\sim 67$  MeV, in order to look into the roles played by various IMF emission process in these reactions. In addition, a large reaction chamber has been developed for reaction mechanism studies, which is also part of this thesis.

Recently, a detailed study of the competition between direct and dissipative processes in binary channels in the systems  $^{16}\text{O} + ^{12}\text{C}$ ,  $^{18}\text{O} + ^{12}\text{C}$  have been made by S. Szilner *et al.* [72] in the energy range 5 - 7.7 MeV/nucleon. For both the systems, resonant structure has been observed at lower energies and refractive effects at higher energies, which may be considered as the signature of the orbiting process. In the present work, we report a study of fragment emission from  $^{16}\text{O} + ^{12}\text{C}$  reaction in the bombarding energy range  $\sim 7 - 10$  MeV/nucleon with the aim to explore the role of different mechanisms (fusion-fission, deep inelastic orbiting, etc.) in the yields of various exit channels. Significant mass and charge transfer occur during the course of

evolution of the rotating dinuclear complex, which leads to typical deep-inelastic reaction yields. Therefore, the study of the rearrangement channels offers a special interest in probing the dynamics of long-lived dinuclear complexes. For a better understanding of the orbiting process, it is important to study how the orbiting process evolves with energy. With this motivation, a detailed study of fragment energy spectra have been made for the reaction  $^{16}\text{O} + ^{12}\text{C}$  at different bombarding energies viz.  $E_{\text{lab}} = 117, 125, 145$  and  $160$  MeV, respectively. As orbiting process always associated with large deformation, detail study of the energy and angular distributions of  $\alpha$ -particles, emitted in the reactions  $^{16}\text{O}$  (117, 125, 145 and 160 MeV) +  $^{12}\text{C}$ , have also been studied to measure the deformation.

In recent years, a few studies have been made on the  $\alpha$ -cluster system  $^{40}\text{Ca}^*$  and the neighboring non- $\alpha$ -cluster systems to look into the relationship between equilibrium emission of fragment (and *vis-à-vis* orbiting) and  $\alpha$ -clustering. From the study of fragment emission ( $6 \leq Z \leq 8$ ) in the inverse kinematical reaction  $^{28}\text{Si} + ^{12}\text{C}$  at energies  $29.5 \text{ MeV} < E_{c.m.} < 50 \text{ MeV}$  [84], it has been conjectured that orbiting played a crucial role in fully energy-damped fragment emission. Even for the non  $\alpha$ -cluster system with  $A_{CN} \simeq 42$  ( $^{28}\text{Si} + ^{14}\text{N}$ ), where the NOC was large compared to that of  $^{28}\text{Si} + ^{12}\text{C}$  [43], the yields of fully energy damped fragments ( $6 \leq Z \leq 8$ ) were found to have contributions, though smaller in magnitude, from the orbiting process [86, 40, 87]. It will, therefore, be worthwhile to study the emission of lighter fragments ( $Z < 6$ ) in particular, for systems around  $A_{CN} \simeq 40$ , to extract the contributions of different emission mechanisms, which will be partly complementary to the earlier measurements. Here, we have studied the light fragment ( $3 \leq Z \leq 5$ ) emission from  $\alpha$ -cluster system ( $^{40}\text{Ca}^*$ ) produced in  $^{12}\text{C}$  (77 MeV) +  $^{28}\text{Si}$  reaction, as well as those from the neighboring composite system  $^{39}\text{K}^*$  produced at the same excitation energy ( $\sim 67$  MeV) via two different reaction channels,  $^{11}\text{B}$  (64 MeV) +  $^{28}\text{Si}$  and  $^{12}\text{C}$  (73 MeV) +  $^{27}\text{Al}$ ; the last two reactions have been chosen to crosscheck the equilibrium decay nature (absence of entrance channel dependence) of the energy damped binary fragment yield in the

decay of  $^{39}\text{K}^*$ . The time scales and the angular momentum dissipation factors for DI fragment emission in these reactions have also been studied.

A K500 Superconducting Cyclotron (SCC) has been built at VECC, which will enable front line nuclear physics research in the Fermi Energy domain. Several large experimental facilities are being built as a part of the SCC utilization program. These facilities may also be used to continue IMF emission study in the Fermi energy domain. One of the important part of the facility is to develop a large (1m diameter, 2.2m long) scattering chamber. The design, development, installation, testing of this the large multipurpose high vacuum ( $\sim 10^{-7}$  mbar) reaction chamber is also part of the present thesis.

## Chapter 2

# Experimental setup and data analysis technique

The main goal of the thesis is to study the emission mechanism of intermediate mass fragments (IMFs) in low energy ( $\lesssim 10\text{MeV/A}$ ) heavy-ion reactions involving light nuclei ( $A_{proj} + A_{targ} \lesssim 50$ ) in general and light  $\alpha$ -cluster nuclei in particular. Two sets of experiments have been performed for this purpose. The first experiment has been performed at Variable Energy Cyclotron Centre (VECC), Kolkata, to study the mechanism of IMF emission in  $\alpha$ -cluster system  $^{16}\text{O} + ^{12}\text{C}$  at different energies. As this system known to show orbiting behaviour at low excitations, the experiment was also aimed to look for the signature of survival of orbiting at these energies. For that purpose, in addition to IMF measurement, light charged particle (LCP) emission has also been studied to get information about the deformation of the excited composite. The second experiment has been done using heavy ion beam from BARC-TIFR pelletron facility at Mumbai. In this experiment, the emission mechanism of IMF has been studied for the  $\alpha$ -clustered system  $^{12}\text{C} + ^{28}\text{Si}$  and compared the same with two nearby systems  $^{12}\text{C} + ^{27}\text{Al}$  and  $^{11}\text{B} + ^{28}\text{Si}$  all at same excitation energy, to look for any indication of the existence of orbiting in  $^{12}\text{C} + ^{28}\text{Si}$  system. The discussion about the experimental setups and data analysis method has given here in a general way.

## 2.1 Accelerators

### 2.1.1 Variable energy cyclotron

It is an azimuthally varying field (AVF) cyclotron with pole diameter of 224 cm. As per design specification, the accelerated beam energy is  $130(Q^2/A)$  MeV where  $Q$  and  $A$  are the charge state and the atomic mass of the accelerated beam, respectively. Details of the machine have been given in Table 2.1. Fig. 2.1 shows the view of

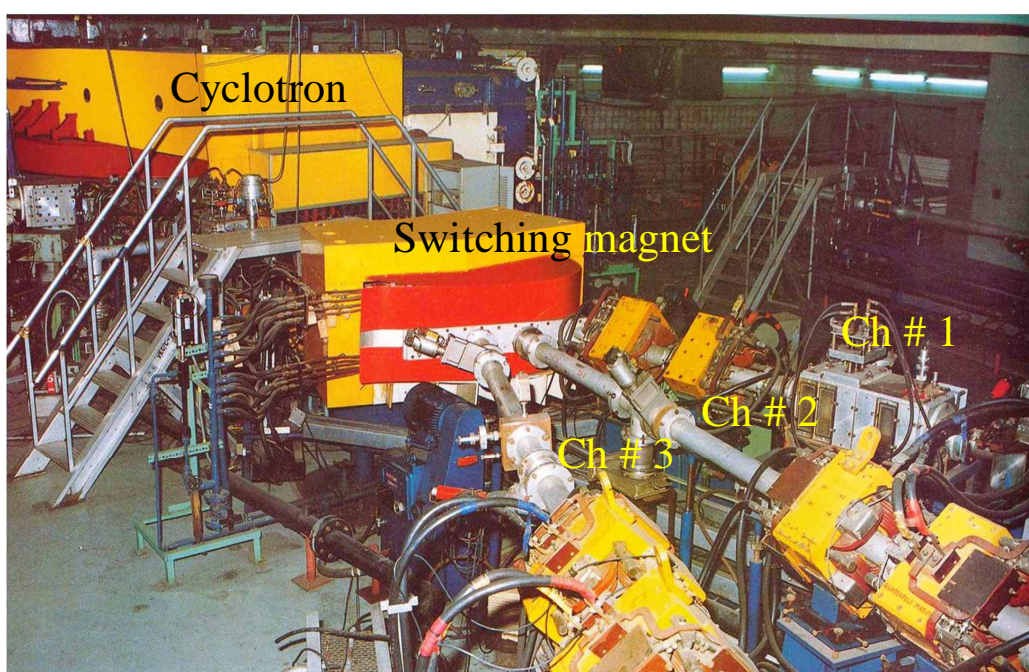


*Figure 2.1: K130 variable energy cyclotron.*

the cyclotron with the switching magnet and the beam lines. Details of the beam line layout have been shown in Fig. 2.2. The  $0^0$  beam line (Ch# 1) is used for high current (irradiation) experiments. The general purpose scattering chamber, where the present experiment has been performed, is placed in the second beam line (Ch# 2) for charged particle experiments. Experiments with  $\gamma$ -detectors are performed in the third beam line (Ch# 3). The fourth beam line (Ch# 4) has been dedicated to the radioactive ion beam (RIB) facility as shown in Fig. 2.2.

**Table 2.1:** *Technical specifications of K130 cyclotron.*

<b>Cyclotron</b>	
Cyclotron type	: AVF
<b>Magnet</b>	
Shape	: H-shaped electromagnet
Pole diameter	: 224 cm
Average pole gap	: 24.5 cm
Average magnetic field	: 17.1 kG
Main coil power	: 490 kW
Trim coil power	: 433 kW
Valley coil power	: 27 kW
<b>R. F. System</b>	
Frequency range	: 5.5 - 16.5 MHz
Dee Voltage	: 70 kV (max)
Energy gain	: 140 keV /turn (max)
Oscillator power output	: 300 kW (max)
<b>Ion Source</b>	
Type	: Hot cathode PIG, ECR
Filament current	: 500 A (max)
Arc current	: 0- 2 A
Arc voltage	: 10 - 600 V
<b>Deflector</b>	
Type	: Electrostatic 120 kV (max)
<b>Vacuum</b>	
Operating pressure	: $10^{-6}$ Torr
<b>Beam</b>	
Energy	: Proton 6 - 30 MeV : Deuteron 12 - 65 MeV : Alpha 25 - 130 MeV : Heavy ion 7-11 MeV/A
Internal beam current	: 100 $\mu$ A
External beam current	: 20 $\mu$ A
Extraction radius	: 99 cm
Resolution	: 0.5% (FWHM)
Beam pulse width for particles	: 4 ns

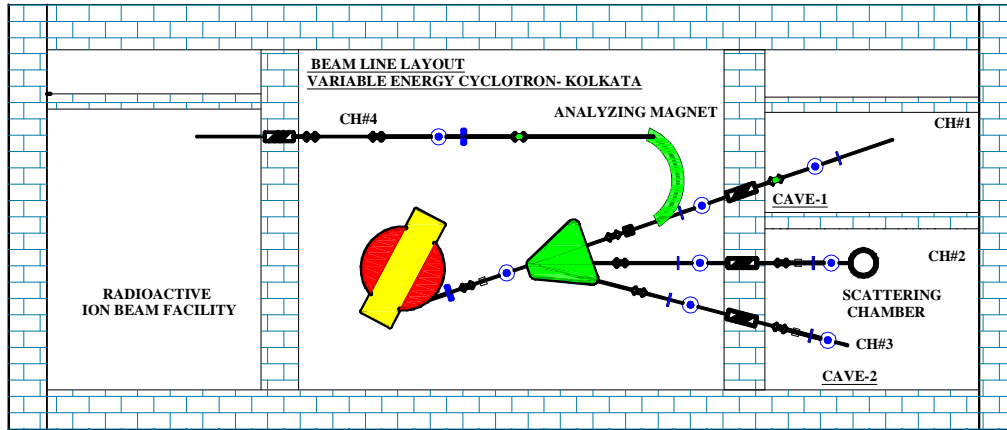


*Figure 2.2: Beam line layout of K30 variable energy cyclotron.*

## 2.1.2 BARC-TIFR Pelletron

It is a 14 Million Volt (MV) tandem electrostatic accelerator which can accelerate  $p$ ,  $\alpha$  and various heavy ions [88]. A schematic diagram of the accelerator with beam line layout is shown in Fig. 2.3. At the top, there is an ion source (Source of Negative Ions by Cesium Sputtering - SNICS) which produces negative ion ( $1^-$ ). This low energy ion is bent vertically downwards by a  $90^\circ$  injector magnet. At the same time, by choosing proper magnetic field, a particular isotope can also be selected. Due to the high voltage terminal at the middle, the negative ion is accelerated and it gains energy of amount  $V_T$ , where  $V_T$  is the terminal voltage (in Million Volts). At this terminal, negative ion is stripped by a carbon stripper foil and becomes a positive ion with charge  $q$ , which is then repelled by the high voltage terminal towards the ground voltage. This results in the energy of ion  $E = (q + 1)V_T$  MeV. Then, an analyzing magnet ( $90^\circ$ ) bends the beam horizontally and at the same time it selects a particular charge state of accelerated ion with energy

$$B = 720.76 \frac{\sqrt{AE}}{q} \quad (2.1)$$

where the magnetic field,  $B$ , is in Gauss and  $E$  in MeV. This beam (energy resolution  $\Delta \approx 2\text{KeV}$ ) is then switched between one of the five experimental beam lines using a switching magnet. The general purpose scattering chamber (SC), where the second

experiment has been done, is placed in the  $0^0$  beam line as shown in Fig. 2.3. A separate beam line is there for super conducting LINAC booster details of which are not discussed here.

## 2.2 Experimental setups

As mentioned earlier, two experiments have been performed in the two accelerators; the IMF and LCP emission from the reactions  $^{16}\text{O}$  ( $\sim 7\text{-}10$  MeV/A) +  $^{12}\text{C}$  have been studied using the cyclotron at VECC, and the IMF emission from the reactions  $^{12}\text{C}$  (77 MeV) +  $^{28}\text{Si}$ ,  $^{12}\text{C}$  (73 MeV) +  $^{27}\text{Al}$ ,  $^{11}\text{B}$ (64 MeV) +  $^{28}\text{Si}$  have been studied using Pelletron accelerator at Mumbai. Similar types of experimental setups have been used in both the experiments; the experiments involved with the measurement of charged particles. The schematic diagram of the setup is shown in Fig. 2.4(a). The charged particle detectors have been housed in a suitable scattering chamber. All the experimental signals have been collected and processed by using standard electronics and CAMAC based data acquisition system.

### 2.2.1 Scattering chambers

Both the scattering chambers (at VECC and BARC-TIFR pelletron) used in the present experiments are similar. The scattering chamber at VECC as well as Pelletron lab are cylindrical in shape with diameter  $\sim 1\text{m}$ . Both of them have two rotating arms on each side of the beam direction which can be rotated from outside so that the detectors can be placed at any angle in between  $\sim 8^0\text{-}170^0$ . Each arm, which is in the form of a plate, is provided with many fixed holes at different angular and radial positions to keep the detector at a particular position. In both the cases, the target ladder is at the centre of the chamber, which can hold several targets, and, by moving the ladder from outside, any of the targets may be brought to the beam position. The operative vacuum in the cyclotron chamber is  $\sim 1\text{-}2 \times 10^{-5}$  mbar and the same for pelletron chamber,

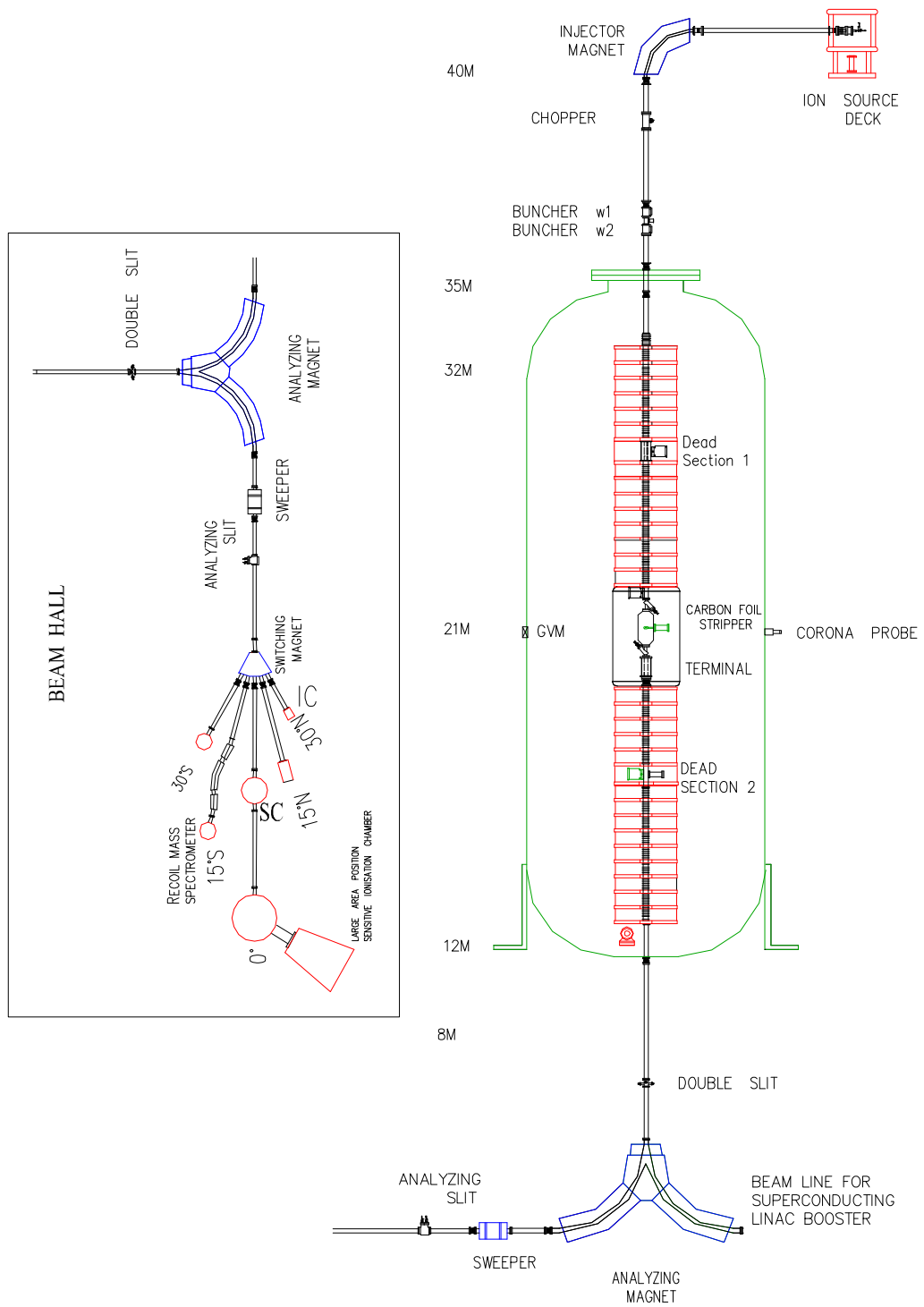


Figure 2.3: Accelerator and beam line layout of TIFR-BARC pelletron.

is  $\sim 4\text{-}5 \times 10^{-6}$  mbar. In both cases, the vacuum is achieved with the help of large diffusion pump and rotary pump combination. The detector signals are taken out using BNC vacuum feed-throughs provided at the wall of the chamber. Schematic view of experimental setup along with scattering chambers are shown in Fig. 2.4.

## 2.2.2 Charged particle telescopes: particle identification

Different combinations of silicon detectors (surface barrier or lithium drifted), ionization chamber and the CsI(Tl) detector have been used in the present experiment in  $\Delta E$ - $E$  telescopic mode to detect and identify the emitted fragments and measure their energy distributions. The working principle of this type of telescope is based on Bethe formula [89] which describes the specific energy loss of an incident charged particle on a particular material and is written as

$$-\frac{dE}{dx} = \frac{4\pi e^4 z^2}{m_0 v^2} NB \quad (2.2)$$

where

$$B = Z \left[ \ln \frac{2m_0 v^2}{\mathcal{W}} - \ln \left( 1 - \frac{v^2}{c^2} \right) - \frac{v^2}{c^2} \right] \quad (2.3)$$

$E (= \frac{1}{2} M v^2)$ ,  $v$ ,  $ze$ ,  $M$  are the energy, velocity, charge and mass of the incident particle and  $N$ ,  $Z$  are the number density and atomic number of the absorber (here detector material) and  $m_0$ ,  $e$  are the mass, charge of electron, respectively. The parameter  $\mathcal{W}$  represents the average excitation and ionization potential of the absorber and normally treated as an experimentally determined parameter for each element. For non-relativistic particle ( $v \ll c$ ), the second and third terms of  $B$  are negligibly small and whole  $B$  varies very slowly with the energy of the incident particle. So, the Eq. 2.2 reduces to

$$-\frac{dE}{dx} \approx \frac{Mz^2}{E} K \quad (2.4)$$

where  $K \approx$  constant. In the case of a two detector telescope which consists of one thin detector followed by a thick detector such that the energy loss of the particle in this thin detector ( $\Delta E$ ) is small compared to the total energy ( $E$ ). Under such condition,

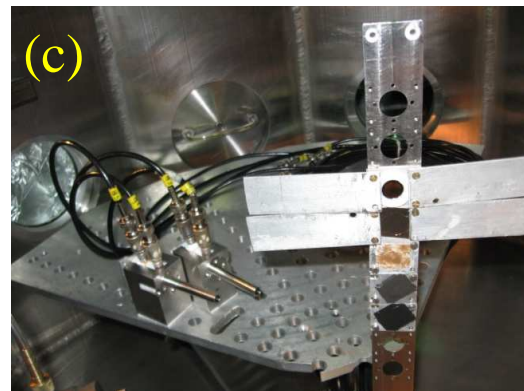
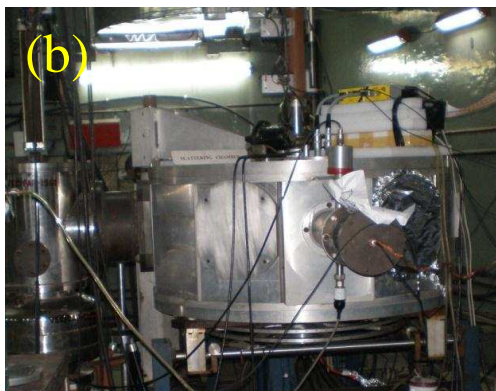
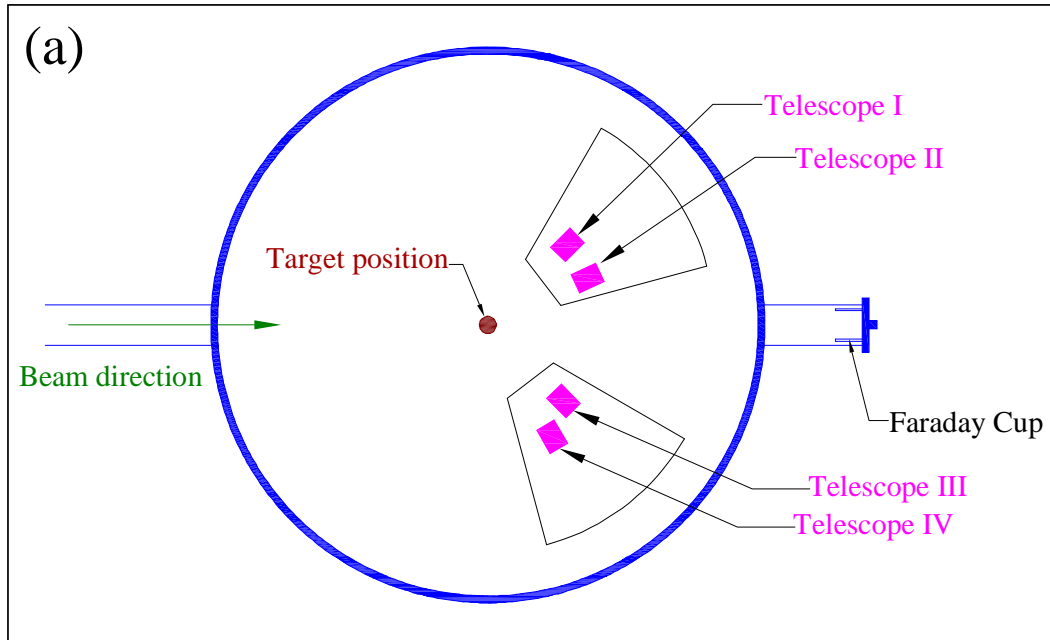


**Figure 2.4:** (a) Schematic diagram of experimental setup used in both experiments done at VECC and pelletron. (b) General purpose scattering chamber, Ch # 2, VECC. (c) Partial view of experimental setup at scattering chamber, Pelletron.

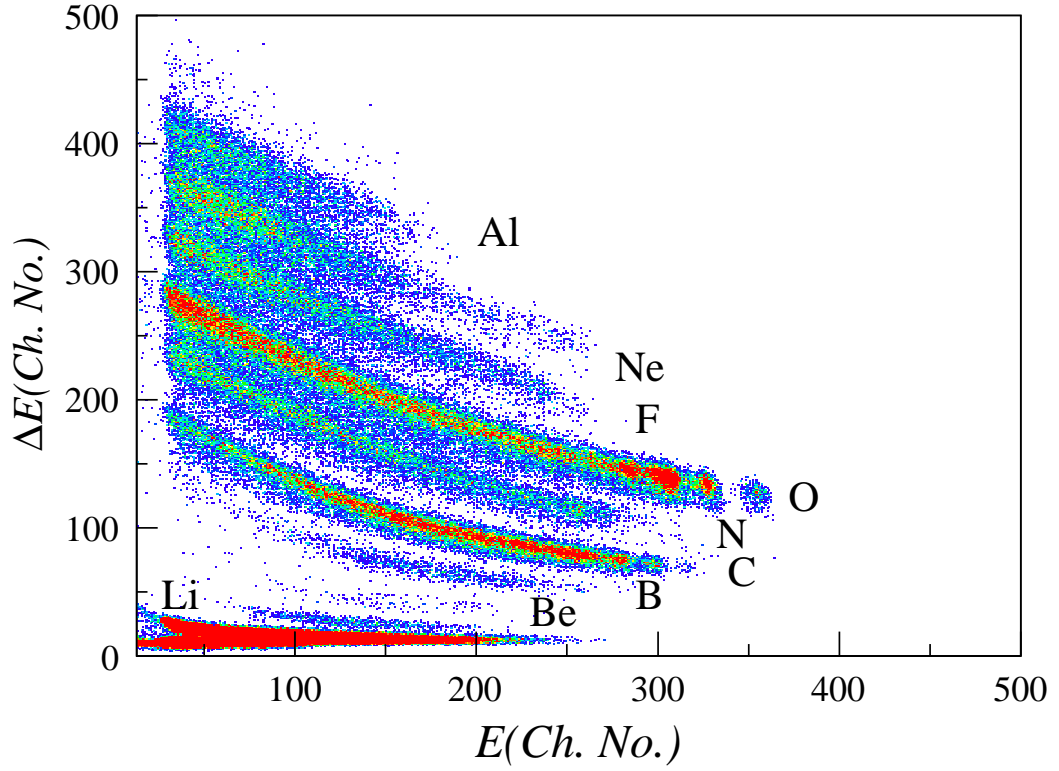


**Figure 2.5:**  $\Delta E$ - $E$  heavy ion spectrum obtained in  $117 \text{ MeV } ^{16}\text{O} + ^{12}\text{C}$  reaction at  $\theta_{lab} = 12^\circ$ .

Eq. 2.4 becomes

$$\Delta E \cdot E = f(A, z) \quad (2.5)$$

which is the equation of a rectangular hyperbola. So, each fragment will give a separate hyperbola in the same  $\Delta E$ - $E$  plot. A typical  $\Delta E$ - $E$  2D spectrum of the fragments emitted in the reaction  $^{16}\text{O} + ^{12}\text{C}$  obtained by a  $\Delta E$ - $E$  telescope is shown in Fig. 2.5. The technical specifications of the detectors have been chosen according to the experimental plan. For example, for the detection of heavy ions, thickness of  $\Delta E$  detector will be thin enough, so that, ions should not be fully stopped at  $\Delta E$ . On the other hand, for the detection of light charged particle, thickness of the  $\Delta E$  detector should be thick enough to generate appreciable signal and at the same time the  $E$  detector should be sufficiently thick to fully stop them. Details of the telescopes used in the present experiments are given in Table 2.2.

**Table 2.2:** *Technical details of the telescopes.*

Properties of the telescopes	Experiment at VECC	Experiment at Pelletron
Number of telescope used	:Four	:Three
Thickness	:Telescope I: $6\mu\text{m}$ [Si(SB)]-4cm [CsI(Tl)] :Telescope II: $9\mu\text{m}$ [Si(SB)]-500 $\mu\text{m}$ [Si(Li)] :Telescope III: $14\mu\text{m}$ [Si(SB)]- 350 $\mu\text{m}$ [Si(SB)] :Telescope IV: $10\mu\text{m}$ (Si)-500 $\mu\text{m}$ [Si(Li)]	:Telescope I : $10\mu\text{m}$ [Si(SB)]-500 $\mu\text{m}$ [Si(SB)] :Telescope II: $10\mu\text{m}$ [Si(SB)]-500 $\mu\text{m}$ [Si(SB)] :Telescope III: 4 cm [Ionization Chamber, 80 Torr]- 350 $\mu\text{m}$ [Si(SB)] : * * *
Energy resolution	:~ 1% for 5.5 MeV $\alpha$ - particle[Si-detector].	:~ 1% for 5.5 MeV $\alpha$ - particle [Si-detector].
Solid angle coverage	: ~ 0.3msr	: ~ 0.23msr
Approximate energy threshold (for different fragments.)	: 2.8, 4.5, 6.5, 9.0 MeV for $\alpha$ -particle, $^7\text{Li}$ , $^9\text{Be}$ , and $^{11}\text{B}$ , respectively.	: 2.8, 4.5, 6.5, 9.0 MeV for $\alpha$ -particle, $^7\text{Li}$ , $^9\text{Be}$ , and $^{11}\text{B}$ , respectively.

### 2.2.3 Electronics and data collection

Standard readout electronics have been used in both the experiments for processing and acquisition of the detector signals. Schematic diagram of the electronic circuit used in the experiment performed at VECC is shown in Fig. 2.6. In this experiment, four telescopes have been used. The detector signals from all telescopes have been fed to ORTEC preamplifiers (Model 142IH). The energy outputs of all preamplifiers have been fed to the input of ORTEC 572A spectroscopic amplifier. By inspecting the measured 2D energy spectra of the fragments during the experiment, the gains of the amplifiers have been adjusted in such a way that all bands (each hyperbola) of the detected fragments are clearly separated. Outputs of the amplifiers have been directly fed to the energy inputs of the analog to digital converter (ADC) ORTEC AD811. The time outputs of the preamplifiers ( $E$  detectors only) have been fed to timing filter amplifier (ORTEC Quad TFA 863) and its output has been fed to constant fraction discriminator (ORTEC Octal CFD CF8000). The logic outputs of CFDs have been fed to gate and delay generator (ORTEC Octal GG8020) and then the OR (PHILIPS SCIENTIFIC Quad four fold logic unit PS 756) of all timing outputs (GG output) have been used as the STROBE of ADC. Lastly, the digitized data from ADC have been collected by PC based CAMAC data acquisition system as shown in Fig. 2.6. For the experiment done at pelletron, similar electronics and data acquisition system have been used.

### 2.2.4 Measurements

As mentioned earlier, two experiments have been performed; one using the cyclotron accelerator at Kolkata and other using the Pelletron accelerator at Mumbai. The details of the beams, targets and measurements are given in Table 2.3 for both the experiments.

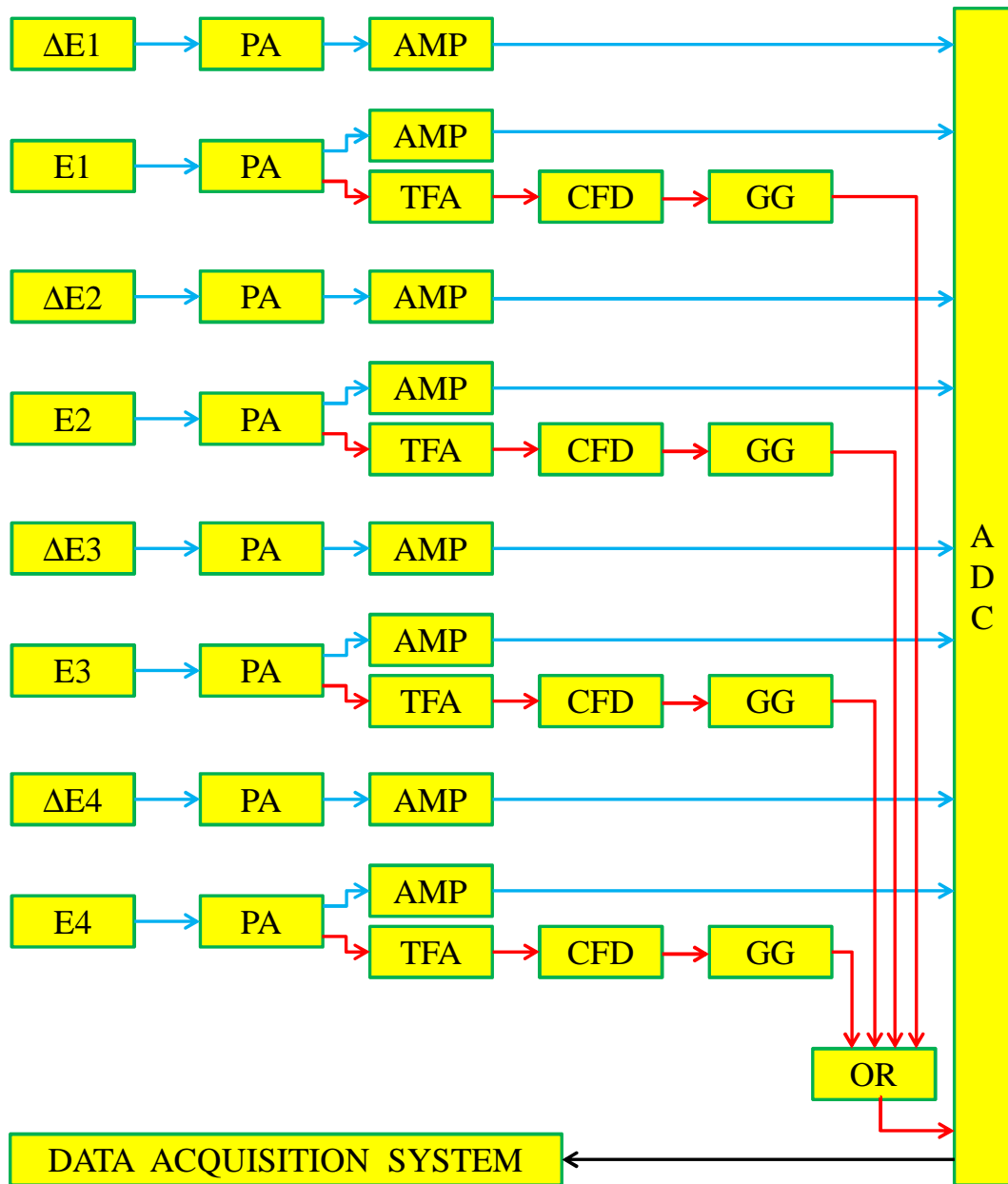


**Figure 2.6:** Schematic diagram of electronics circuit used in the experiment at VECC. PA: Preamplifier, AMP: Amplifier, TFA: Timing filter amplifier, CFD: Constant fraction discriminator, GG: Gate and delay generator, OR: Fan-in-Fan-out.

**Table 2.3:** *Experimental details.*

Details	Experiment at VECC	Experiment at Pelletron
Beam	:Oxygen	:Carbon and boron
Beam energy	:117, 125, 145 and 160 MeV	:73, 77 MeV carbon and 64 MeV boron
Typical beam current	:~10-20nA	:~10-35nA
Typical beam energy resolution	:~0.5 %	:~2keV
Target	:Self-supporting carbon of thickness ~514 $\mu\text{g}/\text{cm}^2$ :	:Self-supporting aluminum of thickness ~500 $\mu\text{g}/\text{cm}^2$ :Silicon of thickness ~1000 $\mu\text{g}/\text{cm}^2$
Measurements	:Energy and angular distributions of $\alpha$ , Li, Be, B	:Energy and angular distributions of Li, Be, B
Angular coverage (lab) with respect to beam direction	:~ 9 <sup>0</sup> -29 <sup>0</sup>	:~ 12 <sup>0</sup> -55 <sup>0</sup>
Energy calibration of the telescopes	:Peaks of elastically scattered oxygen from Au target at all beam energies and $\alpha$ from <sup>229</sup> Th	:Peaks of all the elastically scattered beams of different energies from Al and Au targets.
Gain matching of $\Delta E$ and E detec- tors.	:Using pulsar	:Using pulsar
Target thickness measurement	: <sup>229</sup> Th $\alpha$ -source	:Using <sup>239</sup> Pu- <sup>241</sup> Am $\alpha$ -source

## 2.3 Data analysis technique

Several steps are involved to convert the raw data obtained in the experiment to the final form, which may be utilized to extract physics results. Various steps of the data analysis procedure have been elaborated below.

### 2.3.1 Target thickness measurement

To measure the target thickness, an  $\alpha$ -source having more than one known well separated energy peaks has been used in a separate experimental set up with only one detector with similar electronics circuit and DAQ as used in the main experiment. First, the energy spectrum of  $\alpha$ -source has been measured after placing the target foil in between the detector and the source; in the next step, the same measurement has been repeated without the target. Due to the loss of energy in the target, when the target is in, whole energy spectrum will be shifted towards lower channel number (lower energy) of ADC with respect to the spectrum without the target. Now from the known energy peaks of the  $\alpha$ -particles, channel number can be calibrated and energy loss in the target can be calculated. The stopping power ( $dE/dx$ ) of  $\alpha$ -particle in the target material at the respective peak energies can be obtained from SRIM [90] calculation. By dividing the total energy loss in the target by stopping power, the actual target thickness can be obtained. In the present experiment,  $^{229}\text{Th}$   $\alpha$ -source with peak energies at 5.423, 5.680, 6.290, 6.780, 8.78 MeV have been used to measure the thickness of targets used in the experiment done at VECC. For the experiment at Pelletron,  $^{241}\text{Am}$ - $^{239}\text{Pu}$   $\alpha$  source peaks at 5.485 MeV and 5.152 MeV, has been used for the measurement of the target thickness. Measured thickness of the targets are given in Table 2.3.

### 2.3.2 Gain matching factor

Total energy of any fragment is obtained by adding the energies deposited in the  $\Delta E$  and  $E$  detectors, provided the overall gains of both the detectors are brought in the same scale. For this purpose, the ratio of the gains of  $E$  and  $\Delta E$  detectors is multiplied to the channel number of  $\Delta E$ . This ratio is called the gain matching factor ( $gmf$ ). To

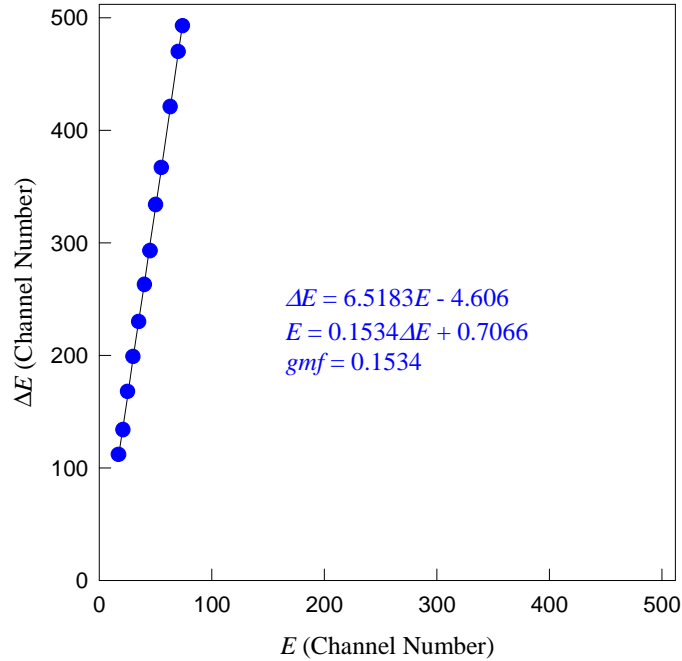


**Figure 2.7:** Typical gain matching spectra of telescope IV, used in the experiment performed at VECC.

find out the factor, the same signal from a pulsar has been fed into both the test inputs of the preamplifiers of  $\Delta E$  and  $E$  detectors (of a particular telescope) and the pulse height has been increased gradually; the corresponding 2D spectrum is shown in Fig. 2.7, which may be fitted with the a straight line,  $\Delta E = m_g E + c_g$ , where  $m_g$  is the slope and  $c_g$  is constant. Then, according to the definition above,  $gmf \approx 1/m_g$ , when  $c_g/m_g$  is small. In the typical case of telescope IV, used in the experiment done at VECC (Fig. 2.7),  $E = 0.1534\Delta E + 0.7066$ . Using these values, energy deposited (*Ch. No.*) in  $\Delta E$  detector is converted into equivalent energy (*Ch. No.*) of  $E$  detector, and the total

energy (*Ch. No.*) may be calculated as  $E_{total} = E + gmf\Delta E$ , which is finally converted into actual energy by using calibration equation for the corresponding telescope.

### 2.3.3 Energy loss correction of the projectile and fragments

Due to finite thickness, the target has different layers of atoms along the path of the projectile and the ejectiles. So, nuclear reaction may occur at any layer of the target as shown the Fig. 2.8. Depending upon the position of the interaction point (distance

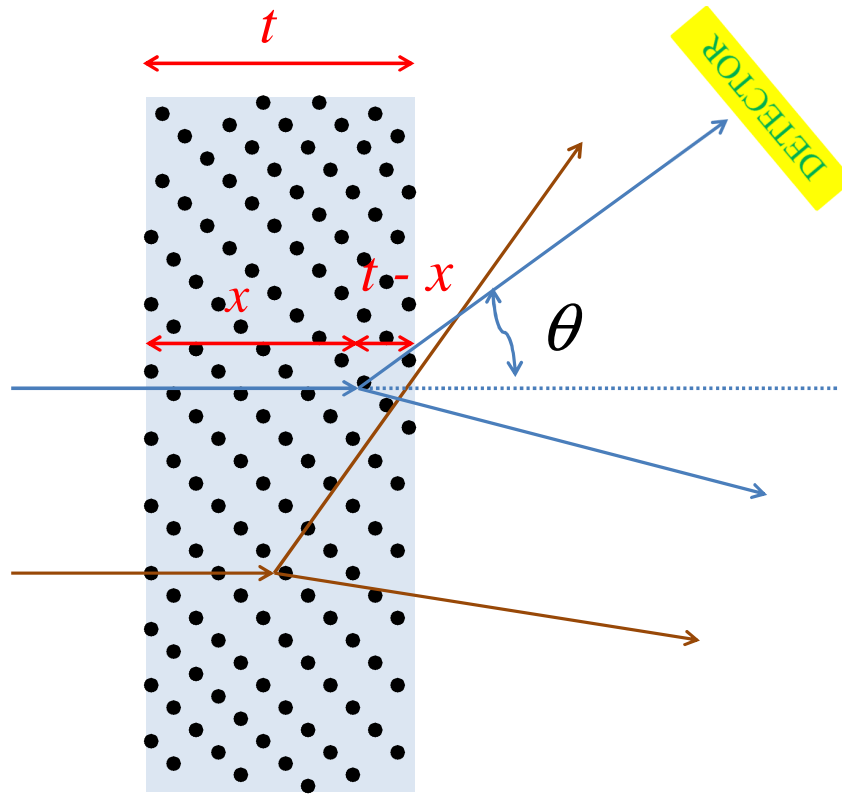


**Figure 2.8:** Energy loss of projectile and ejectile in the target.

$x$  from the entry point), projectile loses a part of its energy in the target and the actual beam energy at the point of interaction becomes  $E_{beam} - (\frac{dE}{dx})_{E_{beam}} \times x$ . The same is true for the ejectiles also. Before detection, the ejectile has to travel a distance of  $(t-x)\sec\theta$  where  $\theta$  is the detection angle and  $t$  is target thickness. So, if the actual ejectile energy, is  $E_{corr}$ , the energy measured by the detector is  $E_{corr} - (\frac{dE}{dx})_{E_{corr}} \times (t-x)\sec\theta$ . Now it

is not possible to measure the actual position of interaction point for each event. So, it is generally assumed that the interaction occur uniformly throughout the target layers and the average effect of the finite thickness may be taken care of by considering that the interaction occurs at the middle of the target,  $t_{1/2} \approx t/2$ . Then, the detected energy

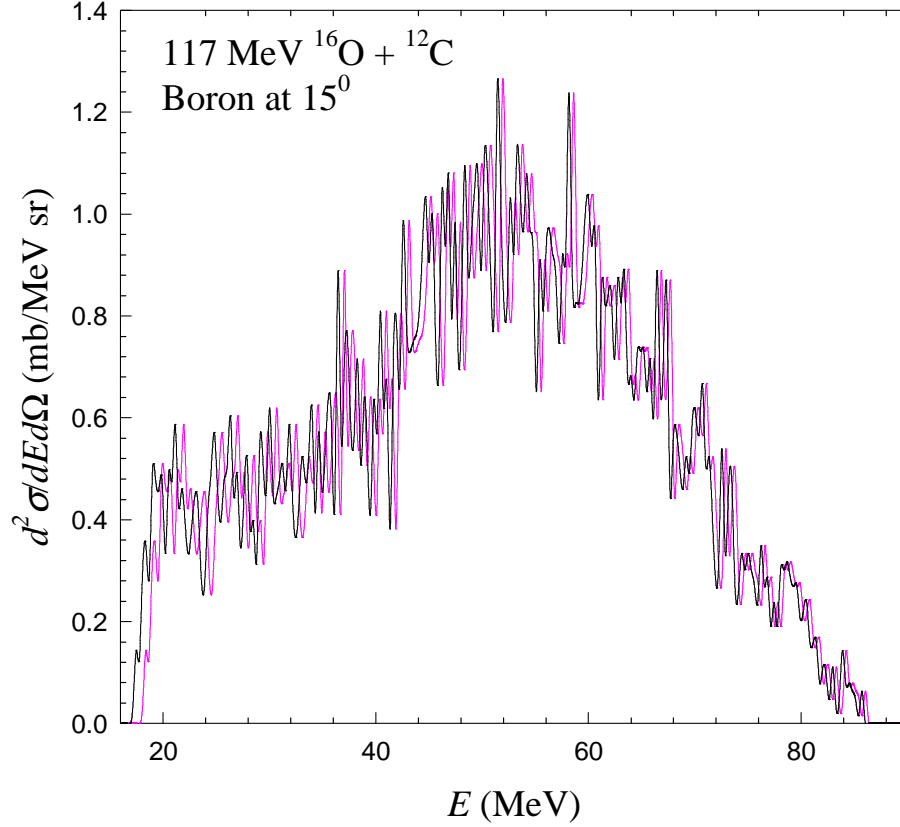


**Figure 2.9:** The effect of energy loss correction on fragments in the target. Black line is the detected spectrum and pink line is the corresponding spectrum after energy loss correction.

of the fragment is  $E_{det}$ , is related to  $E_{corr}$  by,

$$E_{corr} = E_{det} + \left( \frac{dE}{dx} \right)_{E_{corr}} \times t_{1/2} \sec\theta \quad (2.6)$$

Similarly, the actual projectile energy before reaction will be

$$E_{reaction} = E_{beam} - \left( \frac{dE}{dx} \right)_{E_{beam}} \times t_{1/2} \quad (2.7)$$

In the case of projectile energy correction, beam energy is exactly known. So, we can easily calculate  $E_{reaction}$  by taking the value of stopping power  $\left( \frac{dE}{dx} \right)_{E_{beam}}$  at beam energy,  $E_{beam}$ , from SRIM [90]. However, in the case of fragment energy spectrum, for

each value of energy, stopping power is different [89]. Moreover the stopping power has to be known at the actual energy of the fragment  $E_{corr}$  and not at the corresponding detected energy  $E_{det}$ . Therefore, the fragment energies were corrected using the following procedure. Firstly, the stopping power has been calculated at all possible fragment energies using SRIM [90] and  $E_{det}$  has been calculated for each values of  $E_{corr}$  using Eq. 2.6. Then the values of  $E_{corr}$  and the corresponding  $E_{det}$  have been fitted with a generalized function as given below,

$$E_{corr} = C_1 + C_2 E_{det} + C_3 / E_{det} + C_4 / E_{det}^2 \quad (2.8)$$

where  $C_1$ ,  $C_2$ ,  $C_3$  and  $C_4$  are the constant parameters. The typical values of these parameters for boron fragment (in experiment at VECC) are 0.02946, 0.9986, 14.3628, -58.1835, respectively. The effect of the energy loss correction in a typical boron spectrum is shown in Fig. 2.9.

### 2.3.4 Energy calibration of the telescopes

Generally, the energy calibration is done for the telescope as a whole, in the following manner. The elastic peak for a particular reaction is obtained experimentally in terms ADC channel number at different laboratory angles. Total energy ( $Ch. No.$ ) of the elastic peak is calculated using the relation,  $E_{tot} = gm f \times \Delta E + E$ . The corresponding elastic peak energy in MeV is calculated from kinematics with energy corrected for loss (using Eq. 2.7 ) in the target. With this, the energy of scattered particle for a particular angle  $\theta$  is calculated and is modified by using Eq. 2.6. This energy corresponds to the detected elastic peak energy in terms of channel number. A known energy  $\alpha$ -source (e.g.,  $^{228}\text{Th}$ ) is used for calibration points at lower energy. All these channel numbers and corresponding energies are fitted with the calibration equation given by

$$E = Ch \times m + c \quad (2.9)$$

where  $E$  is the energy in MeV,  $m$  is the energy per channel (MeV/ $Ch$ ) and  $c$  is a constant (MeV). Typical energy calibration has been shown in Fig. 2.10 for telescope IV. Blue

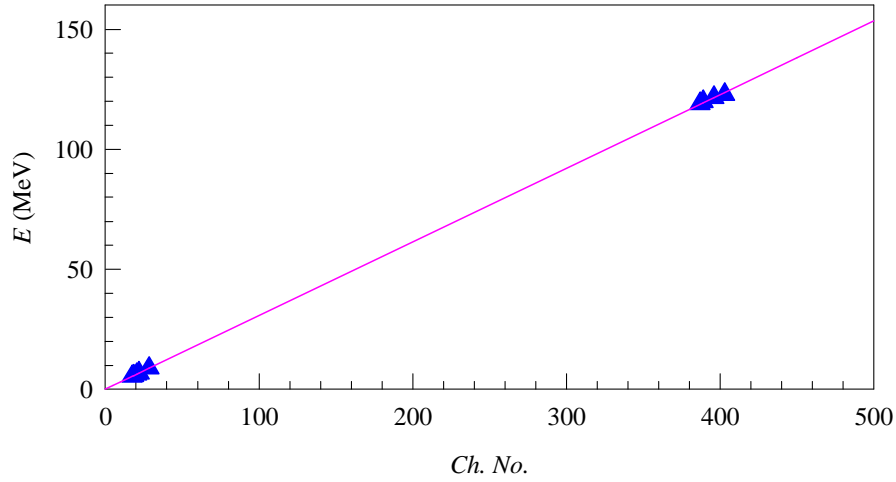


**Figure 2.10:** Calibration of telescope IV used in the experiment at VECC.

triangles represent the experimental points with known the energies obtained from elastic pecks in 125 MeV  $^{16}\text{O}$  on gold reaction and  $\alpha$ -particles peaks from  $^{228}\text{Th}$  source. For this telescope,  $m = 0.31 \text{ MeV/Ch}$  and  $c = 0.03\text{MeV}$ .

### 2.3.5 Calculation of cross section

The fragments are identified from the well separated bands in the  $\Delta E$ - $E$  2D spectrum as shown in Fig. 2.5. To extract the energy spectrum from the 2D plot, a two dimensional gate is drawn around the band of the desired fragment. The yield inside this gate is projected along  $E_{tot} (= gmf \times \Delta E + E, \text{ Ch. No.})$  and energy is then converted to MeV using the calibration equation. To convert the yield in terms of standard unit of cross section, it is normalized by number of incident particles ( $I$ ) on target, the number density of target atom per unit area ( $N$ ), the solid angle covered by the telescope ( $\Omega$ ) and, the energy per channel ( $m$ ) using the following expression of differential cross section,

$$\frac{d^2\sigma}{dEd\Omega} = \frac{C}{NI\Omega m} \times 10^{-27} \text{mb/MeVsr} \quad (2.10)$$

$C \rightarrow$  Experimental yield of the fragment in each channel of projected spectrum.

$N \rightarrow$  Number of target atoms per  $\text{cm}^2$  which is calculated using formula  $N = \frac{N_A}{A}t$  where  $N_A$  is Avogadro number  $6.023 \times 10^{23}$  atoms/mol,  $A$  is atomic mass number,  $t$  is the thickness of the target in  $\text{gm}/\text{cm}^2$ .

$I \rightarrow$  Number of incident particles is measured from the total charge collected in Faraday cup in beam dump using a current integrator.

$\Omega \rightarrow$  Solid angle coverage of the telescopes are measured geometrically and checked by comparing experimental yield,  $\left(\frac{d\sigma}{d\Omega}\right)_{\text{expt,lab}}$ , of elastic scattering spectra and Rutherford scattering cross section,  $\left(\frac{d\sigma}{d\Omega}\right)_{\text{Ruth,lab}}$ .

To interpret the experimental data theoretically, it is required to transform the measured cross section from laboratory frame to c.m. frame which is done by the following equation

$$\left(\frac{d\sigma}{d\Omega}\right)_{\text{c.m.}} = \left(\frac{d\sigma}{d\Omega}\right)_{\text{lab}} \frac{|1 + \gamma \cos\theta_{\text{c.m.}}|}{(1 + \gamma^2 + \gamma \cos\theta_{\text{c.m.}})^{3/2}} \quad (2.11)$$

where  $\gamma = \left(\frac{A_1 A_3}{A_2 A_4} \frac{E_{\text{cm}}}{E_{\text{cm}} + Q}\right)^{1/2}$ ,  $Q$  is the Q-value of the reaction,  $A_1$ ,  $A_2$ ,  $A_3$  and  $A_4$  are projectile, target, detected fragment and recoil fragment mass number, respectively.  $E_{\text{c.m.}}$  is the beam energy available for reaction in c.m. which is obtained by

$$E_{\text{c.m.}} = \frac{A_2}{A_1 + A_2} E_{\text{lab}} \quad (2.12)$$

and  $\theta_{\text{c.m.}}$ , scattering angle in c.m., is obtained by

$$\theta_{\text{c.m.}} = \theta_{\text{lab}} + \sin^{-1}(\gamma \sin\theta_{\text{lab}}) \quad (2.13)$$

## Chapter 3

# Result: Fragment and light particle emission in $^{16}\text{O} + ^{12}\text{C}$ reactions

In this chapter, the results of the fragment and light charged particle emission measurement for the reactions  $^{16}\text{O}$  (117, 125, 145 and 160 MeV) +  $^{12}\text{C}$  will be presented. The main aim of these measurement were to look for the signature/indications of orbiting at higher excitation in the  $\alpha$ -cluster system  $^{16}\text{O} + ^{12}\text{C}$ , which is known to be orbiting at low excitation [72]. Both fragment emission and light charged particle ( $\alpha$ -particle) emission have been used as probes to study the reaction mechanism. As orbiting dinucleus is likely to be highly deformed (as shape relaxation has not occur), the estimation of deformation is crucial to decipher the roles played by orbiting in this system and the shape of energy spectra of LCP (particularly  $\alpha$ -particle) being quite sensitive to the deformation, becomes an important tool. This chapter will be divided into two broad section, first the result of the fragment emission study will be presented in Sec. 3.1 and result of LCP study will be discussed in Sec. 3.2.

## 3.1 Fragment emission study

### 3.1.1 Energy spectra

Typical energy spectra of the fragments Li, Be, B measured at angle  $\theta_{lab} = 15^\circ$  for  $E_{lab}=117, 125, 145$  and  $160$  MeV are shown in Fig. 3.1. The shapes of the spectra are nearly Gaussian almost in all cases. The Gaussian-like shape of the fragment energy spectra may be understood as follows; the equilibrated compound nucleus undergoes deformation leading to fission-like decay into two fragments. Then, the fragment kinetic energy distribution is likely to be Gaussian-like with the average energy corresponding to the kinetic energy at the scission point and the width originating from the fluctuation of the scission point. It has been observed that in case of boron, the lower energy part of the spectrum is found to deviate from the Gaussian behavior and the deviation increases with increasing bombarding energy. Similar observation, to a lesser extent, can also be made regarding beryllium spectrum. From the study of the energy spectrum, it has also been found that the peak position of each spectrum is nearly same as that obtained from Viola systematic [91] corrected by an asymmetry factor given by

$$\frac{4Z_1Z_2}{(Z_1 + Z_2)^2} \quad (3.1)$$

[44] where  $Z_1$  and  $Z_2$  are the atomic number of the two emitted fragments. Viola systematic, which basically gives the dependence of most the probable total kinetic energy of symmetric fission fragments on the Coulomb parameter  $Z^2/A^{1/3}$  of the fissioning nucleus, is given by

$$\langle E_{KE} \rangle = 0.1189Z^2/A^{1/3} + 7.3 \text{ MeV} \quad (3.2)$$

Each of the energy spectrum has been fitted with a Gaussian as shown in Fig. 3.1 by solid line with the corresponding centroid shown by arrows. In case of boron fragment, though the spectra are deviated from the Gaussian shapes, particularly at the lower energy region, still they can be fitted with a Gaussian by taking the centroids obtained from Voila systematic and the widths obtained from the higher energy tail of of the spectra (higher energy side of the centroid).

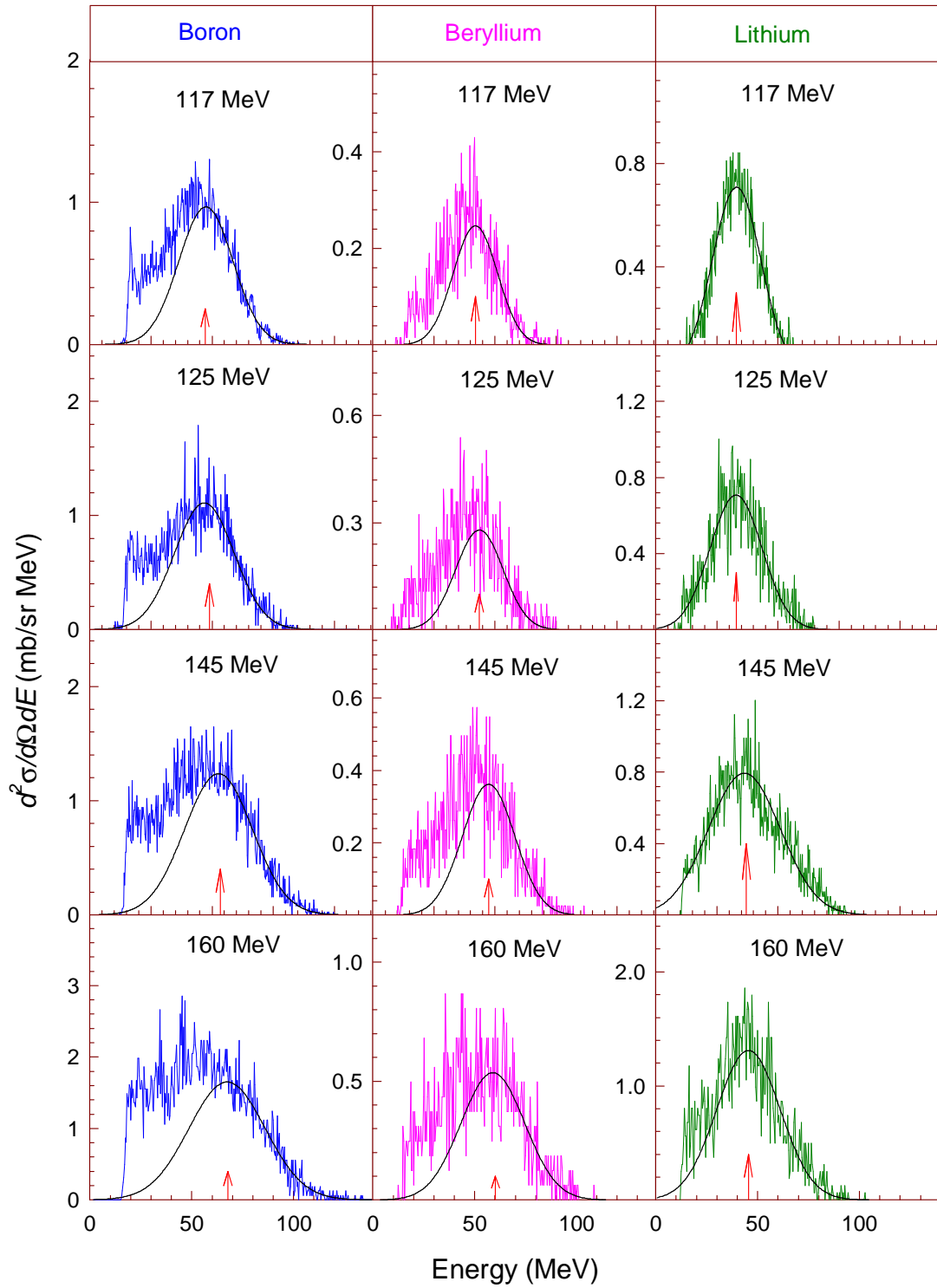


**Figure 3.1:** Typical energy spectra of emitted fragments (B, Be and Li) detected at an angle  $\theta_{lab} = 15^\circ$  at respective  $E_{lab}$ . Arrows indicate the centroid of the Gaussian distributions.

### 3.1.2 Angular distribution

The angular distributions of the fragments emitted from an equilibrated composite follow  $1/\sin\theta_{c.m.}$  dependence in c.m. frame. This  $1/\sin\theta_{c.m.}$  dependence can be intuitively explained [92, 93] as follows: to conserve the orbital angular momentum of the

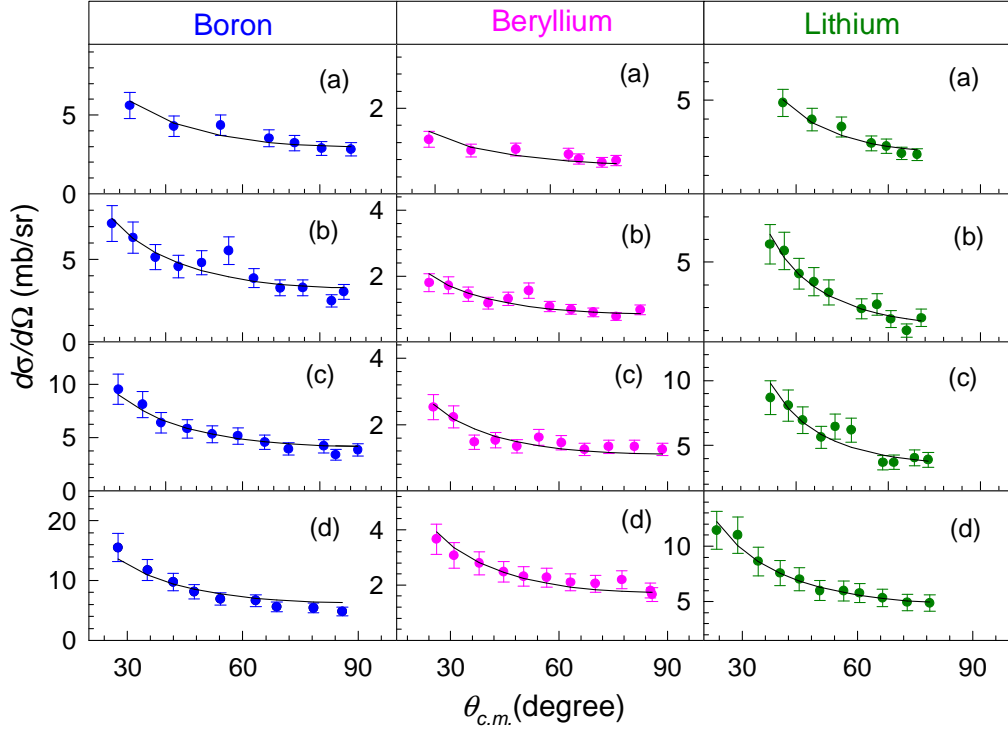


**Figure 3.2:** The c.m. angular distributions of the B, Be and Li fragments obtained at  $E_{lab} = 117, 125, 145,$  and  $160$  MeV [from (a) to (d), respectively]. Solid circles correspond to experimental data and solid lines show fit to the data obtained using the function  $f(\theta_{c.m.}) \propto 1/\sin\theta_{c.m.}$ .

incident particles, the composite system will rotate about an axis perpendicular to the beam direction. If the composite is considered as rotating liquid drop, the particles evaporated from the composite will get an additional velocity if they are emitted at the equator, and the angular distribution has therefore a maximum in the equatorial plane. In a situation, if all the composites have angular momentum perpendicular to both reaction plane and beam direction, all the equatorial planes should coincide with the reaction plane and angular distribution would be independent of  $\theta_{c.m.}$ . However, in

the case of energetic nuclear collision, the direction of angular momentum is random and it always lies in the plane perpendicular to the beam axis. If one averages over the different possible directions of the rotational axis, there will be maxima in the forward and backward directions of the beam, as these directions are contained in all equatorial plans. The distribution will furthermore be symmetrical about  $90^\circ$ . Angular distributions (in c.m. frame) for Li, Be, B are shown in Fig. 3.2 for all beam energies. The differential cross section,  $\left(\frac{d\sigma}{d\Omega}\right)_{lab}$ , has been obtained by integrating the energy spectra under the fitted Gaussian only. The obtained  $\left(\frac{d\sigma}{d\Omega}\right)_{lab}$  has then been transformed into c.m. frame  $\left(\frac{d\sigma}{d\Omega}\right)_{c.m.}$  by using Eq. 2.11, assuming two-body kinematics averaged over total kinetic energy distribution and the corresponding lab angle  $\theta_{lab}$  has been transformed by using Eq. 2.13. In both cases, the  $Q$ -value has been calculated using the following formula,

$$Q = T_3 \left(1 + \frac{M_3}{M_4}\right) - T_1 \left(1 - \frac{M_1}{M_4}\right) - 2 \left(\frac{M_1 M_3 T_1 T_3}{M_4^2}\right)^{1/2} \cos\theta_{lab} \quad (3.3)$$

where  $T_1, T_2, T_3, T_4$  (and  $M_1, M_2, M_3, M_4$ ) are the kinetic energies (and mass numbers) of the projectile, target, detected fragment, and recoil fragment, respectively. The angular distribution of the fragments B, Be, and Li obtained at all bombarding energies are found to follow  $1/\sin\theta_{c.m.}$  dependence in c.m. frame (shown by solid lines in Fig. 3.2), which is characteristic of the fission like decay of an equilibrated composite system.

### 3.1.3 Angular distribution of average $Q$ -value

The angular distribution of the average  $Q$ -value,  $\langle Q \rangle$ , provides information about the degree of equilibration of the composite. For example, in the reactions  $^{16}\text{O}(116 \text{ MeV}) + ^{27}\text{Al}$ ,  $^{28}\text{Si}$  [94, 21] and  $^{20}\text{Ne}(145, 158, 200, 218 \text{ MeV}) + ^{28}\text{Al}$  [95],  $\langle Q \rangle$  has been shown to fall very sharply with  $\theta_{c.m.}$  at forward angles, which indicated about non-equilibrated nature of the decay of the produced composites at all these energies. However, in the present study of fragment emission, it has been observed that the

values of  $\langle Q \rangle$  for all the fragments obtained at different bombarding energies, are independent of center of mass emission angles as shown in Fig. 3.3. The independence of  $\langle Q \rangle$  with respect to emission angle suggests that, the fragments are emitted from a completely energy equilibrated system at all beam energies. Similar results have also been observed in the case of fragments emitted in  $^{20}\text{Ne} + ^{12}\text{C}$  system [96].

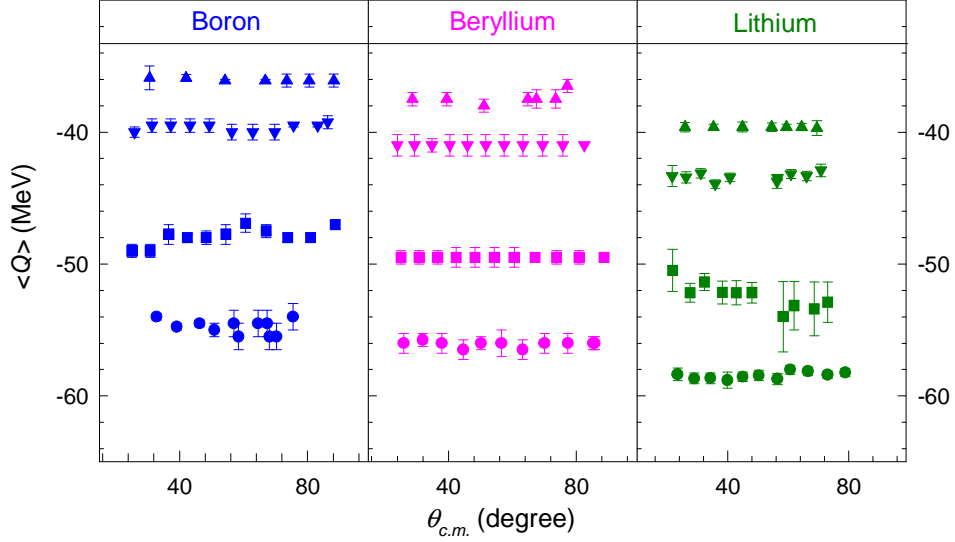


**Figure 3.3:** Average  $Q$ -values,  $\langle Q \rangle$ , of the fragments B, Be and Li obtained at  $E_{lab} = 117, 125, 145$  and  $160$  MeV (denoted by triangle up, triangle down, square and circle, respectively) plotted as a function of c.m. emission angle,  $\theta_{c.m.}$ .

### 3.1.4 Excitation energy dependence of $\langle Q \rangle$ averaged over angle

The average  $Q$ -values,  $\langle Q \rangle$ , have been averaged over the angle [denoted by  $\langle \bar{Q} \rangle$ ] again and plotted in Fig. 3.4 for all the beam energies. It has been found that the  $\langle \bar{Q} \rangle$  values varies linearly with  $E_{c.m.}$  ( $E_{c.m.}$  is the beam energy in c.m. available for reaction). This linear dependence is indicative of full energy equilibration of the composites. The linear relationships extracted from the data (Fig. 3.4) are  $\langle \bar{Q} \rangle = (13.91 \pm 0.91) - (1.004 \pm 0.016)E_{c.m.}$  for the fragment B,  $\langle \bar{Q} \rangle = (12.58 \pm 0.32) - (1.005 \pm 0.005)E_{c.m.}$  for Be and  $\langle \bar{Q} \rangle = (11.03 \pm 1.18) - (1.021 \pm 0.020)E_{c.m.}$  for Li. Moreover, the above linear dependencies also mean that the final kinetic energies ( $E_{kin}^f = \langle Q \rangle +$

$E_{c.m.}$ ) of the fragments are nearly independent of the incident energy. Similar linear dependence of  $\langle \bar{Q} \rangle$  has been observed in the fragment emission from  $^{20}\text{Ne} + ^{12}\text{C}$  system in the bombarding energy range 50 - 200 MeV [96, 95, 97]. This may be due to the limitation on the maximum value of angular momentum beyond which the formation of a dinucleus is not allowed because of centrifugal repulsion [84].

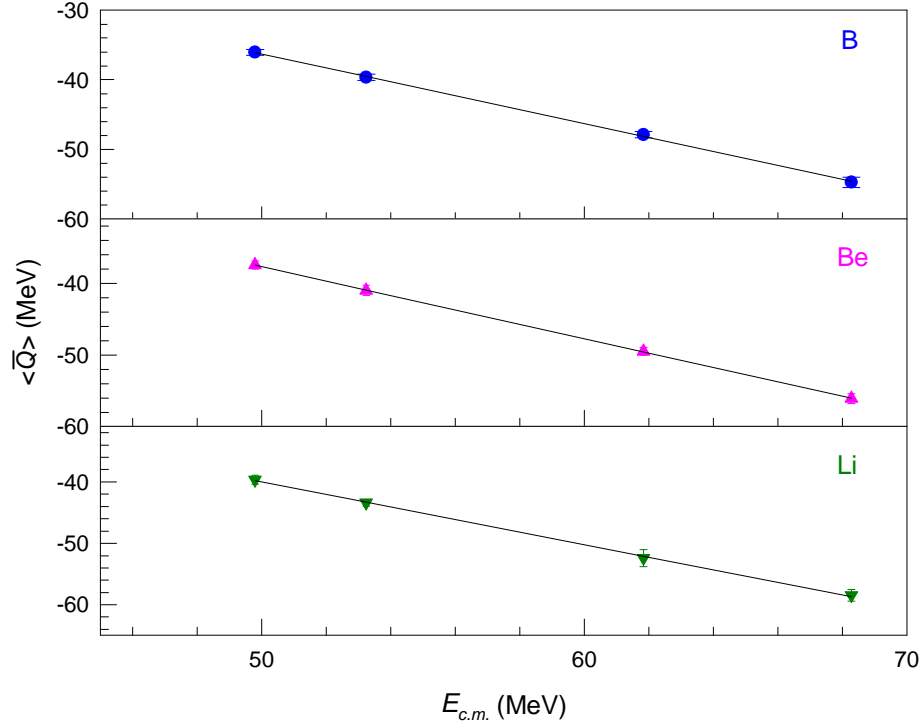


**Figure 3.4:** Variation of  $\langle \bar{Q} \rangle$  with  $E_{c.m.}$ . The solid lines show the linear dependence of  $\langle \bar{Q} \rangle$  with bombarding energy for the fragments B, Be and, Li respectively.

### 3.1.5 Total cross section of the fragment

All these observations show that the fragments have been emitted either from a fully equilibrated CN, or, from a long-lived orbiting dinuclear system, or, from both. It may be noted here that, in case of dinuclear orbiting, the composite system is fully energy equilibrated but shape is not equilibrated. To get further information about the emission process, the angle integrated fragment yields obtained from the fitted Gaus-

sians, have been compared with the theoretical predictions of the standard statistical model codes, i.e., CASCADE [7] and extended Hauser-Feshbach model (EHFM) [18]. The extracted angle integrated yields of different fragments obtained at different incident energies have been shown in Fig. 3.5 by solid circles. The solid lines are the same obtained from CASCADE with angular momentum up to  $\ell_{cr}$ , the critical angular momentum of fusion. The values of  $\ell_{cr} = 20, 21, 22$  and  $23 \hbar$  for beam energy 117, 125, 145 and 160 MeV, respectively. These  $\ell_{cr}$  values have been obtained from dynamical trajectory model calculations with realistic nucleus-nucleus interaction and dissipative forces generated self-consistently through stochastic nucleon exchange model [98]. It

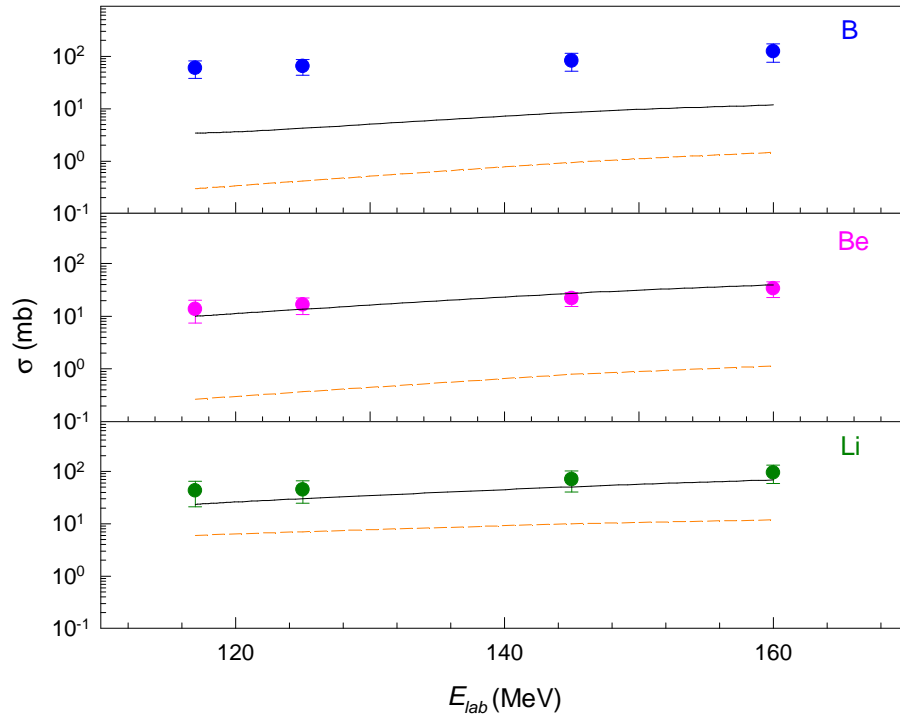


**Figure 3.5:** Excitation functions for the angle-integrated (over the range  $0^0 \leq \theta_{c.m} \leq 180^0$ ) cross section of the B, Be and Li fragments. Solid lines are the predictions of the statistical model CASCADE with angular momentum  $\ell = \ell_{cr}$ . Short dashed lines are the prediction of EHFM.

has been observed that the CASCADE prediction matches well with the experimental yields of the fragments Li, Be. But it underpredicts the B yield at all beam energies. In the case of EHFM, the predicted yields are less than the measured yields all fragments

under study, as shown by dashed line in Fig. 3.5. So, it is evident from the above that there is a significant enhancement in the boron yield with respect to the prediction of both the CASCADE and EHF<sub>M</sub>. Though the CASCADE explains the experimental yield of Li and Be, they are also underpredicted by EHF<sub>M</sub>. However, it may be noted here that the discrepancy between EHF<sub>M</sub> prediction and experimental yield, increases progressively from Li to B, which clearly indicates, increasing additional contributions from other reaction mechanism as one moves from Li to B. So, notwithstanding the limitations of the statistical model calculations extended to light nuclear system, it is evident that there is clear signature of an enhancement in the yield of B as compared to its predicted yield. Such enhancement in the experimental binary yield with respect to respective theoretical predictions near entrance channel configuration is indicative of the formation of an orbiting dinuclear complex. As orbiting is usually described in terms of the formation of a long-lived dinuclear molecular complex that acts as a “doorway” state to fusion with a strong memory of the entrance channel, it is expected that the orbiting mechanism will retain a greater memory of the entrance channel than the FF process. Orbiting has first been established in the system  $^{28}\text{Si} + ^{12}\text{C}$  [36] by observing enhancements of large-angle, binary-reaction yields near to the entrance channel (see Chapter 1 for details); similar enhancements of large-angle, binary-reaction yields have also been observed in the present data.

## 3.2 Study of light charged particle emission

### 3.2.1 Energy spectra

The fusion-evaporation is the most dominated reaction process in light systems, in which the equilibrated composite decays by statistical emission of light charged particles (n, p, d, t,  $^3\text{He}$ ,  $\alpha$ ). It is well established that the  $\alpha$ -evaporation spectra, in particular, carries the signature of the angular momentum dependent deformation of the excited rotating compound nucleus [99, 100, 101]. The energy distribution of the

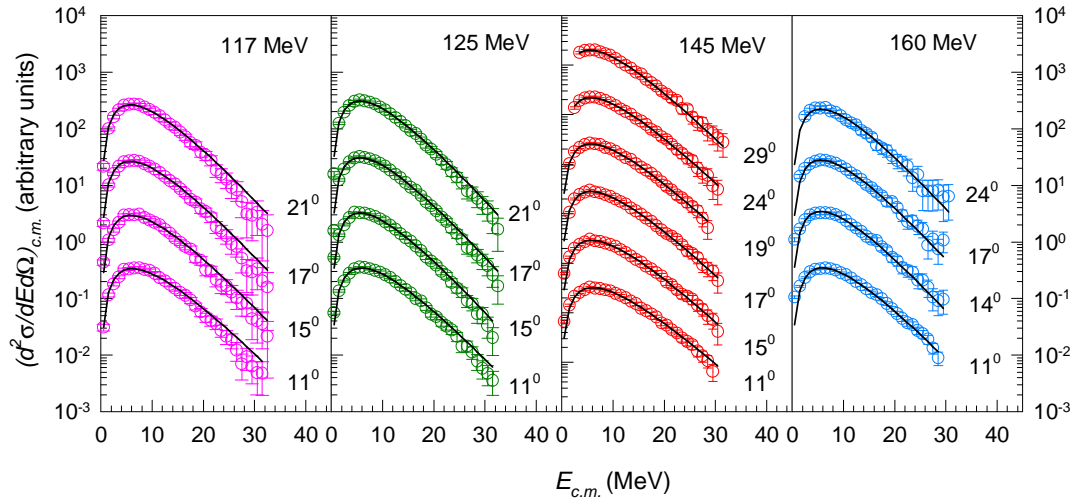


**Figure 3.6:** Energy spectra (c.m.) of  $\alpha$ -particles obtained at different angles for different beam energies. The symbols represent experimental data and the solid lines represent the fitted Maxwellian function. All the experimental and calculated spectra for lower to higher angles have been multiplied by  $10^{-2}$ ,  $10^{-1}$ ,  $10^0$ ,  $10^1$ ,  $10^2$ ,  $10^3$ , respectively.

particles evaporated from a hot system, is known to be Maxwellian in shape [102]. The centre of mass energy spectra of evaporated  $\alpha$ -particles obtained from the reactions  $^{16}\text{O} + ^{12}\text{C}$  at different bombarding energies have been shown (symbols) in Fig. 3.6. In the same figure the solid lines represent the fitted Maxwellian distribution,

$$f(E_{c.m.}) = A E_{c.m.}^{3/2} e^{-E_{c.m.}/T} \quad (3.4)$$

where  $A$  is the normalization constant and  $T$  is the temperature of the hot composite. Since the spectra have been obtained in inclusive mode, there may be some admixture of contributions from other direct reaction mechanisms (like pre-equilibrium emission, etc.) to the equilibrium emission spectra at forward-most angles, in particular. The observed agreement of the experimental energy spectra with the Maxwellian distribution, indicates that  $\alpha$ -particles are emitted mostly from the fusion-evaporation process. For further confirmation, the shape of two spectra, one obtained at most forward angle and the other at backward angle, have been compared and shown in Fig. 3.7. For all beam energies 117, 125, 145 and 160 MeV, the forward most angles at which energy spectra have been measured are  $11^\circ$  and corresponding backward angles are  $21^\circ$ ,  $21^\circ$ ,  $29^\circ$  and

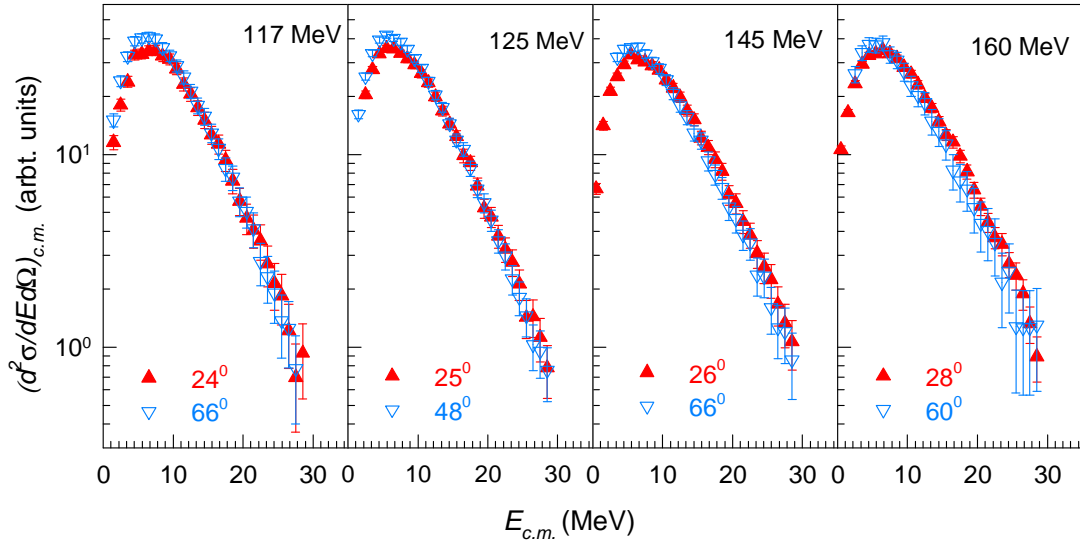


**Figure 3.7:** Comparisons of the energy spectra (*c.m.*) of  $\alpha$ -particles obtained at most forward (red triangles) and backward angles (blue open inverted triangles) at different beam energies. Beam energies and *c.m.* angles are written on the figure.

$24^\circ$ , respectively. It is found that the slopes of both spectra obtained at forward and backward angles are completely matching with each other at all respective beam energies, which clearly indicates that the effects of other direct reaction mechanisms, if any, are not significant even at the forward most measured angles.

### 3.2.2 Angular distribution

The differential cross section,  $(d\sigma/d\Omega)_{c.m.}$ , has been obtained by integrating area under the *c.m.* energy distributions of the  $\alpha$ -particle at each measured angle where conversion of energy distribution in laboratory frame  $(\frac{d^2\sigma}{dE d\Omega})$  to *c.m.* frame  $(\frac{d^2\sigma}{dE d\Omega})_{c.m.}$  was done by multiplying the laboratory spectrum by the ratio of velocity of  $\alpha$ -particle in *c.m.* with its velocity in laboratory. Finally,  $(d\sigma/d\Omega)_{c.m.}$  have been obtained by multiplying with  $2\pi \sin\theta_{c.m.}$ . The angular distributions thus obtained have been shown in Fig. 3.8 as a function of  $\theta_{c.m.}$  for the beam energies of 117, 125, 145 and 160 MeV, respectively. In all cases, the values of  $(d\sigma/d\theta)_{c.m.}$  are found to be constant over the whole

range of observed c.m. angles. So,  $(d\sigma/d\Omega)_{c.m.}$  is  $\propto 1/\sin\theta_{c.m.}$ , which is characteristic of the emission from an equilibrated composite nucleus.

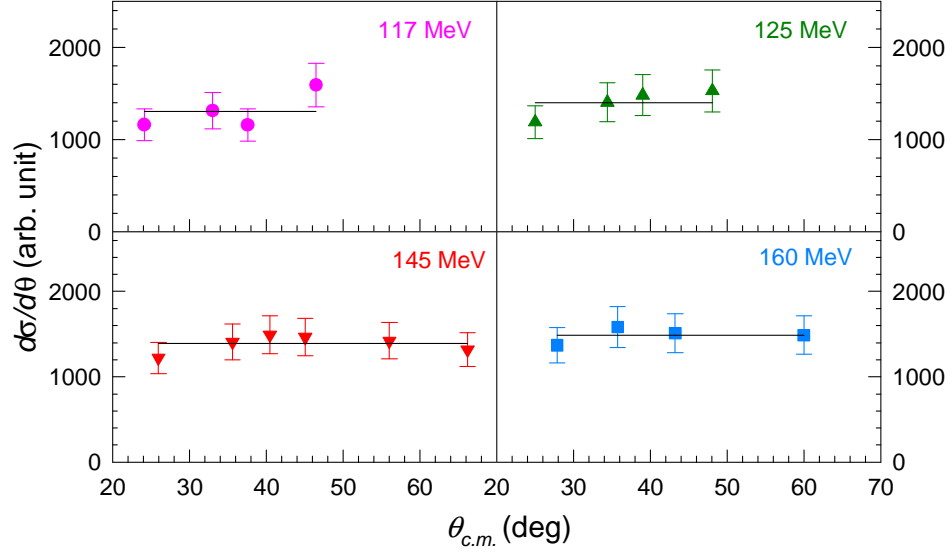


**Figure 3.8:** Angular distribution of  $\alpha$ -particles as a function of c.m. angles,  $\theta_{c.m.}$ . Symbols represents the experimental data and solid lines show fit to the data obtained using  $(d\sigma/d\theta)_{c.m.} = \text{constant}$ .

### 3.2.3 Average velocity

The average velocities in laboratory,  $v_{av}$ , of the  $\alpha$  particles emitted at different angles at different beam energies have been extracted from average energy,  $E_{av}$ . The  $E_{av}$  is obtained by expressions given below

$$E_{av} = \frac{\sum_i E_i (d^2\sigma/dEd\Omega)_i}{\sum_i (d^2\sigma/dEd\Omega)_i} \quad (3.5)$$

where  $i$  covers the whole energy spectrum obtained at a particular angle and the corresponding expression of average velocity is given by

$$\begin{aligned} v_{av} &= \sqrt{\frac{2E_{av}}{m_\alpha}} \\ &= \sqrt{(v_{\parallel}^2 + v_{\perp}^2)} \end{aligned} \quad (3.6)$$

where  $m_\alpha$  is the mass of the  $\alpha$  particle,  $v_{\parallel} = v_{av} \cos \theta_{lab}$  is the parallel and  $v_{\perp} = v_{av} \sin \theta_{lab}$  perpendicular components of the particle's velocity,  $v_{av}$ , detected at angle  $\theta_{lab}$  with respect to the beam direction, as explained in Fig. 3.9. These parallel and perpendicular

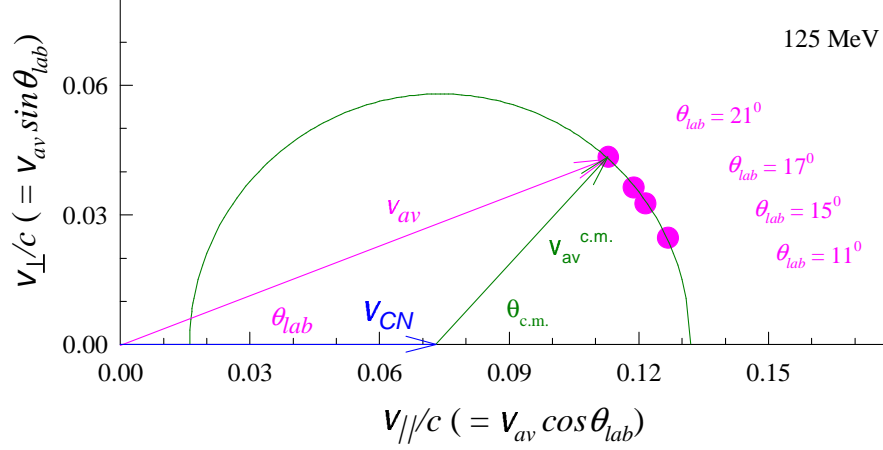


**Figure 3.9:** Average velocity curve of the  $\alpha$ -particle in laboratory frame. Solid pink circles corresponds to experimental data measured at different angle mentioned in the figure and solid lines show fit to the data obtained using Eq. 3.7. The blue, green, and pink arrows indicate the velocity of the composite nucleus in lab ( $v_{CN}$ ), average velocity of  $\alpha$ -particle in c.m. ( $v_{av}^{c.m.}$ ), and average velocity of  $\alpha$ -particle in lab frame ( $v_{av}$ ), respectively .

components of the average velocity at each angle have been plotted in Fig. 3.10. If the particles are emitted from an energy equilibrated composite, in c.m. frame average velocity of the particles emitted at all angles will be the same. In that case, average velocity of the particle in c.m. frame,  $v_{av}^{c.m.}$ , can be written as,

$$\begin{aligned}
 (v_{av}^{c.m.})^2 &= v_{av}^2 + v_{CN}^2 - 2v_{av} \cos \theta_{lab} v_{CN} \\
 &= v_{\perp}^2 + v_{\parallel}^2 + v_{CN}^2 - 2v_{\perp} v_{CN} \\
 &= v_{\perp}^2 + (v_{\parallel} - v_{CN})^2
 \end{aligned} \tag{3.7}$$

which is a equation of a circle in  $v_{\perp}$  vs.  $v_{\parallel}$  plot with centre at  $v_{CN}$ , the velocity of the composite in laboratory frame, and radius  $v_{av}^{c.m.}$ . All the experimental data in Fig. 3.10 have been fitted with Eq. 3.7 and shown by solid lines. Well fitting of the experimental data with Eq. 3.7 implies that the average velocities or the energies of the  $\alpha$ -particles

are independent of the centre of mass emission angles. It has also been found that the value of  $v_{CN}$  obtained from the fitting is well matched with the velocity of composite extracted from the beam energy, using expression given below

$$v_{CN} = \frac{A_{proj}}{A_{proj} + A_{tar}} \sqrt{\frac{2E_{lab}}{A_{proj}}} \quad (3.8)$$

where  $A_{proj}$ , and  $A_{tar}$  the atomic mass number of the projectile and target, respectively. It again indicates that the  $\alpha$ -particles are emitted from a fully energy equilibrated source moving with the velocity,  $v_{CN}$ .

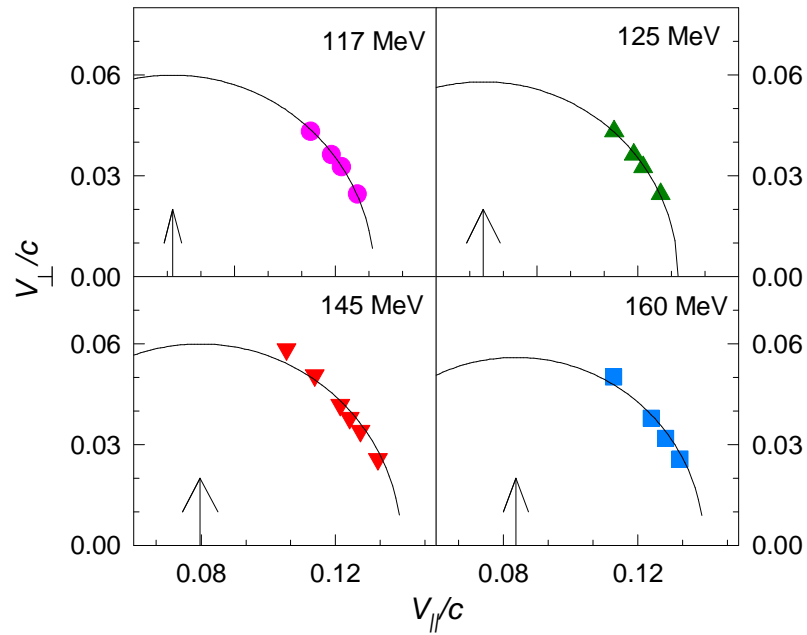


**Figure 3.10:** Average velocity curve. Symbols corresponds to experimental data and solid lines show fit to the data obtained using equation  $v_{\perp}^2 = v_{c.m.}^2 - (v_{\parallel} - v_{CN})^2$ . The arrows indicate the position of  $v_{CN}$ .

### 3.2.4 Statistical model calculations

All the experimental signatures e.g., energy and angular distributions, average velocity etc. show that the  $\alpha$ -particles are emitted from a composite which is fully energy equilibrated. It is known in the earlier works [96] that the experimental signatures of

FF and DIO are nearly the same; in both cases, the composite is fully equilibrated in energy. However, in DIO, the composite remains in the form of a long-live dinucleus, which decays before attaining the fully equilibrated spherical shape (fusion). Therefore, the composite formed in DIO has larger deformation. But, the evaporative decay of the excited composite should be of statical in nature due to the attainment of ‘thermal’ equilibrium in both cases. So, the present experimental data may be explained in the framework of statistical model. The theoretical framework of statistical model has already been discussed in Ch.1. Details of the present analysis using statistical model code CASCADE [7] are given below.

#### 3.2.4.1 Input parameters

The standard form of CASCADE is quite successful in explaining the LCP evaporation in light ion induced reaction in general, where the compound nucleus is assumed to be nearly spherical. On the other hand, in case of heavy ion induced reaction, there is appreciable deviation between the experimental and the predicted LCP evaporation spectra. This deviation is attributed to the deformation of the excited compound system, which is angular momentum dependent. Therefore, in order to explain the energy spectra of LCP, the effects of the deformation of the CN should be included in the statistical model calculations. The deformation affects the particle spectra in two ways. First, it lowers the effective emission barrier, and second, it increases the moment of inertia. The first effect modifies the transmission coefficients for the evaporated particles which may be taken care of by increasing the radius parameter of optical model potential. On the other hand, the change in momentum of inertia affects the level density and the slope of the high energy part of the particle spectrum. This can be taken care of by incorporating the spin dependent ‘deformability’ parameters [103, 100, 104]. For level density calculations, the excited energy has been divided into three regions:

**Region I** (low excitation energy,  $E \leq 3$  to 4 MeV): Here, the experimentally known discrete levels are used for all nuclei produced in the decay cascade. In some cases,

known high-spin states at higher excitation energy, are included as Yrast levels in region II.

**Region II** (medium excitation energy,  $4 \text{ MeV} \leq E \leq 7.5 \text{ MeV}$ ): Analytical level density formula is used in this region. The parameters  $a$  and  $\Delta$  are deduced empirically for each nucleus from the work of Vonach *et al.* [105] and Dilg *et al.* [106]. The excitation energy is corrected for the parity effects.

**Region III** (high excitation energy,  $E \geq E_{LDM}$ ): Shell effects and parity corrections are neglected in this region. The same formula is then used but with LDM parameters are taken from Ref. [107].

Between the regions II and III, the level density parameters are interpolated linearly. The parameters are given in Table 3.1. The level densities used in the regions II and III for a given angular momentum  $\ell$  (All the systems studied under the present have zero intrinsic spin. So, here after we shall write total angular momentum  $J$  as  $\ell$ .) and excitation energy  $E$ , are given by well known Fermi gas expression with equidistant single-particle levels and a constant level density parameter  $a$ :

$$\rho(E, \ell) = \frac{(2\ell + 1)}{12} a^{1/2} \left( \frac{\hbar^2}{2\mathcal{I}_{eff}} \right)^{3/2} \frac{1}{(E + T - \Delta - E_\ell)^2} \exp \left[ 2\{a(E - \Delta - E_\ell)\}^{1/2} \right] \quad (3.9)$$

where  $T$  is the thermodynamic temperature,  $\Delta$  is the pairing correction. The rotational energy,  $E_\ell$ , is expressed as,

$$E_\ell = \left( \frac{\hbar^2}{2\mathcal{I}_{eff}} \right) \ell(\ell + 1). \quad (3.10)$$

The effective moment of inertia,  $\mathcal{I}_{eff}$ , is written as,

$$\mathcal{I}_{eff} = \mathcal{I}_0(1 + \delta_1 \ell^2 + \delta_2 \ell^4), \quad (3.11)$$

where  $\mathcal{I}_0 (= \frac{2}{5} A^{5/3} r_0^2)$  is the rigid body moment of inertia,  $\delta_1$  and  $\delta_2$  are the ‘deformability’ parameters,  $r_0$  is the radius parameter,  $a$  is the level density parameter. So, from all the above equations, it is clear that by changing  $r_0$ ,  $a$ ,  $\delta_1$ , and  $\delta_2$ , it may be possible to reproduce the experimental spectra. By increasing  $r_0$ , both transmission coefficient and level density will be affected. It reduces the potential barrier, leading to the increase of transmission coefficient. Simultaneously, the increase in  $r_0$  leads to

increase of the  $\mathcal{I}_{eff}$  and *vis-à-vis* the available phase space. We have chosen  $r_0 = 1.29$  fm which reproduced the lower energy part of the spectra. Similar value was used in Ref. [108]. To reproduce the present experimental spectra, we have only changed the ‘deformability’ parameters  $\delta_1$  and  $\delta_2$ , like the previous works [100, 109, 103].

### 3.2.4.2 Experimental spectra and CASCADE predictions

The measured energy spectra have been compared with the respective CASCADE [7] calculations which are shown in Fig. 3.11. The critical angular momenta,  $\ell_{cr}$ , used in the calculation, were 20, 21, 22, and 23( $\hbar$ ) for the bombarding energies of 117, 125, 145, and 160 MeV, respectively [Sec. 3.1.5]. The other input parameters are given in Table 3.1. The dash-dot-dash lines represent the results of the CASCADE calculation with the radius parameter  $r_0 = 1.29$  fm and the default values of the deformability parameters,  $\delta_1^A = 3.7 \times 10^{-4}$  and  $\delta_2^A = 1.1 \times 10^{-6}$ , at all beam energies which have been predicted by rotating liquid drop model (RLDM) [113]. The low-energy part of the experimental  $\alpha$ -particle spectra is found to match with the theoretical spectra, but higher energy part does not. To reproduce the whole spectra, we have followed the procedure proposed by Huizenga *et al.*[103]. The ‘deformability’ parameters  $\delta_1$  and  $\delta_2$  have been suitably optimized to reproduce the experimental spectra, which in effect modified the phase space for statistical decay by relocation of the Yrast line. The optimized values of ‘deformability’ parameters,  $\delta_1^B$  and  $\delta_2^B$  are given in Table 3.2 and the calculated energy distribution using these parameters are shown in Fig. 3.11.

### 3.2.5 Quadrupole deformation calculation

The deformation of the excited composite may be expressed in terms of the standard quadrupole deformation parameter,  $\beta$ , using the procedure given in Ref. [99, 114]. It is assumed that the shapes of the non-deformed and the deformed nuclei are spherical and symmetric ellipsoid in shape with volume  $\frac{4}{3}\pi R_0^3$  and  $\frac{4}{3}\pi abc$ , respectively, where

**Table 3.1:** Input parameters used for CASCADE calculations for the reactions  $^{16}\text{O} + ^{12}\text{C}$  at beam energies 117, 125, 145 and 160 MeV.

---



---

Angular momentum distribution:

Critical angular momentum  $\ell_{cr}$  as in Table 3.2

Diffuseness parameter  $\Delta\ell=1\hbar$

OM potentials of the emitted LCP and neutrons:

- (1) Neutrons: Wilmore and Hodgson [110].
- (2) Protons: Perey and Perey [111].
- (3)  $\alpha$ -particles: Huizenga and Igo [112].
- (4) Multiplication factor of the OM radius: RFACT = 1

Level-density parameters at low excitation:  $E \leq 7.5$  MeV

- (1) Fermi-gas level-density formula with empirical parameters from Dilg *et al.* [106].

Level-density parameters at high excitation:  $E \geq 15$  MeV

- (1) Fermi-gas level-density formula with parameters from LDM (Myers and Swiatecki [107])
- (2) Level-density parameter  $a = A/8 \text{ MeV}^{-1}$

Yrast line

$\mathcal{I}_{eff} = \mathcal{I}_0(1+\delta_1 \ell^2 + \delta_2 \ell^4)$ ,  $\delta_1, \delta_2$  are given in Table 3.2.

$\gamma$ -ray width (Weisskopf units)

- (1)  $E1 = 0.001$
- (2)  $M1 = 0.01$
- (3)  $E2 = 5.0$

---



---

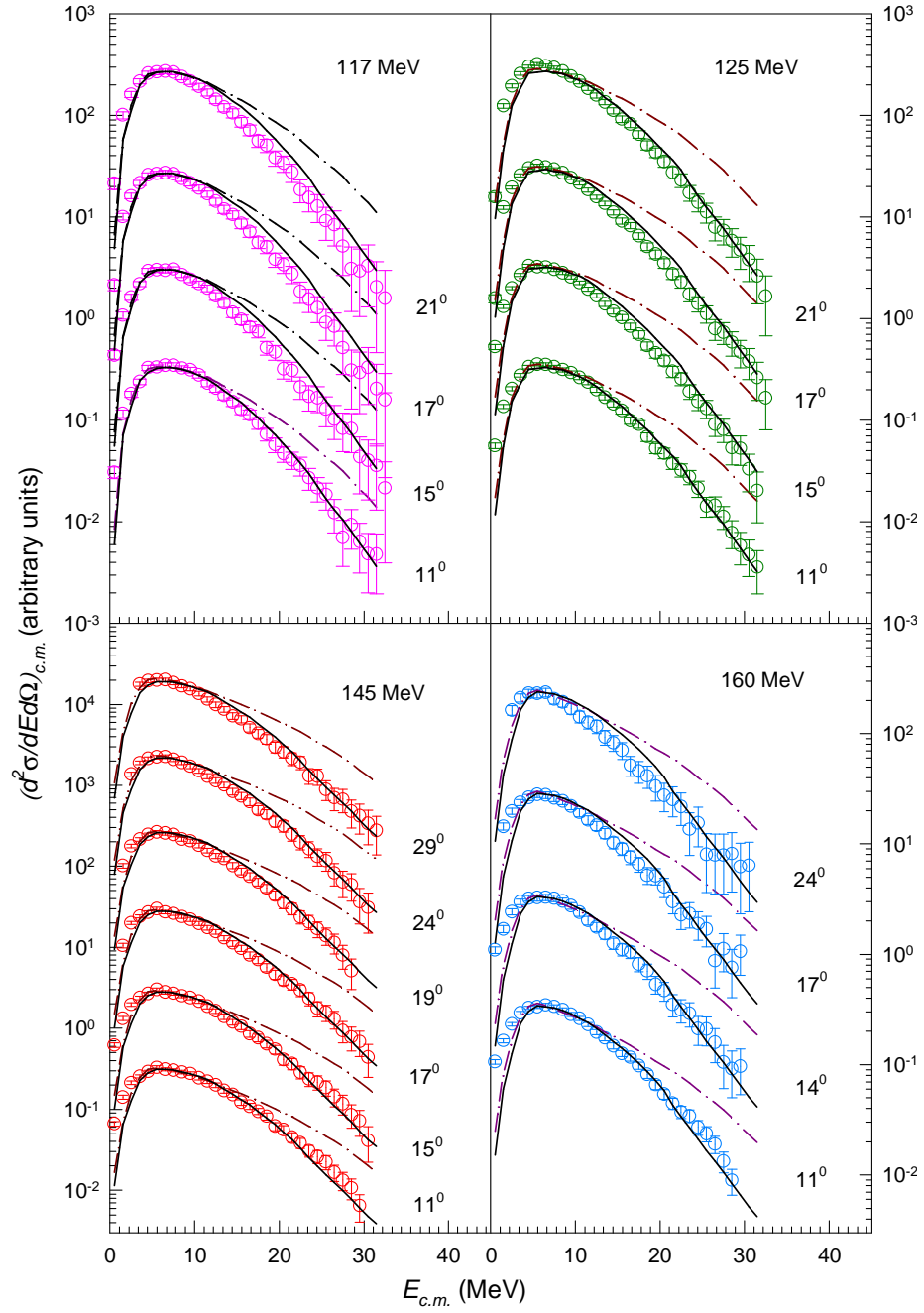


**Figure 3.11:** Energy spectra (c.m.) of  $\alpha$  particles obtained at different angles for different beam energies. The symbols represent experimental data. The dash-dot-dash and solid lines represent CASCADE calculations with default and optimized values of spin dependent ‘deformability’ parameters, respectively (see Table 3.2). All experimental and calculated spectra, starting from the lowest angle, were multiplied by  $10^{-2}$ ,  $10^{-1}$ ,  $10^0$ ,  $10^1$ ,  $10^2$ ,  $10^3$ , respectively.

**Table 3.2:** The values the of ‘deformability’ parameters:  $A$  - obtained from RLDM, and,  $B$  - obtained by fitting the experimental data (see text) have been given below.  $E_{lab}$ ,  $E$ ,  $\ell_{cr}$  and  $\ell_{av}$  are the beam energy, excitation energy, critical angular momentum and average angular momentum, respectively.

$E_{lab}$	$E$	$\ell_{cr}$	$\ell_{av}$	$\delta_1^A$	$\delta_2^A$	$\delta_1^B$	$\delta_2^B$
117	67	20	13	$3.7 \times 10^{-4}$	$1.1 \times 10^{-6}$	$1.9 \times 10^{-3}$	$2.0 \times 10^{-8}$
125	70	21	14	$3.7 \times 10^{-4}$	$1.1 \times 10^{-6}$	$2.1 \times 10^{-3}$	$2.0 \times 10^{-8}$
145	79	22	15	$3.7 \times 10^{-4}$	$1.1 \times 10^{-6}$	$2.3 \times 10^{-3}$	$2.0 \times 10^{-8}$
160	85	23	15	$3.7 \times 10^{-4}$	$1.1 \times 10^{-6}$	$2.5 \times 10^{-3}$	$2.0 \times 10^{-8}$

$R_0$  is the radius for non-deformed nucleus and  $a$ ,  $b$ ,  $c$  are the three semi-axis of the ellipsoid with sharp surfaces [103]. The effective moment of inertia can be expressed as,

$$\mathcal{I}_{eff} = \frac{2}{5}MR_{eff}^2 = \frac{1}{5}M(a^2 + b^2), \quad (3.12)$$

where  $c$  is the axis of rotation. In case of prolate shape,  $a = c$  and  $b$  ( $> a, c$ ) is the symmetry axis. So, from Eqs. 3.11 and 3.12, one obtains,

$$R_{eff}^2 = R_0^2(1 + \delta_1\ell^2 + \delta_2\ell^4) = (1/2)(a^2 + b^2). \quad (3.13)$$

Using Eqs. 3.12 and 3.13 along with the criterion of volume conserving deformation ( $R_0^3 = a^2b$ ), one obtains the following equation for the axis ratio,  $b/a$ ,

$$x^3 + 3x^2 + \lambda x + 1 = 0, \quad (3.14)$$

where  $\lambda = 3 - 8(1 + \delta_1\ell^2 + \delta_2\ell^4)^3$  and  $x = (b/a)^2$ . Using Hill-Wheeler parametrization [115], the ellipsoidal deformation can be expressed as  $a = R_0 \exp[\sqrt{5/4\pi}\beta \cos(\gamma - 2\pi/3)]$ ,  $b = R_0 \exp[\sqrt{5/4\pi}\beta \cos(\gamma + 2\pi/3)]$ ,  $c = R_0 \exp[\sqrt{5/4\pi}\beta \cos \gamma]$  where  $\beta$ , and  $\gamma$  are the quadrupole deformation, and shape parameter, respectively. So,  $\beta$  can be expressed as,

$$\beta = \frac{2}{3} \left( \frac{4\pi}{5} \right)^{1/2} \ln\left(\frac{b}{a}\right) = 1.057 \ln\left(\frac{b}{a}\right). \quad (3.15)$$

**Table 3.3:** The values of the quadrupole parameters: A - obtained from ‘deformability’ using RLDM, and, B - extracted using ‘deformability’ parameters obtained by fitting the experimental data. The ‘deformability’ parameters are given in Table 3.2.

$E_{lab}$	$(b/a)_{\ell_{av}}^A$	$\beta_{\ell_{av}}^A$	$(b/a)_{\ell_{av}}^B$	$\beta_{\ell_{av}}^B$
117	1.23	0.22	1.63	0.52
125	1.27	0.25	1.77	0.60
145	1.32	0.29	1.92	0.69
160	1.32	0.29	1.98	0.72

The values of  $b/a$  and  $\beta$  extracted for two different sets of ‘deformability’ parameters ( those obtained from RLDM [113] and from fitting CASCADE calculations with the present data) have been given in Table 3.3. Typical uncertainty in the estimation of  $\beta$  was  $\approx 15\%$ . The above results are clearly indicative of the presence of substantial quadrupole deformation in  $^{28}\text{Si}^*$  produced through the reaction  $^{16}\text{O} + ^{12}\text{C}$  at all energies, and the deformation is found to increase with increasing the spin of the excited composite.

## Chapter 4

### Result: Fragment emission in $^{12}\text{C} + ^{28}\text{Si}$ , $^{12}\text{C} + ^{27}\text{Al}$ , $^{11}\text{B} + ^{28}\text{Si}$ reactions

The complex fragment emission from the reactions 77 MeV  $^{12}\text{C} + ^{28}\text{Si}$ , 73 MeV  $^{12}\text{C} + ^{27}\text{Al}$ , 64 MeV  $^{11}\text{B} + ^{28}\text{Si}$  have been studied at the excitation energy of  $\sim 67$  MeV. The main aim of this study is to compare the emission mechanism of the fragments from  $\alpha$ -cluster system,  $^{40}\text{Ca}^*$ , produced in  $^{12}\text{C} + ^{28}\text{Si}$  and nearby non  $\alpha$ -cluster system  $^{39}\text{K}^*$  produced via two different reactions,  $^{12}\text{C} + ^{27}\text{Al}$  and  $^{11}\text{B} + ^{28}\text{Si}$ . The last two reactions have been chosen to cross check the equilibrium decay nature (absence of entrance channel dependence) of the energy damped binary fragment yield in the decay of  $^{39}\text{K}^*$ .

The typical energy spectra of the fragments Li, Be and B emitted in these reactions have been shown in Fig. 4.1. It is evident from the figure that there are significant differences in the shapes of the spectra obtained in the three reactions. This is mainly due to the variation of the relative contributions of different reaction processes to the fragment yield. It is known from theoretical [17, 50, 51, 52, 53, 54, 55, 56] and experimental [12, 26, 29, 31, 32, 57, 58, 59, 60, 61, 62, 63, 64, 65, 66, 67, 68, 69, 70, 71, 72, 73, 74, 75, 76, 77, 78, 79, 80, 81, 82, 83, 84, 85] studies of complex fragment emission in low and intermediate energy nucleus-nucleus collision that, the origin of

complex fragments is broadly due to fusion-fission (FF) and non-fusion (deep inelastic collision, deep inelastic orbiting, quasi elastic, breakup, etc.) processes. The quasi-elastic process contributes to the yields of fragments around the entrance channel only and has a strongly forward peaked (around grazing angle) angular distribution. On the other hand, in deep inelastic (DI) collision, mass and angular distributions are much broader, particularly for the lighter systems considered here. So, there is strong overlap in the elemental distributions of the fragments originating from FF and DI processes in

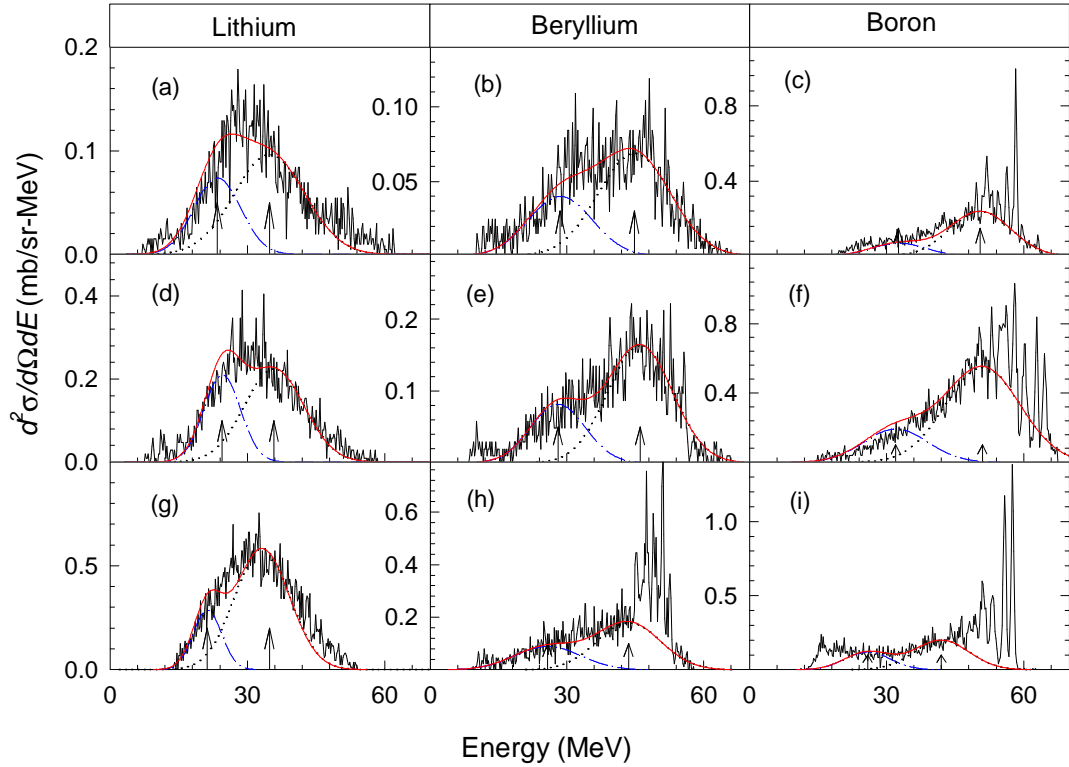


**Figure 4.1:** Typical energy spectra of the fragments measured for the reactions  $^{12}\text{C} + ^{28}\text{Si}$  (a - c),  $^{12}\text{C} + ^{27}\text{Al}$  (d - f) and  $^{11}\text{B} + ^{28}\text{Si}$  (g - i) at  $\theta_{lab} = 17.5^\circ$  (a - h) and  $30^\circ$  (i). The blue dash-dotted, the black dotted, and the red solid curves represent the contributions of the FF, the DI, and the sum (FF + DI), respectively. The left and the right arrows correspond to the centroids of FF and DI components of energy distributions, respectively.

the light systems, which make it very difficult to separate the contributions of DI and FF processes from the total spectrum. In addition, since in the present study, one of the systems ( $^{12}\text{C} + ^{28}\text{Si}$ ) under study is an  $\alpha$ -cluster system, there is a possibility of the

contribution of deep inelastic orbiting (DIO) in the total fragment yield. As the experimental signatures of both FF and DIO are same, DIO contribution will be automatically mixed up (if any) with FF yield. To separate out the contributions of FF and DI from the total yield, the procedure given in the Ref. [21, 94] has been followed and the same has been explained in Fig. 4.2. The contributions of FF and DI processes have been represented by two separate Gaussian functions. The centroid of the Gaussian representing the FF yield has been obtained from Viola systematics [116], duly corrected

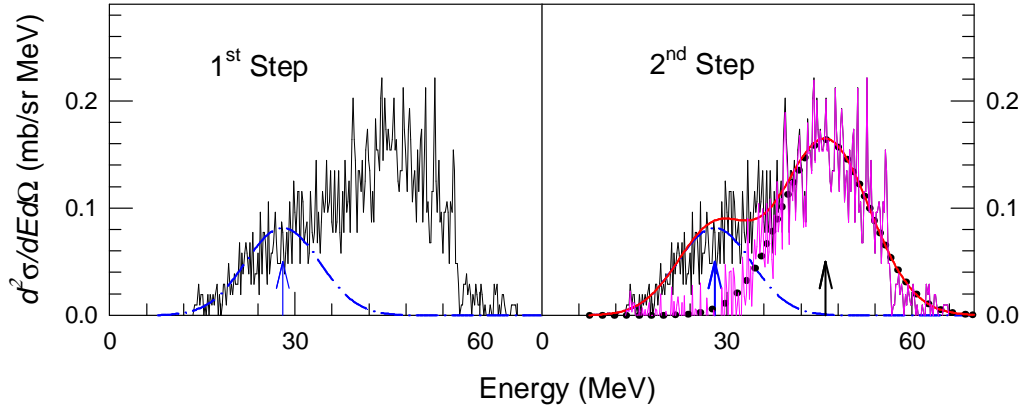


**Figure 4.2:** The typical extraction procedure of FF and DI components from the total energy spectrum of Be fragment measured in the reaction  $^{12}\text{C} + ^{27}\text{Al}$  at  $\theta_{lab} = 17.5^\circ$ . Detail of the extraction procedure is given in the text. The arrow at low and higher energy indicates the FF and DI peaks, respectively.

for the asymmetric factor [44], and the width of the Gaussian (blue dash-dot curve) has been obtained by fitting the lower energy tail of the spectrum. The area under this Gaussian gives the yield from FF. In the next step, this Gaussian has been subtracted from the total energy spectra, as shown by pink color curve. This subtracted spectrum has then been fitted with another Gaussian (black dotted curve) which represents DI contribution. The contributions of FF and DI components thus obtained for each fragment from each reaction have been displayed in the Fig. 4.1. Besides the FF and DI components, there are some other contribution in the yield of fragments B and/or Be in all systems which are seen as sharp peaks in Fig. 4.1. These peaks are due to one nucleon transfer for B (C + Si, C + Al) and Be (B + Si). In case of B fragment emitted

in the reaction B + Si, sharp peaks are due to elastic and inelastic scattering. But all these peaks are excluded in extraction of FF and DI component by proper fitting of the corresponding Gaussians.

## 4.1 Study of fusion-fission fragments

### 4.1.1 Angular distribution

The angular distribution of differential cross section,  $\left(\frac{d\sigma}{d\Omega}\right)_{lab}$  (in laboratory frame), of the fragments of FF origin has been obtained by integrating the area under the corresponding Gaussian (1<sup>st</sup>) extracted from energy spectrum at each angle. The obtained

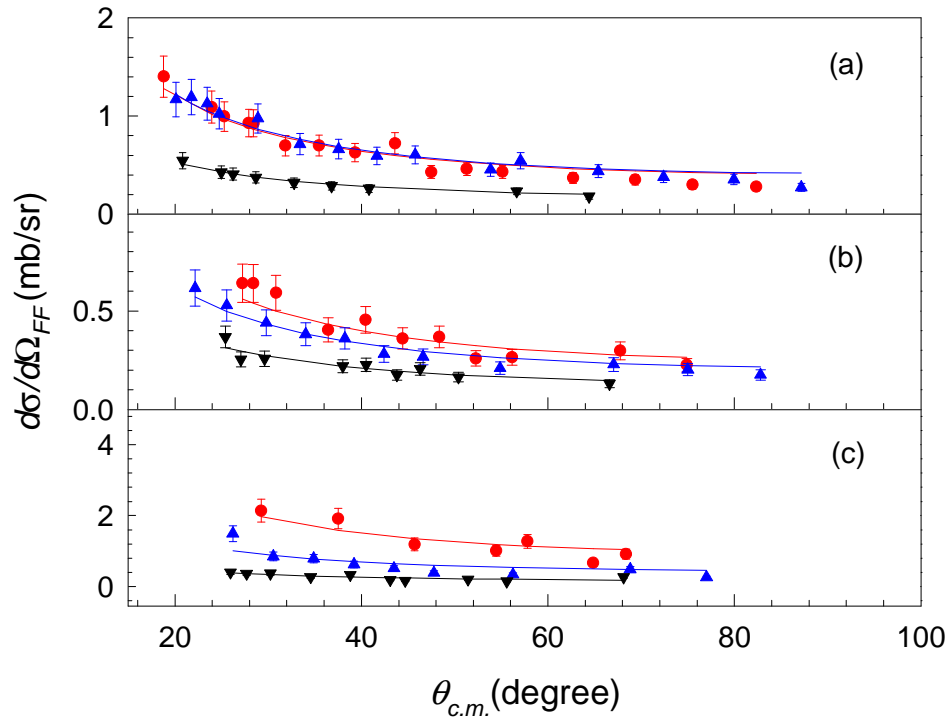


**Figure 4.3:** The c.m. angular distributions of the fragments Li (a), Be (b) and B (c). Solid circles (red), triangles (blue) and inverted triangles (black) correspond to the experimental data for the reactions  $^{11}\text{B} + ^{28}\text{Si}$ ,  $^{12}\text{C} + ^{27}\text{Al}$  and  $^{12}\text{C} + ^{28}\text{Si}$ , respectively. Solid curves are fit to the data with the function  $f(\theta_{c.m.}) \propto 1/\sin\theta_{c.m.}$ .

value of  $\left(\frac{d\sigma}{d\Omega}\right)_{lab}$  has been converted to c.m. frame by using Eq. 2.11, assuming two-body kinematics averaged over total kinetic energy distribution and the corresponding angle,  $\theta_{lab}$  in laboratory frame, has been transformed by using Eq. 2.13. The c.m. angular distributions  $(d\sigma/d\Omega_{FF})$  so obtained for the fragments (Li, Be and B) have been shown in Fig. 4.3 for all three reactions. Each experimental angular distribution data has been fitted with a function  $f(\theta_{c.m.}) = C/\sin\theta_{c.m.}$ , where  $C$  is constant parameter and the fitted curve is shown by solid lines. It is evident from the figure that the angular distributions of all FF fragments follow  $\sim 1/\sin\theta_{c.m.}$  dependence which is characteristic

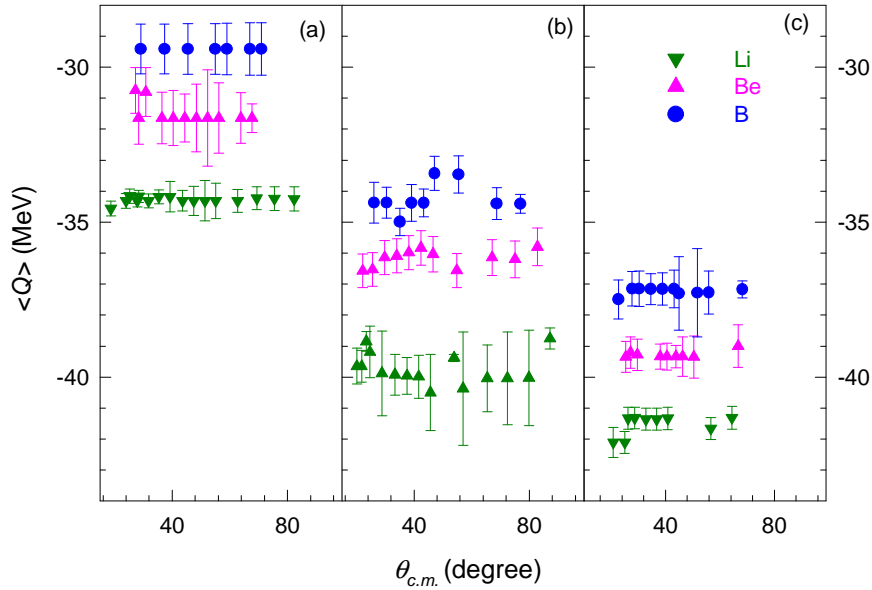


**Figure 4.4:** Average  $Q$ -values of the FF fragments Li, Be and B represented by inverted green triangle, pink triangle and blue circle, respectively for reactions (a)  $B + Si$ , (b)  $C + Al$  and (c)  $C + Si$ .

of the fission-like decay of an equilibrated composite system. It is also observed from the figure that the yields of Li and Be are almost same at all angles for  $^{11}B + ^{28}Si$  and  $^{12}C + ^{27}Al$  reactions. It has further been found that the yield of the fragment Boron in  $^{11}B + ^{28}Si$  reaction is more than the same in  $^{12}C + ^{27}Al$  reaction. It has also been observed that the fragment angular yields for the reactions  $^{11}B + ^{28}Si$  and  $^{12}C + ^{27}Al$  are a little higher (though nearly comparable in magnitude) than those obtained in  $^{12}C + ^{28}Si$  reaction at the same excitation energy.

### 4.1.2 Angular distribution of $Q$ -value

In the present study of fragment emission, it has been observed that  $\langle Q \rangle$  are nearly constant for all the FF fragments emitted from  $^{11}\text{B} + ^{28}\text{Si}$ ,  $^{12}\text{C} + ^{27}\text{Al}$  and  $^{12}\text{C} + ^{28}\text{Si}$  as shown in Fig. 4.4. The independence of  $\langle Q \rangle$  with respect of emission angles suggest that, the fragments are emitted from a completely energy equilibrated system at all beam energies.

### 4.1.3 Total fragment yield

The total yields of the FF fragments have been shown in Fig. 4.5. These total FF fragment yield has been obtained by integrating the angular distribution,  $d\sigma/d\Omega_{FF} = C/\sin\theta_{c.m.}$ , over the whole angular range. The yields of the fragments Li and Be in  $^{11}\text{B} + ^{28}\text{Si}$  and  $^{12}\text{C} + ^{27}\text{Al}$  reactions are found to be nearly the same which confirms their compound nuclear origin. It has also been observed that the yields of these

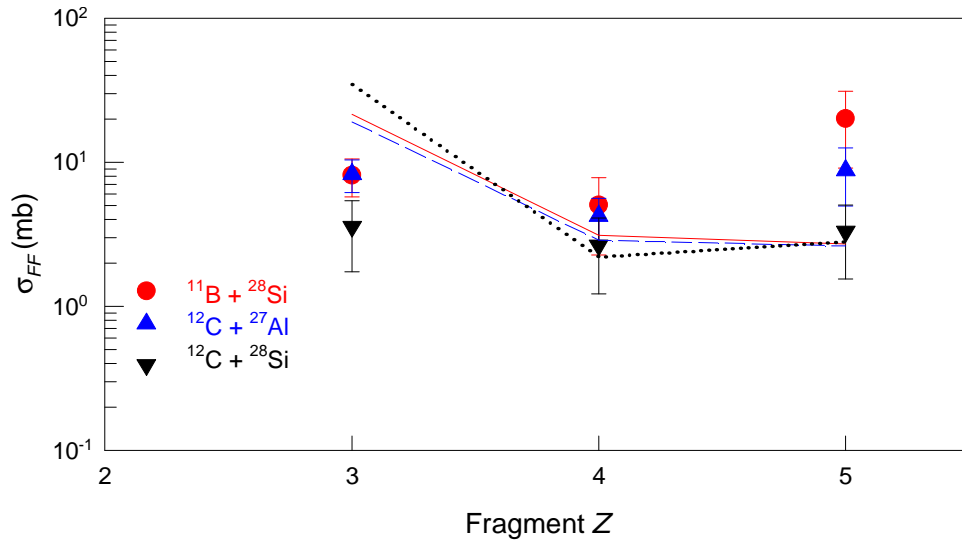


**Figure 4.5:** The total FF fragment cross sections (c.m.) for the three reactions. The solid circles (red), triangles (blue), and inverted triangles (black) correspond to the experimental data for  $^{11}\text{B} + ^{28}\text{Si}$ ,  $^{12}\text{C} + ^{27}\text{Al}$ , and  $^{12}\text{C} + ^{28}\text{Si}$  reactions, respectively. The solid (red), dashed (blue) and dotted (black) lines are the corresponding theoretical predictions.

fragments are comparable to those obtained in  $^{12}\text{C} + ^{28}\text{Si}$  reaction. The yield of B in the reaction  $^{11}\text{B} + ^{28}\text{Si}$  has been found to be slightly more than that obtained in the other two reactions, which might be due to the contamination from the beam-like channels in the former case, where B was the projectile. The experimental FF fragment yields have been compared with the theoretical estimates of the same obtained from the extended Hauser-Feshbach model (EHFM) [18]. The values of the critical angular momenta have been obtained from the experimental fusion cross section data, wherever available [117, 118]; otherwise, they have been obtained from the dynamical trajectory model calculations with realistic nucleus-nucleus interaction and the dissipative forces generated self-consistently through stochastic nucleon exchanges [98]. The values of the critical angular momentum,  $\ell_{cr}$ , for all the three systems, have been the same ( $27\hbar$ ). The calculated fragment emission cross sections have been shown in Fig. 4.5. It is seen from the figure that in all three cases, the theoretical predictions are nearly the same and are in fair agreement with the experimental results.

## 4.2 Study of DI fragments

### 4.2.1 Angular distribution

The angular distribution of DI component of the fragment-yield has been obtained by integrating the respective Gaussian ( $2^{nd}$ ) extracted from the energy distribution. The obtained angular distributions  $(d\sigma/d\Omega)_{lab}$  have been converted to c.m. frame,  $d\sigma/d\Omega_{DI}$ , using the same procedure discussed in Sec. 4.1.1 and have been displayed in Fig. 4.6. It is observed that  $d\sigma/d\Omega_{DI}$  forward peaked and falls off with  $\theta_{c.m.}$  much faster than  $\sim 1/\sin\theta_{c.m.}$  distribution. This is an indication of the non-equilibrium nature of the emission. To reproduce the angular distribution of the fragments originating from DI, several models are available in the literature. For example, it can be explained, classically, in terms of the evolution of a viscous or rigidly rotating dinuclear system [119, 24, 25, 26] as discussed in Sec. 1.2.1.3 and the angular distribution can

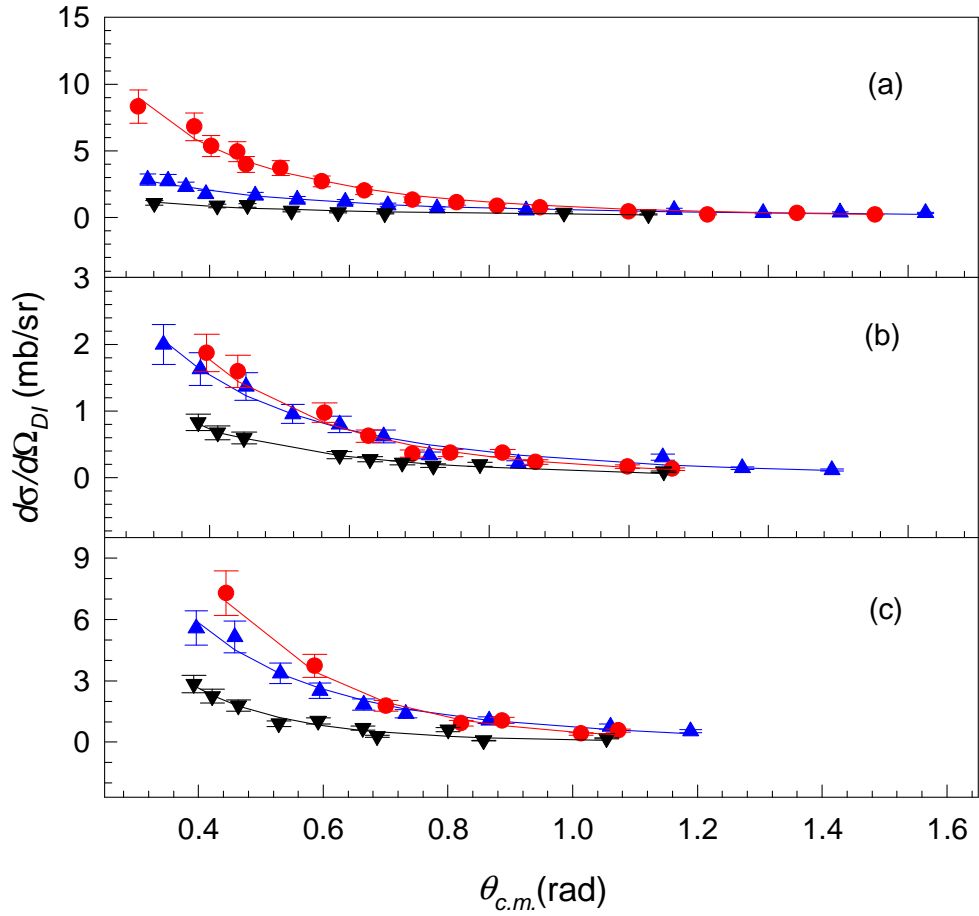


**Figure 4.6:** The *c.m.* angular distributions of the DI fragments [Li (a), Be (b), and B (c)]. The solid circles (red), triangles (blue), and inverted triangles (black) correspond to the experimental data for  $^{11}\text{B} + ^{28}\text{Si}$ ,  $^{12}\text{C} + ^{27}\text{Al}$ , and  $^{12}\text{C} + ^{28}\text{Si}$  reactions, respectively; the solid lines are the fits to the data (see text).

be expressed by Eq. 1.22. When  $\tau \gg 2\pi/\omega$  (dinucleus rotation period), the angular distribution takes the form

$$(d\sigma/d\Omega)_{c.m.} = C/\sin\theta_{c.m.} \quad (4.1)$$

which is expected in case of fusion as seen in Sec. 4.1.1. So, angular distribution of DI fragments falls (Eq. 1.22) faster than the same of FF fragments. This faster fall indicates shorter lifetime of the composite system. Such a shorter lifetime (less than the time period of dinuclear rotation) is not sufficient for the formation of an equilibrated compound nucleus, but may still cause significant energy damping within

**Table 4.1:** Emission time scale of different DI fragments for all three reactions.

<i>System</i>	Frag.	<i>C</i>	$\omega\tau_{DI}^{cr}$	$\tau_{DI}^{cr}(\times 10^{-22}\text{s})$	Err.
C + Si	Li	0.49	1.05	22.69	$\pm 3.64$
	Be	0.76	0.41	8.94	$\pm 0.70$
	B	5.17	0.25	5.34	$\pm 2.25$
C + Al	Li	1.22	0.92	20.14	$\pm 2.94$
	Be	1.30	0.51	11.28	$\pm 1.35$
	B	5.52	0.45	9.89	$\pm 1.34$
B + Si	Li	5.23	0.43	9.77	$\pm 0.96$
	Be	2.07	0.36	8.17	$\pm 1.15$
	B	16.32	0.27	6.14	$\pm 0.39$

the deep-inelastic collision mechanism. In Fig. 4.6, the solid lines represent the fit to the experimental data using Eq. 1.22  $[(d\sigma/d\Omega)_{c.m.} = (C/\sin\theta_{c.m.})e^{-\theta_{c.m.}/\omega\tau}]$ . From this fitting, the lifetime of the intermediate dinuclear complex has been estimated. The time scales for different DI fragments (Li, Be and B) thus obtained (for angular momentum  $\ell = \ell_{cr}$ ) have been compared in Fig. 4.7 and also in Table 4.1. It is seen that, in all reactions, the time scale decreases as the fragment charge increases, which agrees with a previous study by Mikumo *et al.* [25]. This is expected because the heavier fragments (nearer to the projectile) require less nucleon exchange and therefore less time; on the other hand, the emission of lighter fragments requires more nucleon exchange and therefore longer times. The emission time scales of the fragments are related to the number of nucleons exchanged on the average. This explains why the emission time scales of  $^{12}\text{C} + ^{27}\text{Al}$  and  $^{12}\text{C} + ^{28}\text{Si}$  reactions are nearly the same for all fragments. On the other hand, in the case of  $^{11}\text{B} + ^{28}\text{Si}$  reaction, net nucleon exchange is one less to reach any particular fragment; so the corresponding time scales are less. For example, in terms of net nucleon exchange, the emission time scale of Li (Be) from  $^{11}\text{B} + ^{28}\text{Si}$  should be comparable to that of Be (B) from  $^{12}\text{C} + ^{27}\text{Al}$  and  $^{12}\text{C} + ^{28}\text{Si}$  reactions, which is actually the case (Fig. 4.7).

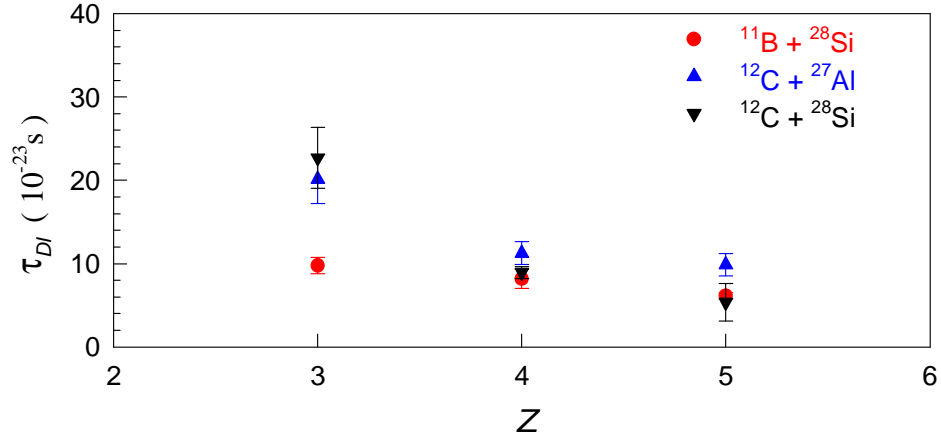


Figure 4.7: The emission time scales of different DI fragments.

### 4.2.2 Average Q-value

The average  $Q$ -values ( $\langle Q_{DI} \rangle$ ) of the DI fragments, estimated from the corresponding fragment kinetic energies assuming two-body kinematics, have been displayed in Fig. 4.8 as a function of the c.m. angle. It is found that, for all fragments, the  $\langle Q_{DI} \rangle$  values tend to decrease with the increase of angle for  $\theta_{c.m.} \lesssim 40^\circ$ , and then gradually become nearly constant. It implies that, up to  $\theta_{c.m.} \lesssim 40^\circ$ , kinetic energy dissipation is incomplete, whereas beyond this point, the kinetic energy is fully damped and dynamic equilibrium has been established before the scission of the di-nuclear composite takes place.

### 4.2.3 Total fragment yield

The experimental angle integrated yields of the DI fragments for all the reactions are shown in Fig. 4.9. The total DI yields have been obtained by integrating fitted Eq. 1.22 over the full range of angles. It is found that the DI yields of all fragments emitted in B + Si reaction are slightly higher than those obtained in C + Al and C + Si reactions. This may be due to the variation of the probability of net nucleon exchange.

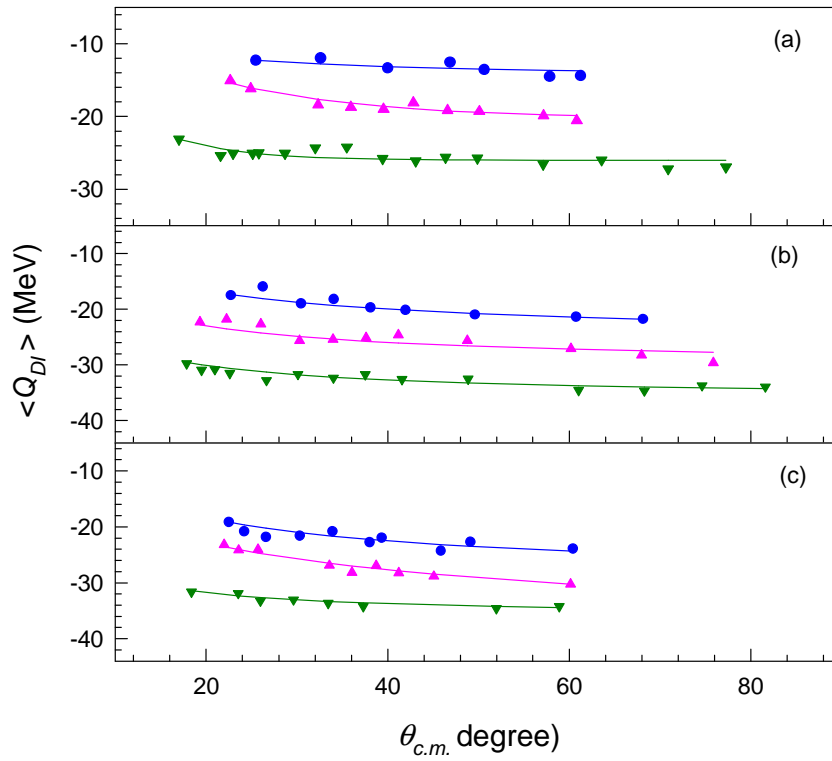


**Figure 4.8:** The average  $Q$ -values,  $\langle Q_{DI} \rangle$ , plotted as function of  $\theta_{c.m.}$  for Li (green inverted triangle), Be (pink triangle), and B (blue solid circle) emitted in (a)  $^{11}\text{B} + ^{28}\text{Si}$ , (b)  $^{12}\text{C} + ^{27}\text{Al}$ , and (c)  $^{12}\text{C} + ^{28}\text{Si}$  reactions. Solid lines are plotted to guide the eye.

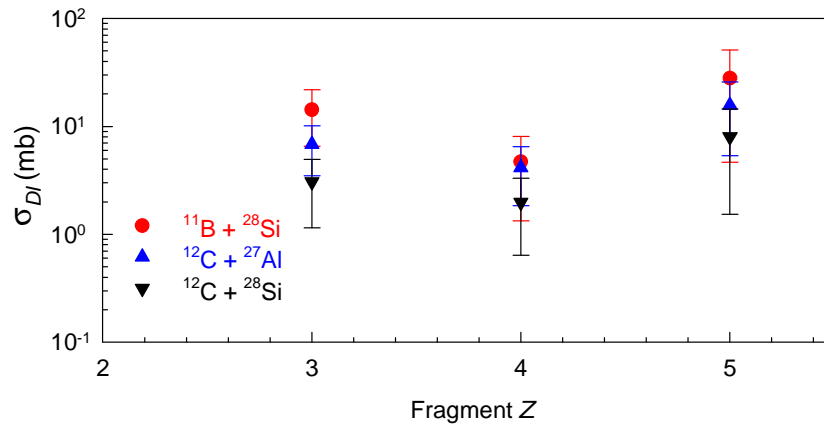


**Figure 4.9:** Total DI cross sections of the fragments obtained in three different reactions.

In addition, the DI fragment yield in C + Si reaction tends to be lower than that for C + Al reaction.

# Chapter 5

## Discussions

### 5.1 $\alpha$ -cluster systems and dinuclear orbiting

The shapes of the energy distributions of the fragments B, Be and Li measured in the reactions  $^{16}\text{O} + ^{12}\text{C}$  for bombarding energies 117, 125, 145 and 160 MeV are similar as shown in Chapter 3. All are found to be peaked around the kinetic energies obtained from Viola systematics [91] corrected by an asymmetry factor [44]. The values of differential cross section  $(d\sigma/d\theta)_{c.m.}$  and average  $Q$ -values of the exit channel,  $\langle Q \rangle$ , are found to be independent of the c.m. emission angle. The observations, viz., large energy damping,  $1/\sin\theta_{c.m.}$  dependence of angular distribution and the near constancy of  $\langle Q \rangle$  over a wide angular range, indicate that the fragments originate from a long-lived, fully energy equilibrated composite,  $^{28}\text{Si}^*$  ( $^{16}\text{O} + ^{12}\text{C}$ ). The linear dependence of angle averaged  $Q$ -value,  $\langle \bar{Q} \rangle$ , on the c.m. bombarding energy,  $E_{c.m.}$ , also confirms full energy equilibration of the composite. Though the fragments are emitted from an energy equilibrated source, standard statistical model CASCADE [7] cannot explain the angle integrated yield of the fragment, B. It has been observed that there is significant enhancement in the yield of the fragment B over the statistical model predictions which suggests additional contribution from other reaction mechanism e.g., dinuclear orbiting. On the contrary, for Li and Be, the binary yields are explained well

by CASCADE. This may be due to the fact that, for the case of Li and Be, number of nucleon exchange is more and these are of compound nuclear origin. It is also seen that the yields of all the fragments Li, Be, B are underpredicted in EHFM calculations. However, the mismatch between the extracted binary-reaction yields and respective EHFM predictions increase progressively from Li to B (see Fig. 3.5), which clearly indicates, increasing additional contributions from other reaction mechanism as one moves from Li to B. So, notwithstanding the limitations of the statistical model calculations extended to light nuclear system, it is evident that there is clear signature of an enhancement in the yield of B as compared to the predicted yield. Such enhancement in the experimental binary yield with respect to respective theoretical predictions near entrance channel configuration is indicative of the formation of an orbiting dinuclear complex.

The shapes of the energy distributions of the same fragments Li, Be, B are somewhat different in case of other  $\alpha$ -cluster system  $^{12}\text{C} + ^{28}\text{Si}$  (and also in non  $\alpha$ -cluster systems  $^{12}\text{C} + ^{27}\text{Al}$  and  $^{11}\text{B} + ^{28}\text{Si}$ ). Energy distributions of each fragments have two different peaks, first one is originating from equilibrated source and the other from non-equilibrated source. These two different contributions have been separated by fitting the energy distributions with two Gaussians following the procedure given in Chapter 4. The  $1/\sin\theta_{c.m.}$  dependence of angular distribution of yields around the first peak and independence with exit channel  $Q$ -value of the c.m. emission angle confirm the equilibrated nature of its source which is denoted as ‘FF fragments’. The measured FF fragment yields ( $3 \leq Z \leq 5$ ) have been found to be in good agreement with the respective statistical model predictions, EHFM, (see Fig. 4.5), indicative of the compound nuclear origin of these fragments. However, a previous study on the binary decay of the same system [83] (using inverse kinematical reaction) had reported an enhancement of fragment ( $6 \leq Z \leq 8$ ) yield over the statistical model prediction and thereby conjectured the presence of orbiting mechanism.

One of the important features of dinuclear orbiting is that number of open channel (NOC) should be small, which is related to the surface transparency. As it has been

mentioned earlier, the most important signature of orbiting is the observation of enhanced equilibrium fragment yield near the entrance channel configuration. Possible reason for the enhancement may also be due to the contribution of yield coming from secondary de-excitation of the excited primary heavy fragments. Another feature of the orbiting system is that it is usually associated with large deformation. Such large deformation was also observed in other  $\alpha$ -clustered systems, e.g.,  $^{20}\text{Ne} + ^{12}\text{C}$  [120] for which orbiting had also been indicated from the fragment emission study [96]. It is therefore essential to investigate into the role of secondary decay in the fragment yield, NOC and deformation in the composite in order to delineate whether the enhancement is due to feeding from the secondary de-excitation of heavier fragments or from orbiting mechanism. A detailed investigation have been performed which are described in the following subsections.

### 5.1.1 Number of open Channels (NOC)

The calculated NOC for the  $\alpha$ -cluster system  $^{16}\text{O} + ^{12}\text{C}$  [43] have been plotted in Fig. 5.1(a) as a function of grazing angular momentum  $\ell_{gr}$ . In the same plot, NOCs for two neighbouring non  $\alpha$ -cluster systems viz.  $A = 28, 31$ , i.e., ( $^{18}\text{O} + ^{10}\text{B}$  and  $^{19}\text{F} + ^{12}\text{C}$  [43]) have also been shown for the comparison purpose. It is found that NOCs are much larger (e.g.,  $\sim 10^4$  times larger) in case of  $^{18}\text{O} + ^{10}\text{B}$  and  $^{19}\text{F} + ^{12}\text{C}$  system, than those for the  $^{16}\text{O} + ^{12}\text{C}$  system at all the grazing angular momentum. Due to large values of NOC, no resonance was observed in  $^{18}\text{O} + ^{10}\text{B}$  and  $^{19}\text{F} + ^{12}\text{C}$  systems [43, 121, 122]. In a detailed study of the energy damped yield of the binary fragments emitted in the reactions  $^{19}\text{F} + ^{12}\text{C}$  and  $^{18}\text{O} + ^{10}\text{B}$ , it was observed that the fragments were originated from FF rather than through deep-inelastic orbiting processes, which is also in agreement with the observation of large NOCs for these systems [77, 123]. In the present system  $^{16}\text{O} + ^{12}\text{C}$ , the value of characteristic minimum of NOC has been observed at grazing angular momentum  $\ell_{gr}^{ch} = 25\hbar$ . The value of the grazing angular momenta at the incident energy, 117, 125, 145 and 160 MeV at which present

system has been studied, are 27, 28, 31 and 33  $\hbar$  respectively. Though these  $\ell_{gr}$  are more than  $\ell_{gr}^{ch}$ , still corresponding values of NOC are much less compared to those for the other two nearby systems viz.  $^{18}\text{O} + ^{10}\text{B}$  and  $^{19}\text{F} + ^{12}\text{C}$ . Unlike these two nearby systems viz.  $^{18}\text{O} + ^{10}\text{B}$  and  $^{19}\text{F} + ^{12}\text{C}$ , resonances have been observed for the system  $^{16}\text{O} + ^{12}\text{C}$  [72] having lower NOC values. Since quasi molecular resonance at lower energies and orbiting mechanism at higher energies appear to be, conceptually, very closely related, one might expect that the system which shows resonances, should also show orbiting phenomena. In a recent study of the competition between direct and dissipative processes in binary channels in the reactions  $^{16}\text{O} + ^{12}\text{C}$ ,  $^{18}\text{O} + ^{12}\text{C}$  at energies 5 - 7.7 MeV /nucleon [72], the observation of resonant structure at lower energies and presence of refractive effects at higher energies, may be considered as the signature of the orbiting process.

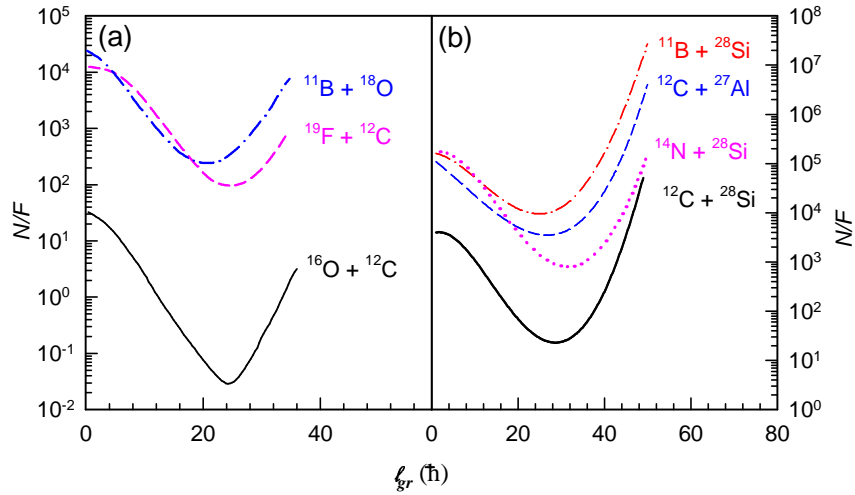


**Figure 5.1:** Number of open channels for decay of composite nucleus (a)  $^{28}\text{Si}^*(^{16}\text{O} + ^{12}\text{C})$ ,  $^{31}\text{P}^*(^{19}\text{F} + ^{12}\text{C})$  and  $^{28}\text{Al}^*(^{10}\text{B} + ^{18}\text{O})$  and (b)  $^{12}\text{C} + ^{28}\text{Si}$ ,  $^{14}\text{N} + ^{28}\text{Si}$ ,  $^{11}\text{B} + ^{28}\text{Si}$ ,  $^{12}\text{C} + ^{27}\text{Al}$ , normalized to the incident flux,  $N/F$ , plotted as a function of grazing angular momentum,  $\ell_{gr}$ .

NOCs for the system  $A = 40$ , i.e.,  $^{12}\text{C} + ^{28}\text{Si}$  and  $A = 42$  ( $^{14}\text{N} + ^{28}\text{Si}$ ) have also been calculated and been plotted in Fig. 5.1(b). It is seen that, the number of open reaction channels for the system  $^{14}\text{N} + ^{28}\text{Si}$  is much larger compared to  $^{12}\text{C} + ^{28}\text{Si}$  reaction [12]. Though the system  $^{28}\text{Si} + ^{14}\text{N}$  is a non- $\alpha$  cluster system, the energy damped yield of

the fragments were found to be due to orbiting process [40, 86]. However, the observed orbiting-like cross sections of the fragments with ( $6 \leq Z \leq 8$ ) emitted in the reaction  $^{28}\text{Si} + ^{14}\text{N}$  [40, 86] are much smaller than those for the  $^{28}\text{Si} + ^{12}\text{C}$  reaction. NOCs of  $^{12}\text{C} + ^{28}\text{Si}$  have also been compared with the same for the neighboring non  $\alpha$ -cluster systems viz.  $A = 39$ , i.e.,  $^{11}\text{B} + ^{28}\text{Si}$  and  $^{12}\text{C} + ^{27}\text{Al}$  and plotted in the same figure. It is seen from Fig. 5.1(b) that the NOCs for the system  $^{11}\text{B} + ^{28}\text{Si}$  and  $^{12}\text{C} + ^{27}\text{Al}$  are nearly the same and much higher than those for the  $^{12}\text{C} + ^{28}\text{Si}$  system at all the grazing angular momentum. The large NOC values for  $^{11}\text{B}$  (64 MeV) +  $^{28}\text{Si}$  and  $^{12}\text{C}$  (73 MeV) +  $^{27}\text{Al}$  and the absence of entrance channel dependence are in consistent with the fact that FF is dominant for the energy damped yield of the fragments emitted from the non- $\alpha$  cluster system  $^{39}\text{K}$ . However, the absence of any significant enhancement in light fragment ( $3 \leq Z \leq 5$ ) yield in the case of  $^{12}\text{C}$  (77 MeV) +  $^{28}\text{Si}$  system as expected from NOC results (and also previously seen for  $6 \leq Z \leq 8$  fragments), needs to be properly understood.

### 5.1.2 Secondary decay of heavier fragments emitted in $^{16}\text{O} + ^{12}\text{C}$

The primary fragments, emitted in the binary reaction,  $^{16}\text{O} + ^{12}\text{C}$ , may have sufficient energy for further decay by emitting lighter fragments, particles and  $\gamma$ -rays. The yield of these secondary fragments may also contribute to the fragment spectra. To check these, detailed simulations of secondary decay have been performed using the Monte Carlo binary decay version of the statistical decay code LILITA [8] as described in Refs.[70, 73]. Secondary decays of different primary binary channels viz.,  $\text{O}^*$  (binary channels  $^{15,16,17}\text{O} + ^{13,12,11}\text{C}$ ),  $\text{F}^*$  (binary channels  $^{17,18,19}\text{F} + ^{11,10,9}\text{B}$ ),  $\text{Ne}^*$  (binary channels  $^{20,21}\text{Ne} + ^{8,7}\text{Be}$ ),  $\text{Na}^*$  (binary channels  $^{21,22}\text{Na} + ^{7,6}\text{Li}$ ), and  $\text{Mg}^*$  (binary channels  $^{24,25}\text{Mg} + ^{4,3}\text{He}$ ) respectively, have been studied at the highest excitation energy for the present bombarding energies. It has been observed that secondary decays of  $\text{Mg}^*$ ,  $\text{Na}^*$ , and  $\text{Ne}^*$  do not reach up to B. However, a significant yield of the fragment B arises due to the the secondary decay of the primary fragments  $^{19}\text{F}^*$  ( $\sim 49\%$ ),  $^{16}\text{O}^*$  ( $\sim 48\%$ ) and

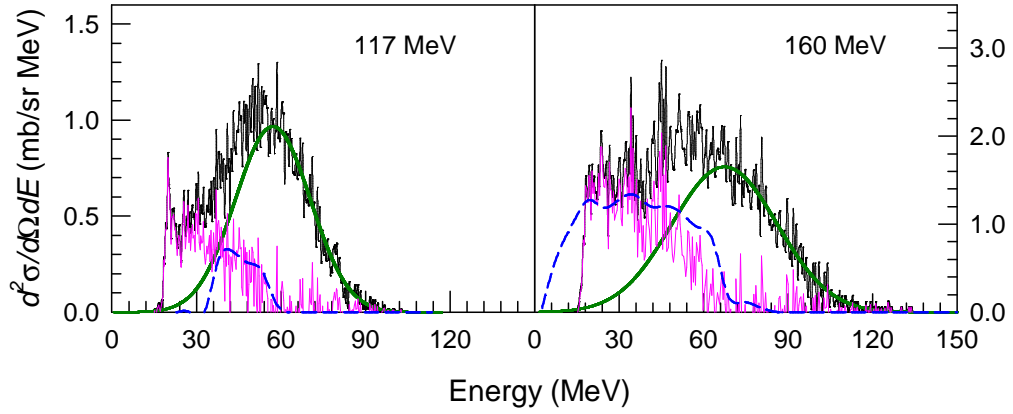


**Figure 5.2:** Secondary decay contribution to B fragment estimated from LILITA at energies 117 and 160 MeV, respectively. The energy distribution of B at these energies at  $\theta_{lab}=15^\circ$  are shown along with fitted Gaussians. In the same graph, the difference spectra (Gaussian subtracted from total spectra) is shown by pink curve and blue dashed curve represents the total secondary decay contribution estimated using LILITA.

$^{15}\text{O}$  ( $\sim 0.4\%$ ). The simulations of the energy distributions of the secondary decay of B from  $^{19}\text{F}^*$ ,  $^{16}\text{O}^*$  and  $^{15}\text{O}^*$  have been done using the code LILITA and are found to peak at much lower energies  $\sim 32\text{-}39$  MeV as shown in Fig. 5.2, typically, for  $E_{lab} = 117$  and 160 MeV.

It has been observed that the energy distributions of the secondary decay components are very different from those of the primary fragment components as shown in Fig. 5.2. However, the contributions of this secondary decay have been eliminated by the Gaussian fitting procedure for the extraction of primary B yields. First, the width of Gaussian is determined by fitting the higher energy tail of the spectrum with a Gaussian having its centroid around energies obtained from Viola systematics. In the next step, the total energy spectrum is fitted with a Gaussian to extract the primary fragment component as shown in Fig. 5.2. It is seen that there is a significant enhancement in yield at lower energy part of the spectra which increases with bombarding energy (Fig. 3.1). The difference spectra are obtained by subtracting the fitted Gaussian from the corresponding experimental spectra as shown by solid pink color in Fig. 5.2. It has been found that the difference spectra obtained at 160 MeV are well reproduced

by the secondary decay distributions (blue dashed line) obtained from LILITA. However, the lower energy tail of the difference spectra obtained at 117 MeV is not fully explained by the secondary decay distributions, which may be due to other additional sources. It is thus evident that the Gaussian fitting procedure for the extraction of primary fragment yield is sufficient to reject the contributions of the secondary decay components, if any, as their energy distributions are different from those of primary fragments [70, 73].

### 5.1.3 Deformation in $^{28}\text{Si}^*$

The deformation of the produced composite,  $^{28}\text{Si}^*$ , has been extracted using charged particle spectroscopy as discussed in Chapter 3. Here, the energy spectrum of the  $\alpha$ -particle could not be reproduced by CASCADE calculation with ‘deformability parameters’ obtained by RLDM [113]. To explain the experimental spectra, the deformability parameters have been optimized. Quadrupole deformation,  $\beta$ , of  $^{28}\text{Si}^*$  has been extracted for both the RLDM deformability parameters and optimized values of deformability parameters as shown in Table 3.2. It is observed that the deformation (see the values of  $\beta_{\ell av}^B$  in Table 3.3) is required to explain the energy spectra of  $\alpha$ -particles is larger than the RLDM deformation ( $\beta_{\ell av}^A$ ), at all beam energies, and the deformation is found to increase with spin of the excited composite. The observed deformation in the present study may thus be considered as another indication of orbiting in  $^{16}\text{O} + ^{12}\text{C}$ .

Though the present formalism of angular momentum dependent level density is largely successful in explaining experimental light charged particle (LCP) spectra, the magnitude of enhancement required is quite large and lacks proper explanation [124, 125]. So, an alternative approach, based on frozen degrees of freedom has been proposed, which has earlier been shown to reproduce the data quite well [126, 127]. In this approach, it is assumed that the deformation of the compound nucleus is frozen during the decay, i.e., there is no change of shape of the nascent final nucleus; so the

phase space is calculated using RLDM deformation of the parent nucleus, rather than that of the usual daughter nucleus. This indicates that the dynamical effects like shape relaxation should be taken into account to properly understand the phenomenon of particle evaporation from a deformed compound nucleus.

The formalism of ‘frozen deformation’ has been applied in the present CASCADE calculation. In the case of  $\alpha$ -particle emission, the effect of frozen deformation on the energy spectrum may be taken into account in the following way. As the  $\alpha$ -particles are emitted predominantly at the initial stage of the decay cascade, the deformation may

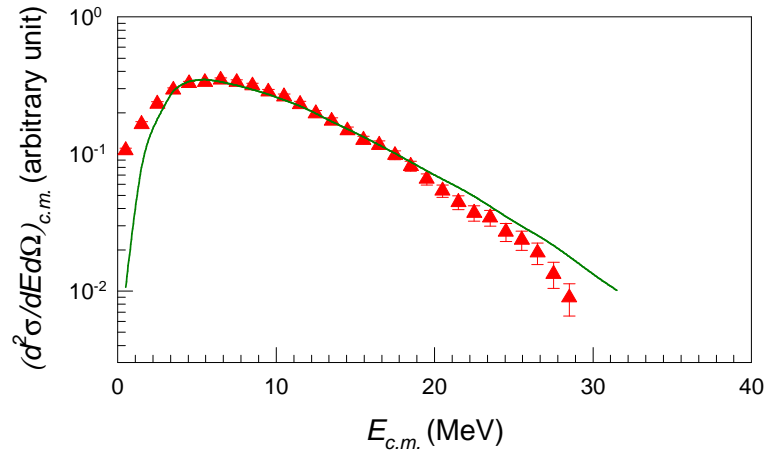


**Figure 5.3:** Comparison of the experimental energy spectra (c.m.) of  $\alpha$ -particles (red triangles) with the same obtained by theoretical calculations for beam energy 160 MeV. Green solid line represent the CASCADE calculations done using ‘frozen’ deformation ( $I_{eff}/I_0$ ) obtained using RLDM deformability parameters for  $\ell = 23\hbar$ .

be ‘frozen’ at its value corresponding to the highest angular momentum that the compound nucleus may have, which is  $\approx \ell_{cr}$ . So, in the present CASCADE calculation, the deformation has been kept fixed throughout by freezing the value of  $\mathcal{I}_{eff}/\mathcal{I}_0$ , the ratio of effective moments of inertia of the deformed composite and the rigid body rotation, which has been calculated using a fixed value of  $\ell \approx \ell_{cr}$  using Eq. 3.11 with  $\delta_1$  and  $\delta_2$  obtained from RLDM (See Table 3.2). The results of the CASCADE calculations with ‘frozen’ deformation and the normal CASCADE prediction with optimized values of deformability parameters have been shown in Fig. 5.3 with the experimental data. It is

observed that, the CASCADE prediction with ‘frozen’ deformation for  $\ell = \ell_{cr} = 23\hbar$  (green dashed curve) nearly matches with the experimental data. The corresponding ‘frozen’ deformation,  $\beta_{froz}$  (calculated for  $\ell_{cr} = 23\hbar$ ) is 0.68. So, it is evident that the ‘frozen’ deformation picture [126, 127], is also equally effective in the explaining the  $\alpha$ -spectra. However it is interesting to note that both the picture (CASCADE calculation with ‘frozen’ deformation and with optimized values of deformability parameters) predict substantial deformation of the composite.

It should however be mentioned here that the ‘frozen deformation’ formalism followed in the present calculation is too simplistic. To get actual deformation using this approach one needs to perform detailed event-by-event Monte Carlo calculations which take into account the initial compound nucleus deformation (depending on the CN spin) and its ‘freezing’ in the consecutive steps of decay. The results are likely to be sensitive to the initial spin distribution. From the above discussion, it may be said that, though the present study shows deformation of the excited composite which is higher than the corresponding RLDM value, uncertainty still remains about the actual magnitude of deformation. This limitation of the present study notwithstanding, there is, at least qualitative, indication about some enhanced deformation, which may be linked with orbiting as one of the contributing factors.

## 5.2 Angular momentum dissipation in DI collision

It has been observed (Chapter 4) that the kinetic energy spectra of the fragments (Li, Be and B) emitted in the reactions  $^{12}\text{C} + ^{28}\text{Si}$ ,  $^{12}\text{C} + ^{27}\text{Al}$  and  $^{11}\text{B} + ^{28}\text{Si}$  (typical spectra shown in Fig. 4.1) have two peaks. The angular distribution and the agreement between the experimental angle integrated yields extracted from the first peak with those predicted by standard statistical model confirmed the compound nuclear origin of the first peak. On the other hand, the faster fall off of the fragment angular distribution extracted from the second peak and  $Q$ -value distributions indicated that this

peak is due to DI collision. To understand the variation of the mean kinetic energies of the fragments as well as the energy damping mechanism in general, it is important to study the angular momentum dissipation in DI collision. For heavy systems, angular momentum dissipation is experimentally estimated using the  $\alpha$ -particle angular distribution and the  $\gamma$ -ray multiplicity data and it is known that the rigid rotation limit is usually reached in these systems [67]. For light systems, the angular momentum transfer is generally estimated from the total kinetic energy of the rotating di-nuclear system,  $E_k$ , which is given by,

$$E_k = V_N(d) + f^2 \frac{\hbar^2 \ell_i (\ell_i + 1)}{2\mu d^2}, \quad (5.1)$$

where  $V_N(d)$  is the contribution from Coulomb and nuclear forces at di-nuclear separation distance  $d$ ,  $\mu$  is the reduced mass of the di-nuclear configuration,  $\ell_i$  is the relative angular momentum in the entrance channel and  $f$  (final angular momentum =  $f\ell_i$ ) is the numerical factor denoting the fraction of the angular momentum transferred. For the light systems, like  $^{20}\text{Ne} + ^{12}\text{C}$  [32], there have been indications of large dissipation of relative angular momentum in excess of the sticking limit predictions, which might be partly due to the ambiguity in the determination of the magnitude of angular momentum dissipation, as both  $d$  and  $f$  are unknown quantities [76]. To remove this ambiguity, a simple prescription for estimating both  $f$  and  $d$  was described in Ref. [76], where it has been shown that the fraction of angular momentum transfer for fully energy-damped DI collision of a few light systems is close to the corresponding rigid rotation limit (sticking limit). To see whether this trend is valid in general for DI collisions of light systems, angular momentum dissipation factor,  $f$ , for each exit channel mass asymmetry has been extracted for all the reactions. It is seen that, for the present systems, at angle  $\theta_{c.m.} \gtrsim 40^\circ$ ,  $\langle Q_{DI} \rangle$  becomes nearly constant which implies that energy dissipation is completed. It is known that DI process occurs in the angular momentum window  $\ell_{cr} < \ell < \ell_{gr}$ . In peripheral collisions,  $\ell \sim \ell_{gr}$ , overlap between two the systems is small and so, the energy dissipation is minimum. On the other hand, for  $\ell \sim \ell_{cr}$ , energy dissipation is likely to be highest [corresponds to the yield at  $\theta_{c.m.} \gtrsim 40^\circ$ ]. It may be noted here that the FF yield is also most predominant near

$\ell \sim \ell_{cr}$ . Hence, it is expected that the exit channel configuration will be nearly same in fully energy damped DI and in FF processes. In the present calculation, the separation distance  $d$  between the two fragments has been estimated from the scission point

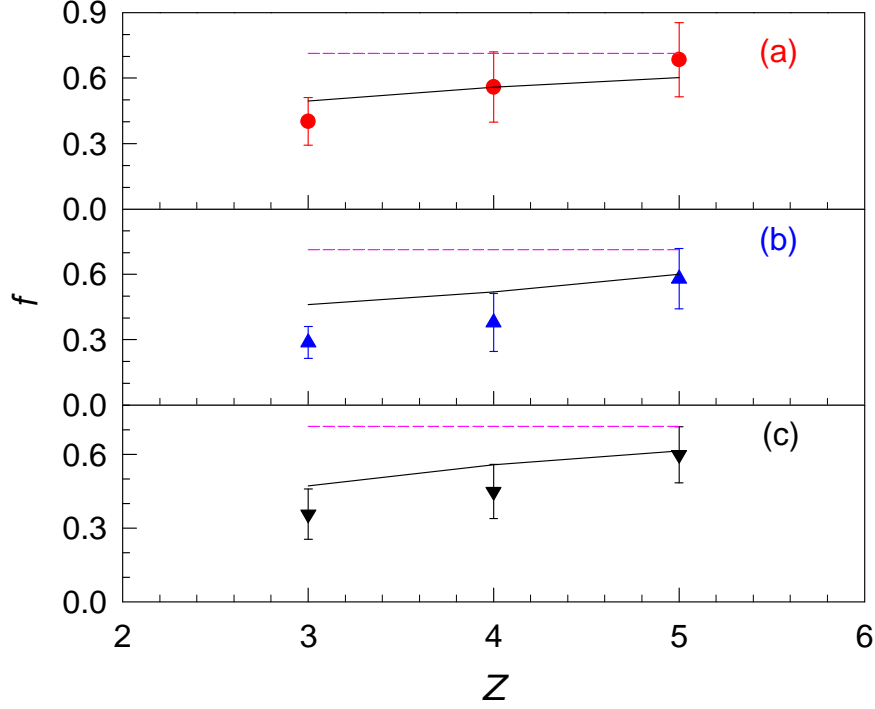


**Figure 5.4:** The variation of angular momentum dissipation factor  $f$  with atomic number of the fragments. The solid circles (red), solid triangles (blue), and inverted triangles (black) are the extracted values of  $f$  for (a)  $^{11}\text{B} + ^{28}\text{Si}$ , (b)  $^{12}\text{C} + ^{27}\text{Al}$ , and (c)  $^{12}\text{C} + ^{28}\text{Si}$  reactions, respectively. The solid (black) and dotted (pink) curves correspond to the sticking limit and the rolling limit predictions for the same, respectively.

configuration corresponding to the respective asymmetric mass splitting [44], and the corresponding value of kinetic energy is taken as  $V_N(d)$ . The value of initial angular momentum  $\ell_i$  has been taken to be equal to the critical angular momentum for fusion,  $\ell_{cr}$ . The angular momentum dissipation factors thus obtained have been displayed in Fig. 5.4 and it is observed that for all three reactions considered, the experimental values of the mean angular momentum dissipation are more than those predicted under the rolling condition; however, the corresponding sticking limit predictions of  $f$  are in fair agreement with the experimental values of the same within the error bar. In all

cases, the discrepancy is more for the lighter fragments, and it gradually decreases for the heavier fragments. This may be explained in terms of the following qualitative argument. Microscopically, friction is generated due to stochastic exchange of nucleons between the reacting partners through the window formed by the overlap of the density distributions of the two. Stronger friction essentially means larger degree of density overlap and more nucleon exchange. The lighter DI fragment (corresponds to more net nucleon transfer) originates from deeper collision, for which the interaction time is also larger as seen in Fig. 4.7. Therefore, the angular momentum dissipation, originating due to the stochastic nucleon exchange, should also be more, which, at least qualitatively, explains the observed trend.

## Chapter 6

# Development a of high vacuum reaction chamber

Vacuum reaction chamber is an essential component of any accelerator based experimental setup in nuclear physics. The design of the chamber depends upon the experimental programme. It may either be a very specialized chamber for dedicated experimental setup e.g, CHIMERA [128], LASSA [129], INDRA [130] as shown in Figs. 6.1(a), 6.1(b), 6.1(c), respectively or it may be a versatile general purpose reaction chamber [Figs. 2.4(a): VECC, Kolkata , 6.1(d): Ciclope [131], LNS, Italy, 6.1(e) :ASCHRA [132], RIKEN, Japan]. CHIMERA, LASSA, and INDRA reaction chambers are dedicated to house the corresponding large complex detector system where the sizes of the chambers are different depending upon the detector system. The size of a general purpose reaction chamber may also vary. For charged particle detector based experiments, chambers are usually big in size (VECC, Ciclope, ASCHRA chamber) to accommodate all detectors within the chamber at a reasonable distance. The VECC chamber have diameter of 91 cm and height 50 cm, Ciclope is of diameter of 2 meter and length 4 meter, ASCHRA have diameter of 2.95 meter and length 4.8 meter. On the other hand, for the  $\gamma$ -ray / neutron based experiments, chamber may be small in size as all the detectors are kept outside the chamber. The chamber used in Indian Na-

tional Gamma Array (INGA) [133] setup at VECC belongs to this category as shown in Fig. 6.1(f). This chamber have diameter  $\sim 15$  cm and height  $\sim 8.5$ cm.



**Figure 6.1:** Different types of reaction chambers used at different laboratory all over the world.

A superconducting cyclotron (SCC) has been constructed at VECC which will deliver beam in the energy range  $10 \leq E \leq 60$  MeV/A for projectile of mass number  $A < 100$  and  $5 \leq E \leq 20$  MeV/A for  $A \sim 200$ . Fig. 6.2 shows the schematic diagram of the cyclotron with the beam line layout. The beam line-I will be used for high current (irradiation) experiments as well as general nuclear physics experiments with charged particle detectors at low beam current. Beam line-II is dedicated for the experiment with neutron detectors and  $\gamma$  detectors. The beam line-III will be reserved for a superconducting solenoid spectrometer and the beam line-IV is dedicated for the experiments on the material science. The SCC is likely to open up new areas of experimental nuclear physics research in intermediate energy and vigorous activities are on to develop new, state-of-the-art experimental setups to facilitate high quality research [134]. The present chamber is multipurpose reaction chamber which will cater to the

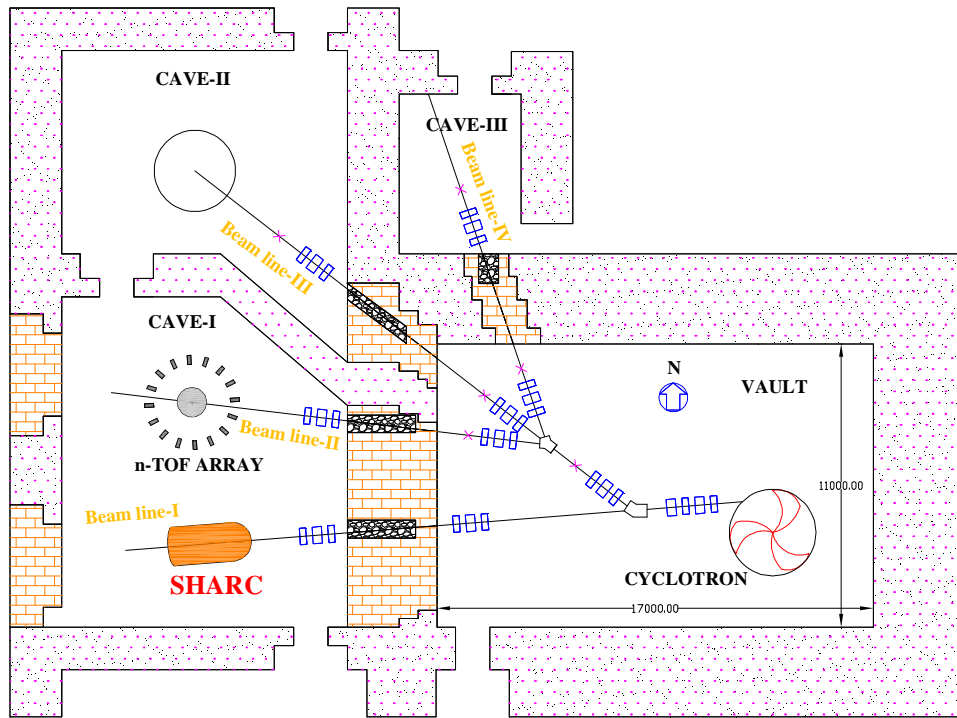


**Figure 6.2:** Schematic diagram of K500 cyclotron beam lines with three beam hall. SHARC has been installed in beam line-I.

needs of different types of experiments using these experimental facilities as well as other detector systems. One of these experimental facilities is the  $4\pi$ -Charged Particle Detector Array (CPDA) which is being built for the study of IMF emission in the Fermi energy domain. The chamber can accommodate CPDA inside it, along with other ancillary detectors like large area gas detector etc. This chamber is a segmented, horizontal axis, reaction chamber (SHARC) which has been designed, fabricated and installed in the SSC beam Cave-I (Fig. 6.2). Here, in the present chapter, the development of SHARC will be discussed.

## 6.1 Basic design parameters

SHARC has been designed as the primary facility to be used for experiments in SCC beam line-I. The dimensions of SHARC have been optimized to have maximum

flexibility for versatile experimental setups as well as to house the whole CPDA. Optimum shape has been decided to be cylindrical with its axis coinciding with the beam axis to avail maximum possible flight path for 'time of flight' measurements. Long cylindrical shape also served the purpose of getting a better angular resolution required in the forward hemisphere because of strong focusing at forward angles at high beam velocities. Other salient design considerations are,

- i. The chamber should be suitably segmented for easy access inside it. Each segment should have independent movement arrangement.
- ii. Vacuum control system should have maximum flexibility. The vacuum system should have both auto and manual modes of operation with dynamic display of complete status. There should be facility for remote monitoring of vacuum status with emergency shutdown option.
- iii. Target ladder should have the provision to be placed at any position inside the chamber along the beam axis to optimize the flight path. The vertical and rotational movements of the ladder have to be controlled and monitored in auto / manual mode, both from local as well as remote station.
- iv. Both vertical position and rotational angle of the ladder should be accurately measured.
- v. The chamber will have a Faraday cup of sufficiently large aperture to stop the beam and measure the beam current.
- vi. Arrangement to see the position of the target and beam spot on the target during the experiment.
- vii. Minimum arrangement to put detectors inside the chamber.
- viii. Proper vacuum feed-through to bring the detectors signals, detectors bias inputs, and other electrical connections outside the chamber.

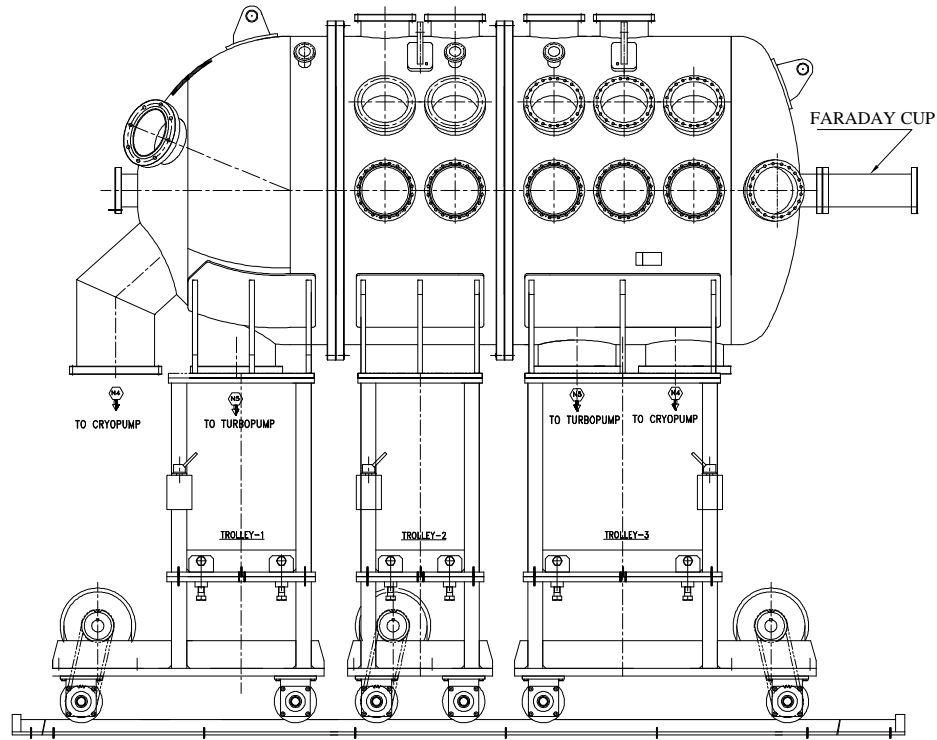


*Figure 6.3: Schematic diagram of SHARC without vacuum pumping system.*

## 6.2 Details of SHARC

A schematic diagram of SHARC and the photograph of the chamber installed in its present position (SCC cave-I) are shown in Figs. 6.3 and 6.4, respectively.

### 6.2.1 Mechanical details

SHARC is a cylindrical, three segments, stainless steel (SS 304L) chamber of length 2.2 meter, diameter 1 meter and total volume including the pipes to connect the pumps is  $\sim 1800$  litres and wall thickness  $\sim 10$  mm. The front (beam-entry) end is hemispherical in shape of radius 500 mm and the rear end is elliptical dish (2:1) shaped. All three segments are mounted on separate support structures which rest on external rails such that each segment can move independently on the rails by automatic gear-motor control mechanism having built-in limit switch locking facility with

manual override option. All three segments (the rear part in particular) may be rolled back on rail to open up the chamber to give accessibility for the installation of users' equipments inside. There is arrangement to manually align the chamber with the beam line axis precisely in horizontal/ vertical/ rotational degrees of freedom. Two pairs of

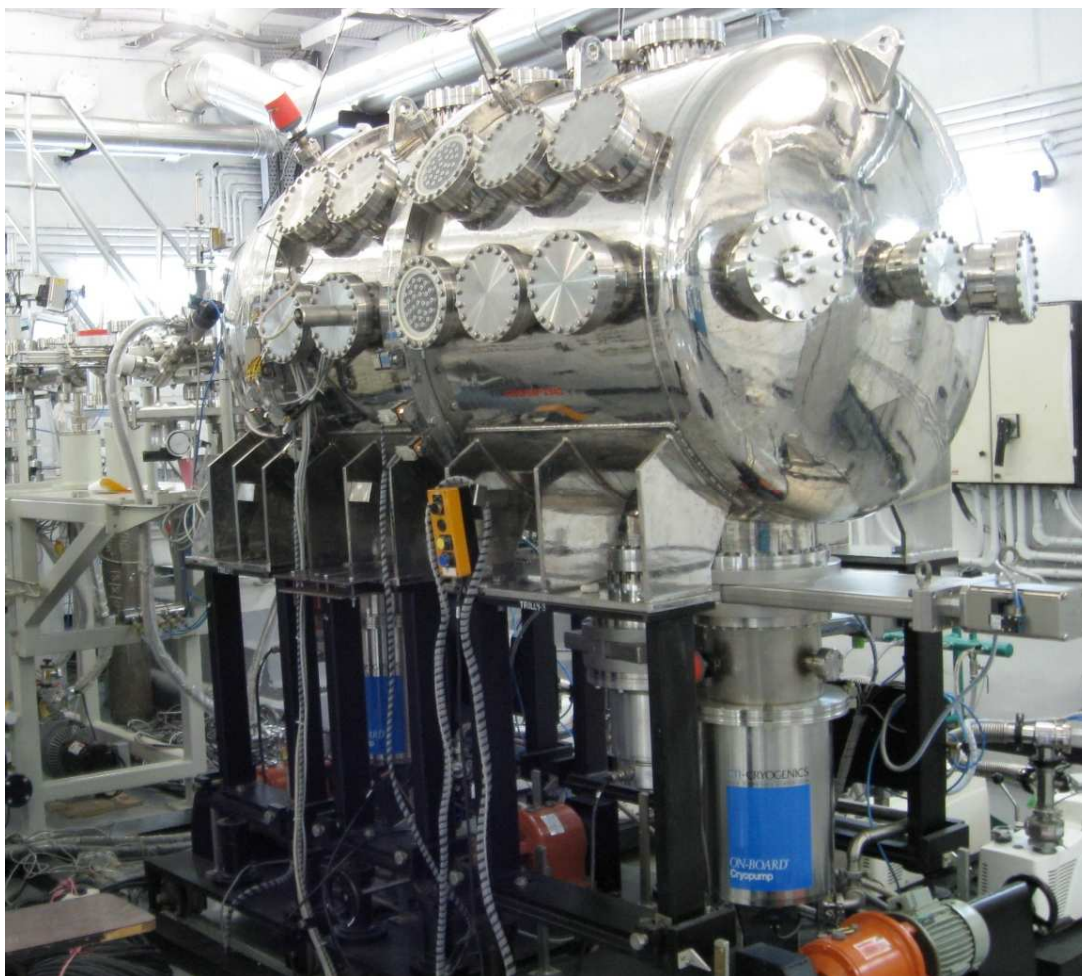


*Figure 6.4: SHARC installed in SCC Cave-I.*

rails are provided within the chamber for mounting and placement of the target ladder system and the user designed detector assemblies at any position within the chamber. A generalized detector mounting table (made of Aluminum alloy 6061-T6) with precision alignment mechanism on manually movable stands with locking arrangement on rails is also provided as default arrangement. All over this table, there are inverted

‘T’-shaped channels which may be used for detector mounting in a general experiment. There is provision to adjust the height of the table as per requirement of the experimental setup. The table can be easily removed from the chamber if the rails are sufficient to mount the detector system. To achieve optimum vacuum performance, all inside surfaces were given smooth granular finish and were finally electro-polished with bright finish.

### 6.2.2 Target ladder assembly

One of the important parts of a reaction chamber is target ladder. As per the requirement of an experiment, the target foil may be placed at different position of the reaction chamber along the beam direction. The present target ladder system has been suitably designed to take the maximum advantage of the full length of the chamber.

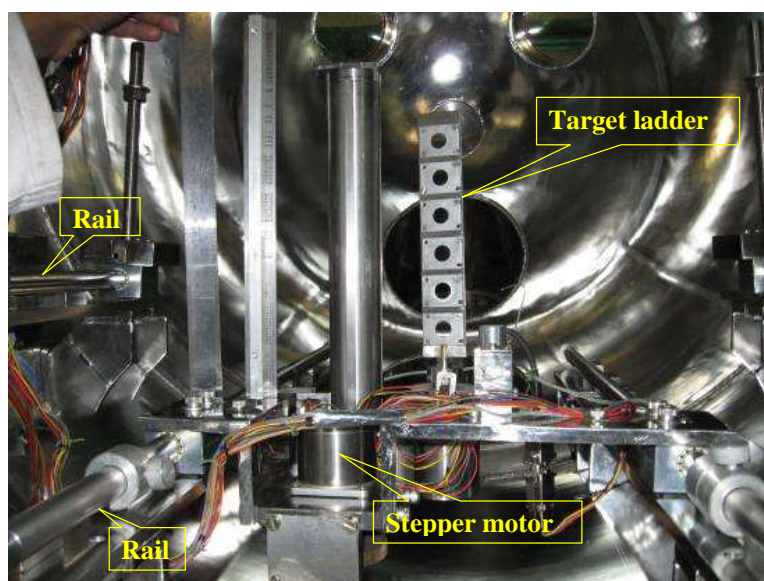


*Figure 6.5: SHARC target assembly.*

The whole assembly is mounted on one pair of internal rails and may be placed at any position along the beam axis within the chamber to optimize the flight path. Another important requirement in the target ladder system is that, one may require to use

many targets in a single experiment. The provision of vertical movement of the whole target ladder is essential for this purpose. The target assembly includes a ladder that can hold six targets at a time in a column (see Fig. 6.5). Generally, the target foil is placed in a plane perpendicular to the beam direction; however, it may also be required to rotate the target at different angular position with respect to beam direction. The present target ladder can be rotated up to maximum angle  $360^{\circ}$  (both clockwise and anti-clockwise) with angular precision of  $0.1^{\circ}$  and can be moved vertically up to 25 cm with accuracy of 0.1 mm with the help of two vacuum compatible stepper motors (Make: M/s. Sanyo Denki, Type 103-770-12V1). These motors are operated by Programmable Logic Controller (PLC) both remotely or locally. Target ladder movements (rotational and vertical) are enabled by giving specific command (to move to a particular distance / rotate through a particular angle) through PLC. Two encoders (one linear, one circular) are needed to measure the actual position / angle of the target ladder. Two glass windows are kept to visually inspect the positions of the target and the detector inside and also to see the beam spot at the target position (on alumina, during optimisation of beam transport) using a camera outside the chamber. It is also planned to fix a web camera inside the chamber in future for on-line monitoring.

### **6.2.3 Input / Output ports**

SHARC has been provided with 24 ports (each of diameter 25 cm) on different locations of the body of chamber (see Fig. 6.3 and Fig. 6.4) to cater to various experimental requirements, like, the connections of gas flow system, electrical signals from the detectors, bias inputs of detectors, cooling pipes (if required) etc. Flanges with standard LEMO connectors as well as indigenously designed and fabricated flanges with Flat Ribbon Connector (FRC) connectors has been used as electrical feed-through to take the detector signals. To prepare the vacuum feed-through with FRC, we have used aluminium flange, 8 mm thick printed circuit board (PCB), FRC connector and casting material Araldite and Epotec H77. The design of the flange and PCB is shown

in Fig. 6.6(a). The aluminium flange has been prepared with a step cut to put the PCB. As per design of the FRC, holes have been drilled on the PCB with accuracy  $\sim 0.05$  mm using Computer Numerical Control (CNC) milling. On each PCB, provision to keep multiple FRC (10-12 no) has been made, depending upon the space and connector dimension. Fabrication of the vacuum feedthrough was carried out in following steps: First, flange and PCB was cleaned with water and soap. Then they were dried with a blower and again washed with acetone and kept in an oven at  $150^{\circ}\text{C}$  for 15 minutes. PCB was glued with the flange using Araldite and were kept 24 hours at room temperature. Then the flange was heated to  $150^{\circ}\text{C}$  again for 15 minutes after fixing the FRCs in the holes on the PCB. The flange was taken out in very hot condition and the epoxy Epotek H77 was poured on it very slowly in one side so as to form an uniform thin layer. Then the flange was kept inside the oven at temperature  $150^{\circ}\text{C}$  for  $\sim 2$  hours, till the color of H77 changes from white to golden [see Fig. 6.6(b)]. Finally, the flange was taken out and same process was repeated for the other side of the flange. After 2 hours, oven was switched off and flange was cooled down slowly inside the chamber.

#### **6.2.4 Vacuum pumping system**

The design of the pumping system mainly depends on the volume of the chamber which will be pumped, the ultimate vacuum, and, the specified time to reach the ultimate vacuum. For high vacuum system, degassing from the inner surface of the chamber and instruments kept inside it is the one of the most important factors to be considered. The design target was to achieve a clean a vacuum  $\sim 10^{-7}$  mbar in SHARC with volume  $\sim 1800$  litres (l) in 8 hours (h); we have done an approximate calculation of pumping speed. The pumpdown calculation was done for two stages, (a) pumping speed required to pump SHARC from atmospheric pressure ( $\sim 1000$  mbar) to rough vacuum ( $\sim 10^{-1} - 10^{-2}$  mbar) in 1h and then (b) rough vacuum to very high vacuum ( $\sim 10^{-6} - 10^{-9}$ ) mbar in 7h. So, the total pumpdown time will be the total time to achieve (a) rough vacuum and (b) high vacuum. To maintain the required pressure at

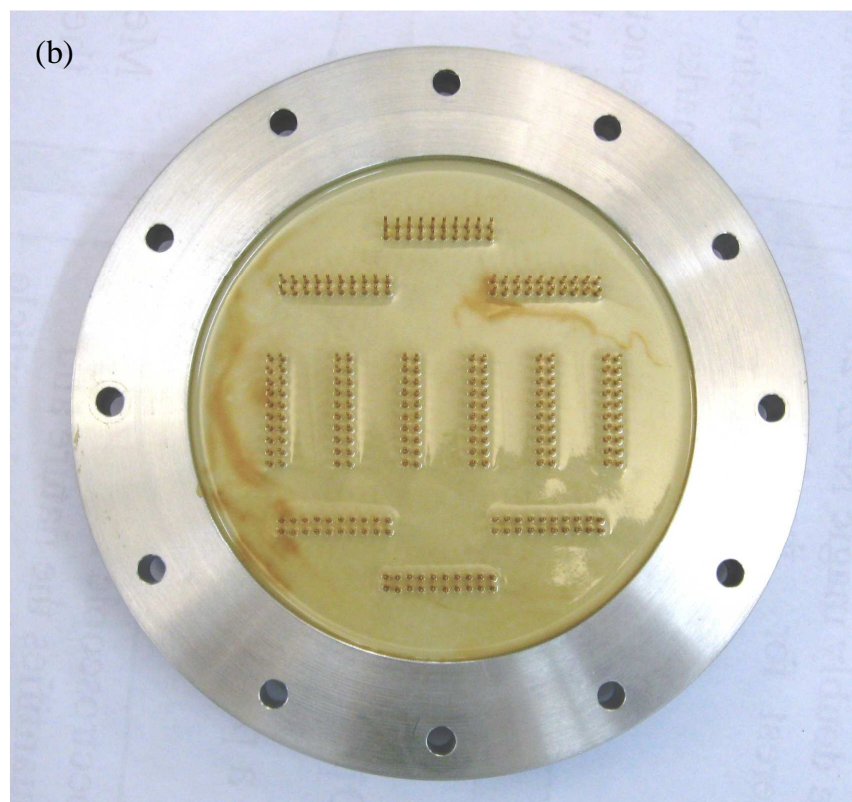
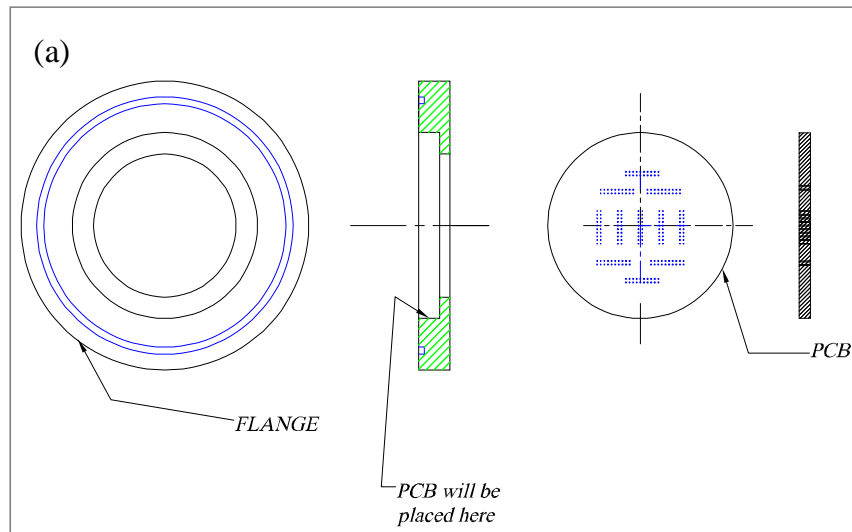


**Figure 6.6:** (a) Design of different component of FRC vacuum feed through. Holes in the PCB are kept to place FRC. (b) The flange after final casting.

high vacuum, one has to consider gas load due to factors like outgassing.

**(a) Pumping speed to evacuate up to pressure 0.05 mbar in 1h:** The pumping speed can be estimated using the following expression,

$$S = V/T \times \ln(P_1/P_2) \times K \quad (6.1)$$

where  $V$  is the volume of the vessel to be pumped,  $T$  is the time to pump down the vessel from initial pressure  $P_1$  to final pressure  $P_2$  with a pumping speed  $S$  assuming degassing factor  $K$ . So, assuming  $K = 1.5$ , required pumping speed to pump down 1800 l volume of SHARC from atmospheric pressure  $\sim 1000$  mbar to 0.05 mbar in one hour is  $\sim 500$  l/min. We have decided to use scroll pump (Adixen ACP 40) to achieve this rough vacuum which have a peak pumping speed  $37 \text{ m}^3/\text{h}$  ( $616 \text{ l}/\text{min}$ ). But the

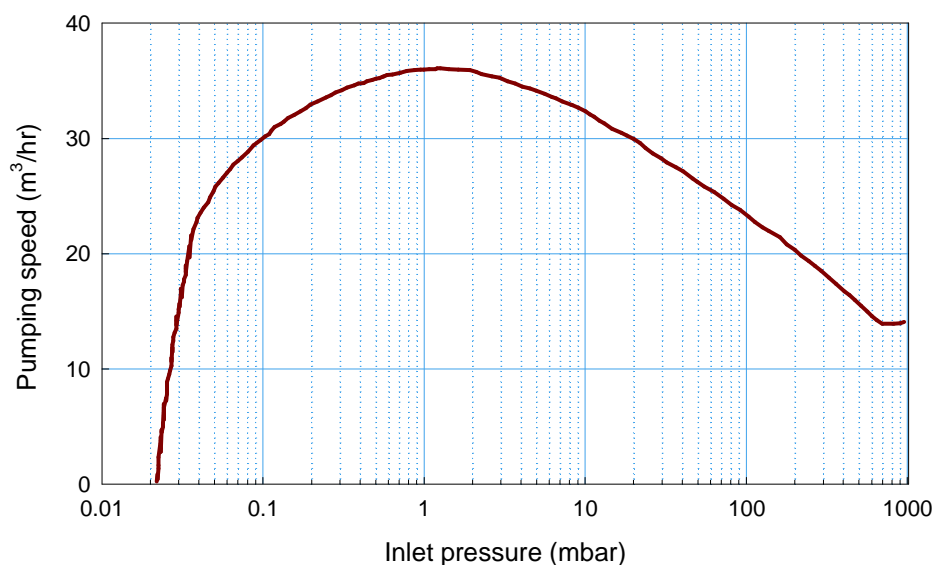


**Figure 6.7:** Variation of pumping speed of the scroll pump with inlet pressure.

pumping speed of scroll pump varies with the pressure of the inlet of the pump as per data sheet (Fig. 6.7). We have calculated the average speed ( $\sum \frac{S \times P}{P}$ ,  $S$  is pumping speed,  $P$  inlet pressure) of individual pump which is found to be is  $17 \text{ m}^3/\text{h}$ . If we assume the speed loss due to conductance is 15%, effective speed of one scroll pump is  $14.5 \text{ m}^3/\text{h}$  ( $240.8 \text{ l}/\text{min}$ ). So, we need two such scroll pump connected in parallel, as shown in Fig. 6.10, to reach 0.05 mbar in  $\sim 1\text{h}$ .

**Table 6.1:** Throughput of the materials used in different parts of SHARC over a period of ~ 6-7h. Throughput is defined as the product of outgassing rate and surface area of the material.

Material	Outgassing rate (mbar-l/s/m <sup>2</sup> )	Area (m <sup>2</sup> )	Throughput (mbar l/s)
SS	$2.3 \times 10^{-5}$	12	$2.8 \times 10^{-4}$
Al(6061-T6)	$5 \times 10^{-5}$	1.4	$7.0 \times 10^{-5}$
Viton 'O' Ring	$2 \times 10^{-5}$	0.6	$1.2 \times 10^{-5}$
Cu Gasket	$5 \times 10^{-6}$	0.3	$1.5 \times 10^{-7}$
			Overall throughput
			$3.6215 \times 10^{-4}$

**(b) Pumping speed to evacuate the chamber from 0.05 to  $\sim 10^{-7}$  mbar:** In this range of vacuum, the Eq. 6.1 is not applicable. This range of vacuum is in molecular region where pumping time entirely depends on outgassing from the different material inside the chamber. The outgassing rates depend on various factors, like, the type of material, temperature, time for which a material is baked (if any), pressure of the vessel, how long it was kept at which pressure etc, which makes it difficult to estimate the actual outgassing. Hence, after the estimation of approximate outgassing, it is checked whether the pumping speed of high vacuum pump is more than the outgassing rate to achieve ultimate vacuum  $\sim 10^{-7}$  mbar.

In Table 6.1, throughputs (outgassing rate  $\times$  surface area) of the materials used in different parts of SHARC, over a period of ~ 6-7h, have been given approximately. So, the minimum pumping speed required to achieve ultimate vacuum  $\sim 10^{-7}$  mbar (from rough vacuum) in ~ 6-7h with total throughput  $3.6215 \times 10^{-4}$  mbar l/s is 3621.5 l/s (total through put/ultimate vacuum)  $\approx 3700$  l/s. We have decided to use two turbo pumps (Varian 1001 Navigator, Model No. 9698947) each with speed 1000 l/s and two cryopump (CTI-Cryogenics, Helix Technology Corporation, Model On-Board 10) with pumping speed 2500 l/s each, all are connected in parallel. The total pumping

speed will be 7000 l/s which are more than the calculated pumping speed. This extra pumping speed we have kept to accommodate the throughput of our detector system which is not included in the calculation given in Table 6.1 and also pumping speed loss due to finite conductance of the pumping pipes.

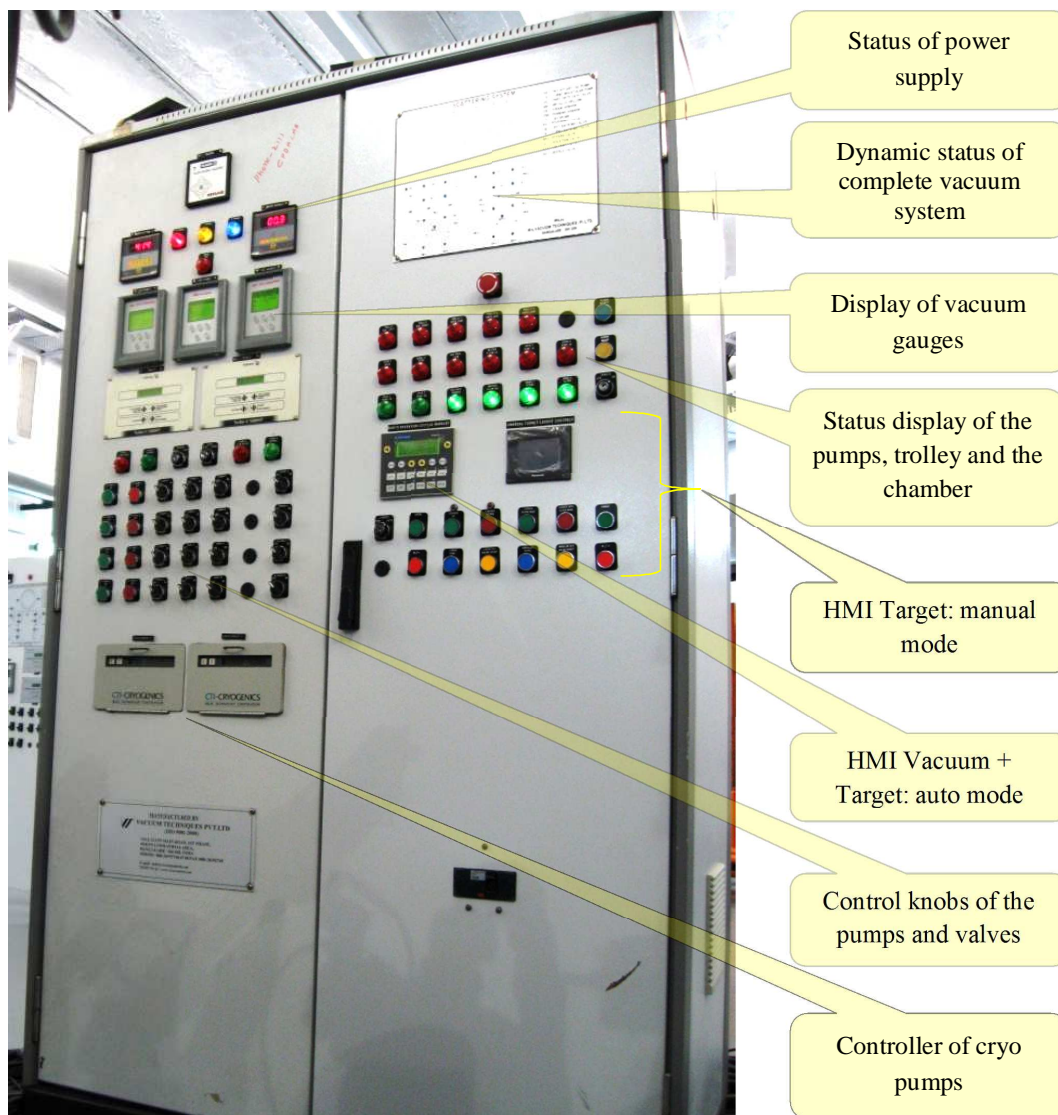


**Figure 6.8:** Local control panel of SHARC. It control both the vacuum system, target ladder and also shows the status all other operations of SHARC.

## 6.3 Operation of the chamber

To operate a particular function of the chamber, one needs to follow certain sequence of steps which is essential to maintain the proper performance of the chamber for a long time in repeated use. For an example, to open a particular section of the chamber, direct use of the corresponding motor on the trolley may severely damage



**Figure 6.9:** Remote control panel of target ladder. It also shows the status all operation of target ladder and pumping system.

the chamber. To open it properly, first the chamber has to bring in atmospheric pressure by letting in dry nitrogen. This is important to get proper vacuum characteristics in the subsequent pump down cycles. Then after opening the nuts and bolts, the corresponding motor can be operated to open the chamber. Similarly, several steps are to be followed in sequence for proper operation of the pumping system and the target ladder assembly. Both the vacuum system and target ladder are controlled by PLC locally as well as remotely through compact control units shown in Fig. 6.8 and Fig. 6.9, respectively. The local control panel of SHARC controls both vacuum system and target ladder operations, and also dynamically displays the status all active parameters of SHARC, like, input power, mechanical interlocks (open or close), pressure of different

of gauges, water supply, status of cryo and turbo pumps, target ladder, valves etc as mentioned in Fig. 6.8. Remote control panel can operate target ladder and also shows the status of its operations and status of the pumping system.

### 6.3.1 Operation of the pumping system

In general, vacuum pumps work properly provided certain conditions are fulfilled. For example, turbo-molecular pump works properly when rough vacuum ( $\sim 10^{-2}$  mbar) is achieved both in its inlet and outlet. At the same time, it cannot be operated if cooling water is not available. Considering the working environment of the pumps used in SHARC (See Fig. 6.10 for details), the whole vacuum operation sequence has been pre-programmed and has been fully automated by using a PLC (Make: M/s. Schneider Electric Modicon). Provision has also been kept to operate the pumps manually. A typical vacuum pumping sequence is displayed in Fig. 6.11 which is controlled by PLC after starting by a single key. Initially all the valves are closed. After switching on the key, rotary pumps (Scroll) RP-1 and RP-2 (Fig. 6.10) are started to pump the pipeline. When the Pirani Gauge PR-1 and PR-3 readings reach  $10^{-2}$  mbar, the rough vacuum valves, RV-1 and RV-2 will be opened to start the rough vacuum pumping of the chamber. When PR-7 and PR-8 show pressures of  $\sim 10^{-2}$  mbar, the turbo pump backing valves (TB-1 and TB-2) are opened and at the same time water to cool the turbo pumps is checked. Then the turbo pumps TP-1 and TP-2 are switched on and within 5 minutes they reach their full speed. At this time, RV-1 and RV-2 are closed and then the high vacuum valve HV-1 and HV-2 are opened. At the same time the backing pumps RP-3 and RP-4 of cryo pumps are started and the valves of the backing pump line CB-1 and CB-2 are opened. Then the temperature of water of the cryo pumps is checked and the pressures of chamber and the cryo pump backing lines are also checked. If the high vacuum (Penning) gauges PNG-1 and PNG-2 show pressure of  $\sim 10^{-6}$  mbar and both PR-5 and PR-6 are  $\sim 10^{-2}$  mbar pressure, then CB-1 and CB-2 are closed and compressors of the cryo pumps are started. When the temperatures of

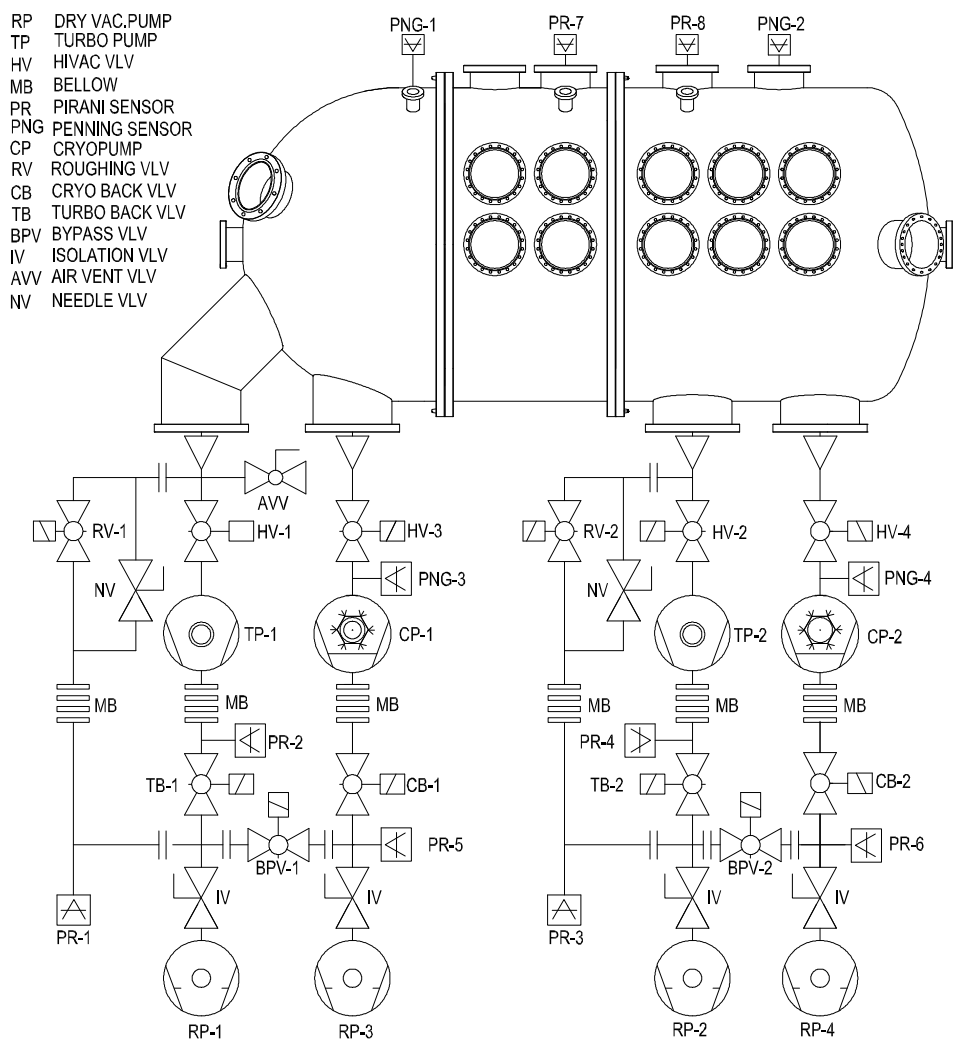


**Figure 6.10:** Schematic diagram of SHARC with vacuum pumping system.

cryo pumps reach below 20K, HV-1 and HV-2 are closed, HV-3 and HV-4 are opened and turbo are pumps switched off. After 10 min, TB-1 and TB-2 are closed RP-1 and RP-2 are switched off and turbo pumps start venting. At this stage the chamber is pumped by cryo pumps only. To achieve a clean vacuum of  $\sim 5 \times 10^{-7}$  mbar, the whole pumping system takes  $\sim 7$ h when SHARC is in empty condition. Alternative options in special situations, such as selection of pumps in case of any failure or in case only rough vacuum is required, are also provided through separate programme packages.

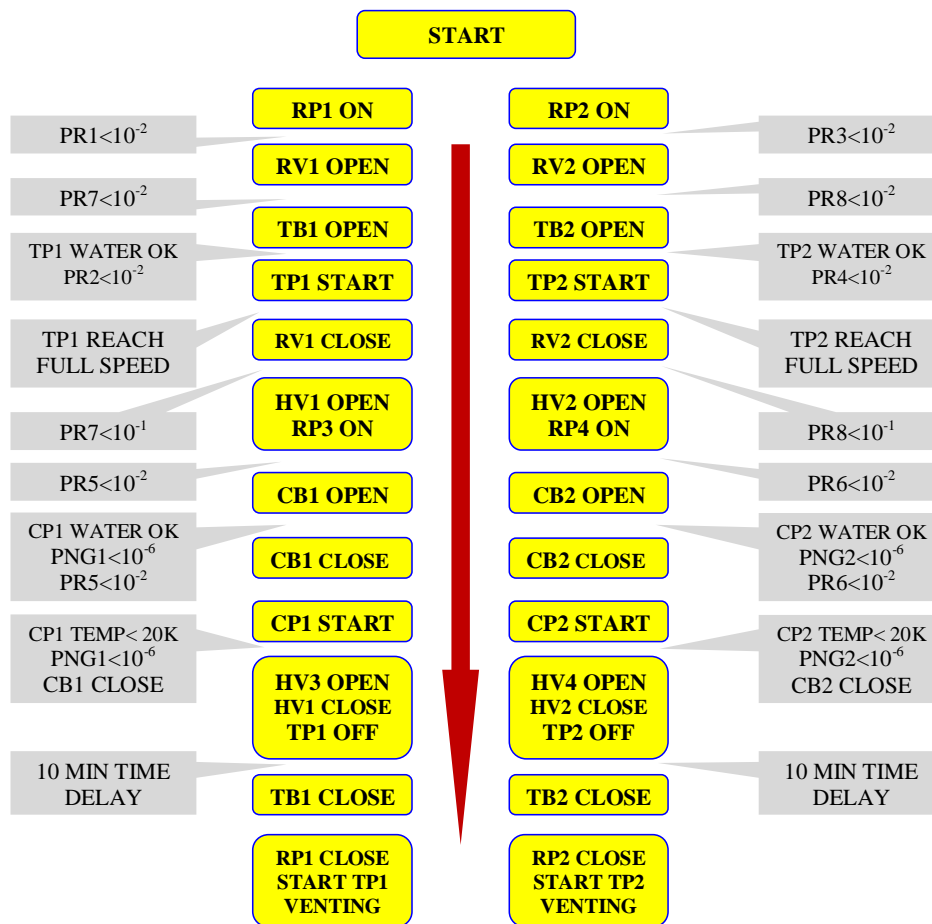


**Figure 6.11:** A typical pumping sequence. Unit of the pressure is in mbar.

Presently, four types of pumping cycle have been stored in PLC, namely, CYCLE-1, 2, 3, and 4. CYCLE-1 is the normal cycle of pumping as discussed above and will be generally used. CYCLE-2 is only for rough vacuum, where turbo and cryo pumps will not be used. CYCLE-3 will be used when any one or two scroll pumps will not work. In case of any failure in cryo pumps, CYCLE-4 is used to bypass it. Any one of these CYCLES can be selected by the Human Machine Interface (HMI) by selecting the corresponding page by pressing side arrows as shown in Fig. 6.12. One may also manually select the failed part and run the vacuum system except that failed part. There is also a provision for slow manual pumping under demanding experimental conditions.

### 6.3.2 Operation of target ladder

The target ladder movement can be operated in two modes, either auto or manual. The same PLC (Make: M/s. Schneider Electric Modicon) used in the operation of pumping system, is also used to control the operation of the target ladder system in auto mode. In this mode of operation, target ladder performed a particular operation as per the specified value given through Human-Machine Interface shown in Fig. 6.12



*Figure 6.12: Human machine interface in auto mode.*

which consists of keys and a display. On the other hand, in the manual mode, target ladder movement is controlled by using jogging of keys and commands through touch screen as shown in Fig. 6.13 and a separate PLC (Make: M/s. Panasonic) is used in this case. Here we shall discuss a few most frequently used operations.

**(a) Auto mode of operation:** Operations of the ladder have been classified into four broad category, (i) Angular value set, (ii) angular speed set, (iii) linear value set, and (iv) linear speed set. Each of these operations has been set in a page which can be selected by the side arrows (left and right) as in Fig. 6.12. Under each of these operations, there are few subcategories, like, SET, ACT, CURR SET etc. By SET,

one can set the value of a particular operation by keys or by pressing the down and up arrows. By button F4, SET value will be added with the actual value (ACT) and it is set as current value of a operation (CURR SET) to be performed. The CURR SET value can also be given directly through the buttons. A particular operation, say, linear value set is explained below. First of all, stepper motors have to be started by buttons F6. By pressing F2 (for angular set F8), ladder will go to 'home' position (minimum value).



**Figure 6.13:** Human machine interface in manual mode. Details of the buttons are given in the text.

Initially we are in 'read' mode. To change the set value of the linear position, we have to go to 'write' mode by pressing up/down arrow until 'read' is changed as 'modify'. Then press 'ENTER' button. It will ask for password. The CURR SET value can be changed by F4 (for angular set F10) or by directly setting its value through the buttons by pressing up and down arrow properly. By pressing F1 (for angular set F7), ladder

will starts to move to the CURR SET value and during the movement, instantaneous position is seen in the display by ACT. This movement can be interrupted anytime forcefully by button F5 (for angular set F11). After required operation, power supply of motors has been switched off by pressing F12.

**(b) Manual mode of operation:** To select this mode of operation, there is a key which is not shown in the Fig. 6.13. Most of the operations can be performed through the ‘touch screen’ as shown in Fig. 6.13 except ladder movement which can be controlled by jogging the buttons. First three columns of the buttons are to control the ‘linear motion’ and last three are for angular motion.

## 6.4 Status

SHARC has already been installed in SSC cave-1 and is connected with beam line-1 as shown in Fig. 6.2. We have successfully achieved a pressure  $\sim 10^{-7}$  mbar in  $\sim 8$ h by following pumping sequence as described in Sec. 6.3.1. Vacuum performance of

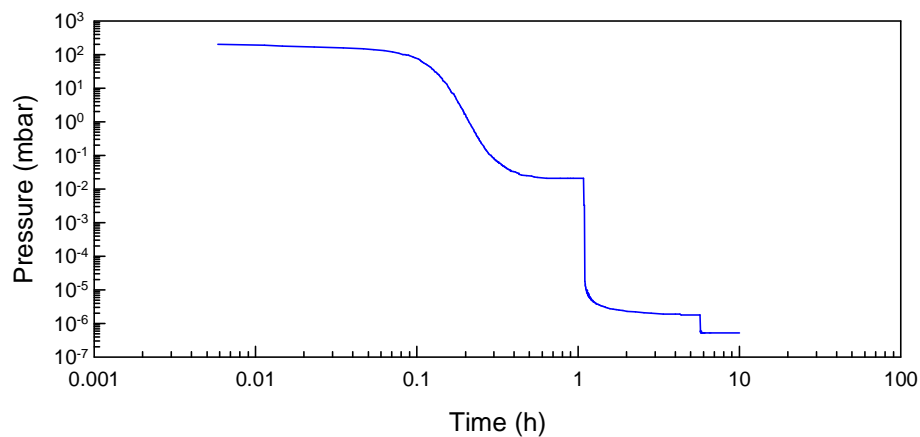


**Figure 6.14:** Vacuum performance of SHARC during a typical pumping cycle.

the chamber during a typical pumping cycle is shown in Fig. 6.14. The rough vacuum of the chamber reached its saturation value of  $\sim 2 \times 10^{-2}$  mbar in  $\sim 40$  minute by using two scroll pumps. After one hour, high vacuum valve of the turbo pumps are opened

and pressure suddenly fall to  $\sim 1.5 \times 10^{-5}$  mbar within  $\sim 75$  second. It reaches saturation at pressure  $\sim 1.4 \times 10^{-6}$  mbar at  $\sim 4$ h. At this point, the cryo pumps are connected to the chamber and pressure again falls suddenly to  $\sim 8 \times 10^{-7}$  mbar and saturates at  $\sim 5 \times 10^{-7}$  at  $\sim 8$  hours.

# Chapter 7

## Summary and conclusion

The inclusive double differential cross-sections for IMFs having atomic number,  $3 \leq Z \leq 5$ , emitted in the reactions involving both  $\alpha$ -cluster and non  $\alpha$ -cluster systems (a)  $^{16}\text{O}$  (117, 125, 145 and 160 MeV) +  $^{12}\text{C}$  and (b)  $^{11}\text{B}$  (64 MeV) +  $^{28}\text{Si}$ ,  $^{12}\text{C}$  (73 MeV) +  $^{27}\text{Al}$  and  $^{12}\text{C}$  (77 MeV) +  $^{28}\text{Si}$ , have been measured in two separate experiments [(a) and (b)]. For the system (a), the energy distributions of all fragments at all incident energies were single peaked, having nearly Gaussian shapes with their centroids at the expected kinetic energies corresponding to the binary break up obtained from the Viola systematics corrected by the corresponding asymmetric factors. The energy distributions of the fragments emitted from the systems (b) were found to have two peaks, one originating from equilibrated source, identified as FF process, and, the other from non-equilibrium source, DI process; each of these peaks is fitted with a separate Gaussian. Characterisation of the equilibrium component of fragment spectrum has been done in various ways. The angular distributions  $(d\sigma/d\Omega)_{c.m.}$  were found to follow  $1/\sin\theta_{c.m.}$  dependence in all cases. It has been observed that for each fragment, at all bombarding energies, the average  $Q$ -value is independent of emission angle, which suggests that the fragments are emitted from a completely equilibrated source at all the incident energies considered here. Total elemental cross-section for the fragments Li to B have been estimated from the experimental distributions and the same have been compared

with the statistical model predictions. At all incident energies, a significant enhancement in the yield of the fragment B have been observed over the theoretical predictions of CASCADE and EHF<sub>M</sub> calculations for the  $\alpha$ -cluster system (a). The yield of the fragments Li and Be are in good agreement with the theoretical predictions of the statistical model code CASCADE, though they are underpredicted by EHF<sub>M</sub> calculations. However, the magnitude of mismatch increases progressively from Li to B, which clearly indicates increasing additional contributions from other reaction mechanism or possible enhancement to the energy damped yield near the entrance channel configuration. The above observation is consistent with the fact that the NOC value for this system is much smaller than those for other two nearby systems - which is indicative of the formation of an orbiting dinuclear complex in  $^{16}\text{O}+^{12}\text{C}$  at the energies studied here. However, the total angle integrated yields of the equilibrium fragments in the reactions (b) are in fair agreement with EHF<sub>M</sub> predictions which confirm their compound nuclear origin; even the yields of FF fragments emitted from  $\alpha$ -cluster system,  $^{12}\text{C} + ^{28}\text{Si}$ , also match with EHF<sub>M</sub> predictions. It is interesting to note here that a previous study on fragment decay from the same system ( $^{40}\text{Ca}^*$ , produced through inverse kinematical reaction  $^{28}\text{Si} + ^{12}\text{C}$  at same excitation energy [83]) had indicated a possible signature of enhancement in fragment yield (for relatively heavier fragments;  $6 \leq Z \leq 8$ ) over those predicted by the statistical model.

As the fragment emission study of the reactions (a)  $^{16}\text{O}$  (117, 125, 145 and 160 MeV) +  $^{12}\text{C}$  indicated the possibility of dinuclear orbiting, the energy and angular distribution of  $\alpha$ -particles have been studied to measure the deformation of the produced composite,  $^{28}\text{Si}^*$ . The measured energy spectra have been compared with the same predicted by the standard statistical model calculations. It has been found that the experimental  $\alpha$ -particle energy spectra are properly explained by CASCADE only when an appreciable amount of deformation is introduced by optimizing the ‘deformability’ parameters. The extracted quadrupole deformation parameters are found to be large (larger than the corresponding RLDM values) at all beam energies. It is also observed that the deformation is found to increase with increasing the spin of the excited com-

posite. The observed enhancement of deformation in the present study may be another indication of orbiting in  $^{16}\text{O} + ^{12}\text{C}$ . However the understanding does not seem to be so simple and straightforward when one compares the above with the results of CASCADE calculation with ‘frozen’ deformation, which has also been shown to be almost equally effective in explaining the data. In this case, the effective ‘frozen’ deformation turned out to be smaller than that obtained using the optimised parameters (though it is still higher than the corresponding RLDM value). So, the uncertainties about the magnitudes of the actual compound nucleus deformations notwithstanding, it can, only qualitatively, be said that equilibrium orbiting, which is similar to particle evaporation in time scale, could also be one of the contributing factors for the observed deformation. However, the present models are too simplistic to predict the actual deformation of the compound nucleus; more realistic event-by-event Monte Carlo calculations, taking into account the initial deformation, spin distribution of the compound nucleus and their subsequent evolutions, should be performed to have a proper understanding of the compound nucleus deformation. In addition, new experimental inputs (like measurement of deformation from GDR studies [120]) are needed for more comprehensive understanding of the process.

The DI component of the fragment ( $3 \leq Z \leq 5$ ) energy distribution in all the three reactions (b) has been studied in details. It has been shown that the DI fragment angular distribution falls off much faster than  $1/\sin\theta_{c.m.}$  distribution. The time scale of the DI process has been estimated from these DI angular distributions. It has been observed that for all these reactions, the time scale, which is related to net nucleon transfer, decreases as the fragment charge increases (closer to the projectile charge). It has also been observed that the average  $Q$ -values for the DI fragments decrease with the increase of emission angle and saturate at higher angles, signifying a saturation in energy damping process beyond these angles. Assuming a compact exit channel configuration (estimated from the extracted FF part of the spectra), the angular momentum dissipation factor,  $f$ , for the DI process has been extracted. For all the three

reactions, the experimental values of  $f$  have been found to be in fair agreement with the corresponding sticking limit predictions.

A large high vacuum reaction chamber has been designed, fabricated and installed in SSC beam line-I. This Segmented, Horizontal Axis, Reaction Chamber (SHARC) will cater to needs of different types of experiments using the facilities being developed under superconducting cyclotron utilization project, VECC. SHARC is a cylindrical, three segment, stainless steel (SS 304L) chamber of length 2.2m, diameter 1m and total volume including the pipes to connect the pumps is  $\sim 1800$  litres and wall thickness  $\sim 10$ mm. The front (beam-entry) end is hemispherical in shape of radius 500mm and the rear end is elliptical dish (2:1) shaped. All three segments are mounted on separate support structures which rest on external rails such that each segment can move independently on the rails by automatic gear-motor control mechanism having built-in limit switch locking facility with manual override option. Two pairs of rails are provided within the chamber for mounting and placement of the target ladder system and the user designed detector assemblies at any position within the chamber. A generalized detector mounting table (made of Aluminum alloy 6061-T6) with precision alignment mechanism on manually movable stands with locking arrangement on rails is also provided as default arrangement. All over this table, there are inverted 'T'-shaped channels which may be used for detector mounting in a general experiment. There is provision to adjust the height of the table as per requirement of the experimental setup. The table can be easily removed from the chamber if the rails are sufficient to mount the detector system. To achieve optimum vacuum performance, all inside surfaces were given smooth granular finish and were finally electro-polished with bright finish. A target assembly is there inside the chamber; linear and rotational motion is fully controlled very precisely with the help of two vacuum compatible stepper motor and programmable logic controller. The whole assembly is mounted on one pair of internal rails and may be placed at any position within the chamber to optimize the flight path. The target assembly includes a ladder that can hold six targets at a time in a column. Two glass windows are kept to visually inspect the positions of the target

and the detector inside and also to see the beam spot at the target position (on alumina, during optimisation of beam transport) using a camera outside the chamber. SHARC has been provided with 24 ports (each of diameter 25 cm) on different locations of the body of chamber to cater to various experimental requirements, like, the connections of gas flow system, electrical signals from the detectors, detectors bias inputs, cooling pipes (if required) etc. Flanges with standard LEMO connectors as well as indigenously designed and fabricated flanges with Flat Ribbon Connector (FRC) connectors has been used as electrical feed-through to take the detector signals. The design of the pumping system has been done by considering the possible degassing load due detector systems. Two sets of pumping systems, connected in parallel, have been used to achieve the ultimate vacuum. Each set consists one turbo pump (speed 1000 l/s ) and one cryo pump (pumping speed 2500 l/s) each backed by scroll pump ( peak pumping speed 37m<sup>3</sup>/h). Whole pumping system is auto controlled by PLC. The chamber is successfully commissioned in the SSC beam line and the nominal vacuum of  $\sim 5 \times 10^{-7}$  mbar has been achieved in 8 hours in empty condition.

# Bibliography

- [1] R. Bock, *Heavy Ion Collisions*, vol. 2 (North-Holland Publishing Company, 1980).
- [2] R. Bass, *Nuclear Reactions with Heavy Ions* (Springer-Verlag, Berlin/Heidelberg/New York, 1980), first edn.
- [3] S. Ayik, D. Shapira, B. Shivakumar, *Phys. Rev. C* **38**, 2610 (1988).
- [4] P. Fröbrich, I. I. Gontchar, *Phys. Rep.* **292**, 131 (1998).
- [5] P. Hodgson, *Nuclear Heavy Ion ractions* (Clarendon press, Oxford, 1978).
- [6] N. Bohr, *Nature* **137**, 344 (1936).
- [7] F. Pühlhofer, *Nucl. Phys.* **A280**, 267 (1977).
- [8] J. Gomez del Campo, R. G. Stokstad, Description and use of the monte carlo code "LILITA", *Tech. Rep. ORNL-TM 7295*, Oak Ridge National Laboratory, TN, USA (1981).
- [9] A. Gavron, *Phys. Rev. C* **21**, 230 (1980). PACE is a modified version of JULIAN which described by Gavron.
- [10] R. Charity, *et al.*, *Nuclear Physics A* **483**, 371 (1988).
- [11] W. Hauser, H. Feshbach, *Phys. Rev.* **87**, 366 (1952).
- [12] S. J. Sanders, A. Szanto de Toledo, C. Beck, *Phys. Rep.* **311**, 487 (1999). And references therein.
- [13] R. Vandenbosch, J. R. Huizenga, *Nuclear fission* (Academic Press, 1973).
- [14] N. Bohr, J. A. Wheeler, *Phys. Rev.* **56**, 426 (1939).
- [15] P. D. Bond, *Phys. Rev. Lett.* **52**, 414 (1984).
- [16] H. H. Rossner, J. R. Huizenga, W. U. Schröder, *Phys. Rev. Lett.* **53**, 38 (1984).

- [17] S. J. Sanders, *Phys. Rev. C* **44**, 2676 (1991).
- [18] T. Matsuse, C. Beck, R. Nouicer, D. Mahboub, *Phys. Rev. C* **55**, 1380 (1997).
- [19] L. Moretto, *et al.*, *Nuclear Physics A* **259**, 173 (1976).
- [20] L. Moretto, S. Kataria, R. Jared, R. Schmitt, S. Thompson, *Nuclear Physics A* **255**, 491 (1975).
- [21] C. Bhattacharya, *et al.*, *Phys. Rev. C* **69**, 024607 (2004).
- [22] J. R. Huizenga, J. R. Birkelund, W. U. Schröder, K. L. Wolf, V. E. Viola, *Phys. Rev. Lett.* **37**, 885 (1976).
- [23] W. Nörenberg, *Physics Letters B* **52**, 289 (1974).
- [24] J. Barrette, *et al.*, *Nucl. Phys. A* **279**, 125 (1977).
- [25] T. Mikumo, *et al.*, *Phys. Rev. C* **21**, 620 (1980).
- [26] C. Beck, *et al.*, *Eur. Phys. J. A* **2**, 281 (1998).
- [27] J. R. Birkelund, J. R. Huizenga, J. N. De, D. Sperber, *Phys. Rev. Lett.* **40**, 1123 (1978).
- [28] D. A. Brombley, *Treatise on Heavy Ion Science*, vol. 2 (Plenum Press, New York, 1984).
- [29] B. Shivakumar, S. Ayik, B. A. Harmon, D. Shapira, *Phys. Rev. C* **35**, 1730 (1987).
- [30] J. Wilczyński, *Physics Letters B* **47**, 484 (1973).
- [31] D. Shapira, J. L. C. Ford, J. Gomez del Campo, R. G. Stokstad, R. M. DeVries, *Phys. Rev. Lett.* **43**, 1781 (1979). And references therein.
- [32] D. Shapira, J. L. C. Ford Jr., J. Gomez del Campo, *Phys. Rev. C* **26**, 2470 (1982).
- [33] P. Braun-Munzinger, *et al.*, *Phys. Rev. Lett.* **38**, 944 (1977).
- [34] W. von Oertzen, H. Bohlen, *Physics Reports* **19**, 1 (1975).
- [35] P. Braun-Munzinger, J. Barrette, *Physics Reports* **87**, 209 (1982).
- [36] D. Shapira, *et al.*, *Phys. Lett.* **114B**, 111 (1982).
- [37] R. R. Betts, B. B. Back, B. G. Glagola, *Phys. Rev. Lett.* **47**, 23 (1981).
- [38] R. Betts, S. DiCenzo, J. Petersen, *Physics Letters B* **100**, 117 (1981).
- [39] R. Zurmühle, *et al.*, *Physics Letters B* **129**, 384 (1983).

- [40] B. Shivakumar, *et al.*, *Phys. Rev. C* **37**, 652 (1988).
- [41] A. Glaesner, *et al.*, *Nuclear Physics A* **509**, 331 (1990).
- [42] F. Haas, Y. Abe, *Phys. Rev. Lett.* **46**, 1667 (1981).
- [43] C. Beck, Y. Abe, N. Aissaoui, B. Djerroud, F. Haas, *Phys. Rev. C* **49**, 2618 (1994). And references therein.
- [44] C. Beck, *et al.*, *Z. Phys. A* **343**, 309 (1992).
- [45] C. Beck, *et al.*, *Phys. Rev. C* **47**, 2093 (1993).
- [46] R. M. Anjos, *et al.*, *Phys. Rev. C* **49**, 2018 (1994).
- [47] R. R. Betts, S. Saini, *Physica Scripta* **1983**, 204 (1983).
- [48] A. J. Sierk, *Phys. Rev. C* **33**, 2039 (1986).
- [49] P. Kutt, *et al.*, *Physics Letters B* **155**, 27 (1985).
- [50] L. G. Moretto, *Nucl. Phys. A* **247**, 211 (1975).
- [51] L. G. Moretto, G. J. Wozniak, *Prog. Part. Nucl. Phys.* **21**, 401 (1988). And references therein.
- [52] R. J. Charity, *et al.*, *Nucl. Phys. A* **476**, 516 (1988).
- [53] R. J. Charity, *et al.*, *Nucl. Phys. A* **483**, 371 (1988).
- [54] S. A. Kalandarov, G. G. Adamian, N. V. Antonenko, W. Scheid, J. P. Wieleczko, *Phys. Rev. C* **84**, 064601 (2011).
- [55] A. K. Dhara, C. Bhattacharya, S. Bhattacharya, K. Krishan, *Phys. Rev. C* **48**, 1910 (1993).
- [56] A. Szanto de Toledo, S. J. Sanders, C. Beck, *Phys. Rev. C* **56**, 558 (1997).
- [57] L. G. Sobotka, *et al.*, *Phys. Rev. Lett.* **51**, 2187 (1983).
- [58] L. G. Sobotka, *et al.*, *Phys. Rev. Lett.* **53**, 2004 (1984).
- [59] M. A. McMahan, *et al.*, *Phys. Rev. Lett.* **54**, 1995 (1985).
- [60] T. Kozik, *et al.*, *Z. Phys. A* **326**, 421 (1987).
- [61] K. Grotowski, *et al.*, *Phys. Rev. C* **30**, 1214 (1984).
- [62] K. Grotowski, *et al.*, *Phys. Lett. B* **223**, 287 (1989).
- [63] K. Kwiatkowski, J. Bashkin, H. Karwowski, M. Fatyga, V. E. Viola, *Phys. Lett. B* **171**, 41 (1986).

- [64] G. Ademard, *et al.*, *Phys. Rev. C* **83**, 054619 (2011).
- [65] W. U. Schröder, J. R. Huizenga, *Ann. Rev. Nucl. Sci.* **27**, 465 (1977).
- [66] W. U. Schröder, J. R. Huizenga, *Treatise on Heavy-Ion Science*, vol. 2 (Plenum Press, New York and London, 1984). And references therein.
- [67] L. G. Sobotka, *et al.*, *Phys. Rev. Lett.* **46**, 887 (1981).
- [68] S. Cavallaro, *et al.*, *Phys. Rev. C* **57**, 731 (1998).
- [69] N. Carlin Filho, *et al.*, *Phys. Rev. C* **40**, 91 (1989).
- [70] A. Dey, *et al.*, *Phys. Rev. C* **76**, 034608 (2007). And references therein.
- [71] A. Dey, *et al.*, *Phys. Rev. C* **75**, 064606 (2007). And references therein.
- [72] S. Szilner, *et al.*, *Nucl. Phys. A* **779**, 21 (2006).
- [73] C. Bhattacharya, *et al.*, *Phys. Rev. C* **72**, 021601 (2005).
- [74] A. Pop, *et al.*, *Nucl. Phys. A* **679**, 793 (2001). And references therein.
- [75] C. Bhattacharya, *et al.*, *Phys. Rev. C* **66**, 047601 (2002).
- [76] C. Bhattacharya, *et al.*, *Phys. Rev. C* **69**, 024607 (2004). And references therein.
- [77] C. Bhattacharya, *et al.*, *Phys. Rev. C* **54**, 3099 (1996).
- [78] C. Beck, *et al.*, *Phys. Rev. C* **54**, 227 (1996).
- [79] S. P. Barrow, *et al.*, *Phys. Rev. C* **52**, 3088 (1995).
- [80] K. A. Farrar, *et al.*, *Phys. Rev. C* **54**, 1249 (1996).
- [81] R. M. Anjos, *et al.*, *Phys. Rev. C* **48**, R2154 (1993).
- [82] C. Beck, *et al.*, *Phys. Rev. C* **47**, 2093 (1993).
- [83] D. Shapira, *et al.*, *Phys. Lett. B* **114**, 111 (1982).
- [84] D. Shapira, *et al.*, *Phys. Rev. Lett.* **53**, 1634 (1984).
- [85] W. Dünnweber, *et al.*, *Phys. Rev. Lett.* **61**, 927 (1988).
- [86] B. Shivakumar, *et al.*, *Phys. Rev. Lett.* **57**, 1211 (1986).
- [87] S. Ayik, D. Shapira, B. Shivakumar, *Phys. Rev. C* **38**, 2610 (1988).
- [88] K. G. Prasad, *Nucl. Instrum. Meth.* **B40/41**, 916 (1989).

- [89] G. F. Knoll, *Radiation detection and measurement* (John Wiley & Sons, Inc, New York/Chichesler/Weillheim/Brisbane/Toronto/Singapore, 1999), third edn.
- [90] <http://www.srim.org>.
- [91] V. E. Viola, K. Kwiatkowski, M. Walker, *Phys. Rev. C* **31**, 1550 (1985).
- [92] T. Ericson, V. Strutinski, *Nucl. Phys.* **8**, 284 (1958).
- [93] T. Ericson, V. Strutinski, *Nucl. Phys.* **9**, 689 (1958-59).
- [94] C. Bhattacharya, *et al.*, *Phys. Rev. C* **66**, 047601 (2002).
- [95] A. Dey, *et al.*, *Phys. Rev. C* **75**, 064606 (2007).
- [96] C. Bhattacharya, *et al.*, *Phys. Rev. C* **72**, 021601 (2005).
- [97] D. Shapira, J. L. C. Ford, J. Gomez del Campo, *Phys. Rev. C* **26**, 2470 (1982).
- [98] S. Bhattacharya, K. Krishan, S. K. Samaddar, J. N. De, *Phys. Rev. C* **37**, 2916 (1988).
- [99] C. Bhattacharya, *et al.*, *Phys. Rev. C* **65**, 014611 (2001).
- [100] I. M. Govil, J. R. Huizenga, W. U. Schröder, J. Töke, *Phys. Lett.* **197B**, 515 (1987).
- [101] R. K. Choudhury, *et al.*, *Phys. Lett. B* **143**, 74 (1984).
- [102] W. A. Friedman, W. G. Lynch, *Phys. Rev. C* **28**, 16 (1983).
- [103] J. R. Huizenga, A. N. Behkami, I. M. Govil, W. U. Schröder, J. Töke, *Phys. Rev. C* **40**, 668 (1989).
- [104] D. Bandyopadhyay, *et al.*, *Eur. Phys. J. A* **14**, 53 (2002).
- [105] H. Vonach, M. Hille, *Nucl. Phys.* **A127**, 289 (1969).
- [106] W. Dilg, W. Schantl, H. onach, M. Uhl, *Nucl. Phys.* **A217**, 269 (1973).
- [107] W. D. Myers, W. J. Swiatecki, *Nucl. Phys.* **81**, 1 (1966).
- [108] D. Mahboub, *et al.*, *Phys. Rev. C* **69**, 034616 (2004).
- [109] G. Viesti, *et al.*, *Phys. Rev. C* **38**, 2640 (1988).
- [110] D. Wilmore, P. E. Hodgson, *Nucl. Phys.* **55**, 673 (1964).
- [111] C. M. Perey, F. G. Perey, *Nucl. Phys.* **17**, 1 (1976).
- [112] G. I. J.R. Huizenga, *Nucl. Phys.* **29**, 462 (1962).

- [113] S. Cohen, F. Plasil, W. J. Swiatecki, *Ann. Phys.* **82**, 557 (1974).
- [114] M. Rousseau, *et al.*, *Phys. Rev. C* **66**, 034612 (2002).
- [115] D. L. Hill, J. A. Wheeler, *Phys. Rev.* **89**, 1102 (1953).
- [116] V. E. Viola, K. Kwiatkowski, M. Walker, *Phys. Rev. C* **31**, 1550 (1985).
- [117] M. F. Vineyard, *et al.*, *Phys. Rev. C* **47**, 2374 (1993).
- [118] M. Rousseau, *et al.*, *Phys. Rev. C* **66**, 034612 (2002).
- [119] P. Bondorf, M. I. Soble, D. Sperber, *Phys. Rep.* **15**, 83 (1974).
- [120] D. Pandit, *et al.*, *Phys. Rev. C* **81**, 061302 (2010).
- [121] N. Aissaoui, *et al.*, *Phys. Rev. C* **55**, 516 (1997).
- [122] N. Aissaoui, *et al.*, *Z. Phys. A* **348**, 237 (1994).
- [123] R. Anjos, C. Tenreiro, A. de Toledo, S. Sanders, *Nuclear Physics A* **555**, 621 (1993).
- [124] W. E. Ormand, P. F. Bortignon, A. Bracco, R. A. Broglia, *Phys. Rev. C* **40**, 1510 (1989).
- [125] B. Lauritzen, G. Bertsch, *Phys. Rev. C* **39**, 2412 (1989).
- [126] B. Fornal, G. Viesti, G. Nebbia, G. Prete, J. B. Natowitz, *Phys. Rev. C* **40**, 664 (1989).
- [127] B. Fornal, *et al.*, *Physics Letters B* **255**, 325 (1991).
- [128] S. Aiello, *et al.*, *Nucl. Inst. Meth.* **AS83**, 461 ((1995)).
- [129] B. Davin, *et al.*, *Nucl. Inst. Meth.* **473**, 302 (2001).
- [130] J. Pouthas, *et al.*, *Nucl. Inst. Meth.* **357**, 418 (1995).
- [131] <http://www.lns.infn.it/gallery/ciclope/>.
- [132] <http://www.rarf.riken.go.jp/rarf/exp/e2/aschra.html>.
- [133] [http://brahma.iuc.res.in/~iuc\\_cc/veccinga3.html](http://brahma.iuc.res.in/~iuc_cc/veccinga3.html).
- [134] S. Bhattacharya, *Pramana* **75**, 305 (2010).

# Publication list

## (A) Publications relevant to the thesis:

### Referred Journals:

1. “*Fragment emission studies of the  $^{16}\text{O} + ^{12}\text{C}$  reaction*”, **S. Kundu**, A. Dey, K. Banerjee, T. K. Rana, S. Mukhopadhyay, D. Gupta, R. Saha, S. Bhattacharya, and C. Bhattacharya, *Phys. Rev. C* **78** (2008) 044601.
2. “*Complex-fragment emission in low-energy light-ion reactions*”, **S. Kundu**, C. Bhattacharya, K. Banerjee, T. K. Rana, S. Bhattacharya, A. Dey, T. K. Ghosh, G. Mukherjee, J. K. Meena, P. Mali, S. Mukhopadhyay, D. Pandit, H. Pai, S. R. Banerjee, and D. Gupta, P. Banerjee, Suresh Kumar, A. Shrivastava, A. Chatterjee, K. Ramachandran, K. Mahata, S. K. Pandit, and S. Santra, *Phys. Rev. C* **85** (2012) 064607.
3. “*A Large High Vacuum Reaction Chamber for Nuclear Physics Research at VECC, Kolkata*”, **S. Kundu**, S. Bhattacharya, J. K. Meena, T. K. Ghosh, T. Bhattacharjee, P. Mukhopadhyay, C. Bhattacharya, T. K. Rana, K. Banerjee, G. Mukherjee, S. R. Banerjee, D. L. Bandyopadhyay, M. Ahammed and P. Bhattacharya, *J. Phys.: Conf. Ser.* **390** (2012) 012075.
4. “*Deformation in  $^{28}\text{Si}^*$  produced via  $^{16}\text{O} + ^{12}\text{C}$  reaction*”, **S. Kundu**, C. Bhattacharya, S. Bhattacharya, T. K. Rana, K. Banerjee, S. Mukhopadhyay, D. Gupta, A. Dey, R. Saha, *Phys. Rev. C* **87**(2013) 024602.

### Conference Proceedings (selected):

1. “*Entrance channel effects on fragment emission*” **S. Kundu**, P. Mali, A. Dey, C. Bhattacharya, T. K. Rana, K. Banerjee, T. K. Ghosh, G. Mukherjee, D. Gupta,

- S. Bhattacharya, J. K. Meena, S. R. Banerjee, S. Mukhopadhyay, D. Pandit, A. Srivastava, Suresh Kumar, A. Chatterjee, K. Ramachandran, Proc. of DAE-BRNS Symposium on Nuclear Physics, **53** (2008) 493.
2. “*Large segmented reaction chamber for VECC superconducting cyclotron experiments*”, S. Bhattacharya, **S. Kundu**, J. K. Meena, T. K. Ghosh, T. Bhattacharjee, P. Mukhopadhyay, C. Bhattacharya, T. K. Rana, K. Banerjee, G. Mukherjee, S. R. Banerjee, D. L. Bandyopadhyay, M. Ahammed, P. Bhattacharya, Proc. of DAE- BRNS symposium on Nuclear Physics , **55** (Part II)(2010)768.
  3. “*Deformation in  $^{28}\text{Si}^*$  produced via  $^{16}\text{O} + ^{12}\text{C}$  reaction*”, **S. Kundu**, C. Bhattacharya, T. K. Rana, K. Banerjee, S. Mukhopadhyay, D. Gupta, A. Dey, R. Saha, and S. Bhattacharya, Proc. of DAE- BRNS symposium on Nuclear Physics, **56** (2011)506.

### (B) Other publications:

#### Referred Journals:

1. “*Dissipation of angular momentum in light heavy-ion collision*”, C. Bhattacharya, S. Bhattacharya, T. Bhattacharjee, A. Dey, **S. Kundu**, S. R. Banerjee, P. Das, S. K. Basu, and K. Krishan, Phys. Rev. C **69**, 024607 (2004).
2. “*Survival of orbiting in  $^{20}\text{Ne}$  (7- 10 MeV/nucleon) +  $^{12}\text{C}$  reactions*”, C. Bhattacharya, A. Dey, **S. Kundu**, K. Banerjee, S. Bhattacharya, S. Mukhopadhyay, D. Gupta, T. Bhattacharjee, S. R. Banerjee, S. Bhattacharya, T. Rana, S. K. Basu, R. Saha, S. Bhattacharjee, K. Krishan, A. Mukherjee, and D. Bandopadhyay, Phys. Rev. C **72**, 021601(R) (2005).
3. “*Evidence of large nuclear deformation of  $^{32}\text{S}^*$  formed in the  $^{20}\text{Ne} + ^{12}\text{C}$  reaction*”, Aparajita Dey, S. Bhattacharya, C. Bhattacharya, K. Banerjee, T. K. Rana,

- S. Kundu**, S. Mukhopadhyay, D. Gupta, and R. Saha, Phys. Rev. C **74**, 044605 (2006).
4. “*Characteristics of Gd-loaded liquid scintillators BC521 and BC525*”, K. Banerjee, **S. Kundu**, S. Mukhopadhyay, T. K. Rana, S. Bhattacharya, C. Bhattacharya, S. R. Banerjee, T. K. Ghosh, G. Mukherjee, T. Bandyopadhyay, A. Dey, J. K. Meena, P. Mukhopadhyay, D. Gupta, S. Pal, D. Pandit, S. Bhattacharya, Nucl. Instr. and Meth. A, **580**, 1383 (2007).
  5. “*Study of dissipative collisions of  $^{20}\text{Ne}$  ( $\approx 7\text{-}11\text{ MeV/nucleon}$ ) +  $^{27}\text{Al}$* ”, Aparajita Dey, C. Bhattacharya, S. Bhattacharya, T. K. Rana, **S. Kundu**, K. Banerjee, S. Mukhopadhyay, S. R. Banerjee, D. Gupta, and R. Saha, Phys. Rev. C **75**, 064606 (2007).
  6. “*Characterization of fragment emission in  $^{20}\text{Ne}$  ( $\approx 7\text{-}11\text{ MeV/nucleon}$ ) +  $^{12}\text{C}$  reactions*”, Aparajita Dey, C. Bhattacharya, S. Bhattacharya, **S. Kundu**, K. Banerjee, S. Mukhopadhyay, D. Gupta, T. Bhattacharjee, S. R. Banerjee, S. Bhattacharyya, T. K. Rana, S. K. Basu, R. Saha, K. Krishan, A. Mukherjee, D. Bandopadhyay, and C. Beck, Phys. Rev. C **76**, 034608 (2007).
  14. “*LAMBDA: Large Area Modular BaF<sub>2</sub> Detector Array for the measurement of high energy gamma rays*”, S. Mukhopadhyay, Srijit Bhattacharya, Deepak Pandit, A. Ray, Surajit Pal, K. Banerjee, **S. Kundu**, T. K. Rana, S. Bhattacharya, C. Bhattacharya, A. De, S. R. Banerjee, Nucl. Instr. and Meth. A, **582**, 603 (2007).
  7. “*Consistency of nuclear thermometric measurements at moderate excitation*”, T. K. Rana, C. Bhattacharya, **S. Kundu**, K. Banerjee, S. Bhattacharya, A. Dey, T. K. Ghosh, G. Mukherjee, J. K. Meena, D. Gupta, S. Mukhopadhyay, D. Pandit, S. R. Banerjee, A. Roy, and P. Dhara, Phys. Rev. C **78**, 027602 (2008).
  8. “*Giant dipole resonance width in nuclei near Sn at low temperature and high angular momentum*”, Srijit Bhattacharya, S. Mukhopadhyay, Deepak Pandit, Surajit Pal, A. De, S. Bhattacharya, C. Bhattacharya, K. Banerjee, **S. Kundu**,

- T. K. Rana, A. Dey, G. Mukherjee, T. Ghosh, D. Gupta, and S. R. Banerjee, Phys. Rev. C **77**, 024318 (2008).
9. “*Light charged-particle emission from hot  $^{32}\text{S}^*$  formed in  $^{20}\text{Ne} + ^{12}\text{C}$  reaction*”, Aparajita Dey, S. Bhattacharya, C. Bhattacharya, K. Banerjee, T. K. Rana, **S. Kundu**, S. R. Banerjee, S. Mukhopadhyay, D. Gupta, and R. Saha, Eur. Phys. J. A **41**, 39 (2009).
  10. “*Variation of neutron detection characteristics with dimension of BC501A neutron detector*”, K. Banerjee, T. K. Ghosh, **S. Kundu**, T. K. Rana, C. Bhattacharya, J. K. Meena, G. Mukherjee, P. Mali, D. Gupta, S. Mukhopadhyay, D. Pandit, S. R. Banerjee, S. Bhattacharya, T. Bandyopadhyay, S. Chatterjee, Nucl. Instr. and Meth. A, **608**, 440 (2009).
  11. “*Sharp change-over from compound nuclear fission to quasifission*”, T. K. Ghosh, K. Banerjee, C. Bhattacharya, S. Bhattacharya, **S. Kundu**, P. Mali, J. K. Meena, G. Mukherjee, S. Mukhopadhyay, and T. K. Rana, Phys. Rev. C **79**, 054607 (2009).
  12. “*Change over from compound nuclear fission to quasi-fission*”, T. K. Ghosh, K. Banerjee, C. Bhattacharya, S. Bhattacharya, **S. Kundu**, P. Mali, J. K. Meena, G. Mukherjee, S. Mukhopadhyay, and T. K. Rana, Eur. Phys. J. Web of Conference **2**, 10003 (2010).
  13. “*Extreme nuclear shapes examined via giant dipole resonance lineshapes in hot light-mass systems*”, Deepak Pandit, S. Mukhopadhyay, Srijit Bhattacharya, Surajit Pal, A. De, S. Bhattacharya, C. Bhattacharya, K. Banerjee, **S. Kundu**, T. K. Rana, A. Dey, G. Mukherjee, T. Ghosh, D. Gupta, and S. R. Banerjee, Phys. Rev. C **81**, 061302(R) (2010).
  14. “*Cluster emission in  $^{13}\text{C} + ^{12}\text{C}$  and  $^{12}\text{C} + ^{12}\text{C}$  reaction at 6MeV/nucleon*”, T. K. Rana, C. Bhattacharya, **S. Kundu**, K. Banerjee, S. Bhattacharya, G. Mukherjee, T. K. Ghosh, J. K. Meena, P. Dhara and M. Biswas, H. Pai, K. Mahata, S. Kumar,

- K. Ramachandran, P. C. Rout and S. K. Pandit, V. Nalal and R. G. Pillay, *Intr. Jour. of Mod Phys E* **20**, 789 (2011).
15. “*Evidence of quasi fission in  $^{16}\text{O} + ^{238}\text{U}$  reaction at sub barrier energies*”, K. Banerjee, T. K. Ghosh, S. Bhattacharya, C. Bhattacharya, **S. Kundu**, T. K. Rana, G. Mukherjee, J. K. Meena, J. Sadhukhan, S. Pal, P. Bhattacharya, K. S. Golda, P. Sugathan, R. P. Singh *Phys. Rev. C* **83**, 024605 (2011).
  16. “*Variation of nuclear level density with angular momentum*”, K. Banerjee, S. Bhattacharya, C. Bhattacharya, M. Gohil, **S. Kundu**, T. K. Rana, G. Mukherjee, R. Pandey, P. Roy, H. Pai, A. Dey, T. K. Ghosh, J. K. Meena, S. Mukhopadhyay, D. Pandit, S. Pal, and S. R. Banerjee *Phys. Rev. C* **85**, 064310 (2012).
  17. “*Measurement and simulation of neutron response function of organic liquid scintillator detector*”, M. Gohil, K. Banerjee, S. Bhattacharya, C. Bhattacharya, **S. Kundu**, T. K. Rana, G. Mukherjee, J. K. Meena, R. Pandey, H. Pai, T. K. Ghosh, A. Dey, S. Mukhopadhyay, D. Pandit, S. Pal, S. R. Banerjee, T. Bandyopadhyay, *Nucl. Instr. and Meth. A* **664**, 304 (2012).
  18. “*Measurement of giant dipole resonance width at low temperature: A new experimental perspective*”, S. Mukhopadhyay, Deepak Pandit, Surajit Pal, Srijit Bhattacharya, A. De, S. Bhattacharya, C. Bhattacharya, Banerjee, **S. Kundu**, T. K. Rana, G. Mukherjee, R. Pandey, M. Gohil, H. Pai, J. K. Meena and S. R. Banerjee, *Phys. Lett. B* **709**, 9 (2012).
  19. “*Onset of deformation at  $N = 112$  in Bi nuclei*”, H. Pai, G. Mukherjee, R. Raut, S. K. Basu, A. Goswami, S. Chanda, T. Bhattacharjee, S. Bhattacharyya, C. Bhattacharya, S. Bhattacharya, S. R. Banerjee, **S. Kundu**, K. Banerjee, A. Dey, T. K. Rana, J. K. Meena, D. Gupta, S. Mukhopadhyay, Srijit Bhattacharya, Sudeb Bhattacharya, S. Ganguly, R. Kshetri, and M. K. Pradhan, *Phys. Rev. C* **85**, 064317 (2012).

Conference Proceedings (selected):

1. “*Performance test of CsI & 16 channel Si- strip detector*”, **S. Kundu**, K. Banerjee, C. Bhattacharya, A. Dey, S. Bhattacharya, S. Mukhopadhyay, D. Gupta, R. Saha, P. Bhaskar, M. D. Trivedi, Proc. of DAE-BRNS Symposium on Nuclear Physics, **47B** (2004) 504.
2. “*Testing of a CsI (Tl) detector and its energy calibration*”, **S. Kundu**, K. Banerjee, T. K. Rana, C. Bhattacharya, P. C. Rout, A. Mitra, E.T. Mirgule, V. Nanal, Suresh Kumar, V.M. Datar, D. R. Chakrabarty, S. Bhattacharya, A. Dey, G. Mukherjee, T. K. Ghosh, D. Gupta, J. K. Meena, Proc. of DAE-BRNS Symposium on Nuclear Physics, **51** (2006), 618.
3. “*Charged particle detector array: 45<sup>0</sup>-175<sup>0</sup>*”, **S. Kundu**, C. Bhattacharya, T. K. Rana, K. Banerjee, S. Bhattacharya, J. K. Meena, R. Saha, G. Mukherjee, T. K. Ghosh, R. Pandey, P. Roy, M. Gohil, V. Srivastava, A. Dey, G. Pal, S. Roy, S. R. Bajirao, C. Nandi, Proc. of DAE-BRNS Symposium on Nuclear Physics, **57** (2012), 864.